The Role of the Large-scale Modes of Climate Variability in the Southern African Wave Climate

University of Cape Town

Department of Oceanography

Benjamin Oliver

Supervisor: Prof. Chris Reason (University of Cape Town)

Co-supervisor: Dr. Jennifer Veitch (SAEON)

Dissertation presented for the degree Master of Science in the Department of Oceanography at the University of Cape Town.

September 2021

Declaration

I know and understand the meaning of plagiarism and declare that all the work in this document, save for that which is properly acknowledged/referenced, is my own. I have used the Harvard convention for my citations and referencing. This dissertation has been submitted to the Turnitin module and I confirm that my supervisor has seen my report and any concerns revealed by such have been resolved with my supervisor

Signature: _____ Signed by candidate

Date: 27 September 2021

Benjamin Oliver

Cape Town

Acknowledgments

Firstly, I would like to thank my supervisors, Prof. Chris Reason and Dr. Jennifer Veitch, for their helpful inputs throughout the research process. Secondly, I would like to thank both the NRF and SAEON for funding this research and the Oceanography department for upgrading my computing power to allow for more efficient data processing and analysis. I would also like to thank my data sources: The Council for Scientific and Industrial Research for providing the in-situ wave buoy data essential to this project. The RADwave development team for providing the altimeter track data and the AVISO team for providing the gridded altimeter data. The Wavewatch III data was produced by the Centre for Australian Weather and Climate Research (CAWCR), in partnership with Australian Bureau of Meteorology and the Commonwealth Scientific and Industrial Research Organisation. The European Centre for Medium Range Weather Forecasting for creating the ERA5 product and the climate data store for making it freely available. The ERA5 cyclone track and density data were created and made openly available Gramcianinov et al. (2020). Finally, I would like to thank my family and friends for continued support over the past 2 years as well as their helpful input in the writing process.

Abstract

The wave energy flux along the southern African coastline regularly reaches extreme levels, seriously impacting coastal communities, infrastructure, as well as near-coast and offshore marine operations. Understanding the drivers behind past high wave energy events and their frequency is key to forecasting future events. Using both the in-situ wave buoy data recorded by the Council for Scientific and Industrial Research (CSIR) and satellite altimeter data, 2 global wave hindcast products are evaluated and the best-performing is chosen to assess long-term variability and trends around the coastline between 1979 and 2020. Seasonal trend analysis revealed significant increasing trends in offshore flux for all seasons, with spring having the strongest coastal trends. The role of the Southern Annular Mode (SAM), El Nino Southern Oscillation (ENSO), and the semi-annual oscillation (SAO) on the interannual monthly wave energy flux and direction variations were assessed. Individually each mode showed significant anomalies for at least one season, however often there are multiple active modes making things more complex. SAM has the strongest control on the wave energy flux anomalies, with its negative phase associated with above average flux and westerly direction anomalies and the opposite true for its positive phase. ENSO is directly correlated with the summer wave energy flux and direction implying positive flux and westerly direction anomalies during El Niño summers. The SAO is inversely associated with the wave energy flux and direction over spring and winter, implying below average flux and easterly direction anomalies during positive SAO winters and springs. All the in-situ wave height correlations showed changes when compared to partial correlations controlling for the other 2 modes. The SAO relationships showed the largest reduction in strength when accounting for the influence of SAM and ENSO. Constructive modal interference has led to both strong positive and negative anomalies in the past and will continue to do so in the future. The largest near-coast positive anomalies occurred under concurrent negative SAM and negative SAO, with more intense offshore anomalies under El Niño whereas the strongest negative anomalies occurred under a combination of La Niña with positive SAM and SAO phases.

Contents

Declaration i

Acknowledgements ii

Abstract iii

Contents iv - v

List of Tables vi

List of Figures vii - ix

List of Acronyms x - xi

1. Introduction 1

2. Literature Review 3

2.1 Wave Theory 3

2.1.1 Wave Generation 6

2.1.2 Wave Propagation 7

2.1.3 Waves and Currents 8

2.1.4 Intermediate to Shallow Water 9

2.1.5 Coastal Processes 10

2.2 Observing Waves 11

2.3 Modelling Waves 12

2.4 Climate Modes important for the Southern Hemisphere 14

2.5 Southern Hemisphere Wave Climate 16

2.5.1 The Role of Large-scale Modes of Climate Variability 17

2.6 Long Term Trends and Waves in a Changing Climate 19

2.7 A Regional Perspective: South Africa 21

2.7.1 Regional Atmospheric forcing 21

2.7.2 South African Wave Climate 23

3. Data and Methods 27

3.1 Wave Data 27

3.1.1 Buoy Data 27

3.1.2 Altimeter Data 29

3.1.3 Wave Models 30

3.2 Climate Indices 31

3.3 Model Evaluation Strategy 32

3.3.1 Preparation of Buoy Comparisons 32

3.3.2 Preparation of Altimeter Comparisons 32

3.3.3 Statistical Approach 33

3.4 Evaluation Results 34

3.4.1 Evaluation Against Buoy Data 34

3.4.2 Evaluation Against Altimeter Data 40

4. Results and Discussion 44

4.1 Seasonal Variability 44

4.2 Interannual Variability 47

4.3 The Role of the Large-scale Modes of Variability 50

4.3.1 Antarctic Oscillation / Southern Annular Mode (SAM) 54

4.3.2 El Niño Southern Oscillation (ENSO) 60

4.3.3 The Semi-annual Oscillation (SAO) 66

4.3.4 Climate Mode Combinations 72

5. Summary and Conclusion 79

APPENDIX 82

References 86

List of Tables:

Table 1: A table describing the in-situ data recorded along the South African coastline since 1978. 28

Table 2: The statistics used to plot Figure 9. The bold indicates the stronger statistic. The standard deviations and centred root mean square differences have been normalized by the observed standard deviations. 40

Table 3: The statistics used to plot Figure 11, bold text indicates a stronger statistic. 42

Table 4: Correlation coefficients from a Pearson correlation between detrended wave energy flux and mean wave direction standardized anomalies for the entire period and the subset 5-year cycle period. Bold indicates significance > 95%. 50

Table 5: Correlations between the modes in question over the whole period and during the 5-year cycle subset. Bold indicates significance at the 95% level. 54

Table 6: Seasonal correlations between ERA5 derived SAM index and in-situ significant wave height data recorded along the South African coastline at a monthly frequency. Bold indicates significance >= 95%. 60

Table 7: Seasonal correlations between in-situ significant wave height data and the ERA5 derived Niño3.4 index at a monthly frequency. Bold indicates significance >= 95%. 66

Table 8: Correlations between in-situ significant wave height and the ERA5 derived SAO index at the monthly frequency. Bold indicates significance greater than 95%. 72

Table 9: The sample sizes used to plot Figure 27 of the different phases of each mode independent of the phase of the other two and dependent on the other two in a neutral phase 73

Table 10: The sample sizes of the combinations used in Figure 28 76

Table 11: Seasonal partial correlations between SAM and the in-situ significant wave height data at a monthly frequency controlling for the SAO and ENSO. Bold indicates 95% significance. 77

Table 12: Seasonal partial correlations between ENSO and the in-situ significant wave height data at a monthly frequency controlling for the SAO and SAM. Bold indicates 95% significance. 78

Table 13: Seasonal partial correlations between SAO and the in-situ significant wave height data at a monthly frequency controlling for SAM and ENSO. Bold indicates 95% significance. 78

List of Figures:

Figure 1: A snapshot of a 1-dimension wave train in time (x on the x-axis) or a graph of the surface elevation (η) at one point for all times (t on the x-axis). 4

Figure 2: A diagram of the bending of waves and focusing of wave energy due to the depth-induced refraction (from Trujillo and Thurman 2014). 10

Figure 3: GEBCO 2020 15 arcsec bathymetry. Shows the buoy locations (black diamonds), the chosen grid points (red (ERA5) and purple (CAWCR) dots), and the center of the offshore (>50km) 1º x 1º altimeter bins coloured by region (orange, yellow, green, and red squares). The coloured triangles represent the offshore nodes used to assess the long-term variability, with the region following the same name as the squares. The contour lines represent the – 1000m and – 100m depths. 27

Figure 4: All the altimeter missions used in this study and their respective return periods. 29

Figure 5: Climatology of Hs for the in-situ data vs ERA5 (blue) and CAWCR (green) per location. The locations go from west to east. The standard deviations of each hindcast are shown by the dotted lines of the corresponding dataset. The in-situ standard deviation is shown by the shaded envelope. 35

Figure 6: As for Figure 6 but for peak period (Tp). 36

Figure 7: As for Figure 4 but for CAWCR and buoy peak direction and ERA5 mean wave direction. Only for stations measuring wave direction. 37

Figure 8: Scatter plots of ERA5 and CAWCR Hs anomalies vs in-situ buoy anomalies. Pearson correlation coefficients are shown on each plot. 38

Figure 9: Taylor diagram showing ERA5 (red) vs CAWCR (magenta) Hs anomalies against buoy Hs anomalies. 39

Figure 10: Climatologies of Hs derived from altimeter data compared to hindcast data. The grey envelope represents the altimeter standard deviation. ERA5's standard deviation is represented by the blue dashed line and the CAWCR's by the green. 41

Figure 11: Taylor diagram showing the average regional performance of ERA5 (green) and CAWCR (blue) anomalies against the altimeter anomalies of Hs. 42

Figure 12: Seasonal composite maps of wave height and their respective bias with the AVISO product. From the left: ERA5, CAWCR, AVISO, ERA5 bias, and CAWCR bias. 43

Figure 13: Seasonal composites of monthly wave energy flux (a) and monthly 10m wind, cyclone density and mean sea level pressure (MSLP). The arrows indicate the direction of the flux (a) and wind (b) and the contour lines represent 50 kW/m flux (a) and MSLP levels (b). 45

Figure 14: The annual trend in the mean seasonal wave energy flux and direction fields. The shading indicates 95% significance as determined through the pre-whitened Mann-Kendal test over the period 1980 – 2020. 47

Figure 15: Standardized wave energy flux (1) and mean wave direction (2) anomalies and their associated wavelets for offshore nodes located along the west (a), southwest (b) , south (c), and east (d) sections of the South African coastline (see diamonds Figure 3). 49

Figure 16: 10m wind (vectors), cyclone track density (colour shading) and mean sea level pressure (MSLP) (solid (positive) and dashed (negative) lines) anomaly composites for different combinations of positive/negative (> 1.5sd, <1.5sd) wave energy flux and direction anomalies at the south node. 51

Figure 17: Time series of the 5 month-rolling mean standardized wave energy flux and direction anomalies compared to the ERA5 derived SAM, ENSO, and SAO indices. The solid black line in plots c), d) and e) represents the 5-month rolling mean. 52

Figure 18: 10m wind speed (a) and direction (b) anomalies seasonally correlated with SAM. Only correlations significant at 95% and greater are shown. The darker the colour the stronger the correlation. 54

Figure 19: Monthly wave energy flux (CgE (kW/m)) (a) and direction (b) seasonally correlated with SAM. Only areas significant at the 95% level are shown. 56

Figure 20: Wave energy flux and direction anomalies under negative (left) and positive (right) SAM by season. The shading indicates 95% significance in the wave energy flux anomalies. 58

Figure 21: Same as Figure 19 but for detrended correlations with the ERA5 derived Niño3.4 index. Only correlations significant at 95% are shown. 61

Figure 22: Same as Figure 20 but for detrended correlations with the ERA5 derived Niño3.4 index. Only correlations significant at 95% are shown. 63

Figure 23: Same as Figure 21 but for negative (La Niña) and positive (El Niño) months. Shading indicates 95% significance. 65

Figure 24: Detrended spatial correlations between the SAO index and 10m wind speed (a) and direction (b). Only correlations significant at the 95% level are shown. 67

Figure 25: Same as for Figure 19 but for detrended correlations to the ERA5 derived semi-annual oscillation index. Only correlations significant at 95% or greater are shown. 69

Figure 26: The same as Figure 19 but for seasonal composites under negative and positive SAO events. The shading indicates significance at the 95% level. 71

Figure 27: Composites of the positive and negative phases of SAM, ENSO, and the SAO for months when the mode in question is active dependent on the other two modes being in a neutral phase (Dependent columns) compared to composites when only the mode in question is active independent of the other two (Independent columns). The phase is defined by an exceedance of one standard deviation away from the mean in the positive or negative direction and the sample sizes of each composite given in Table 9. The solid (dashed) contour line indicates anomalies 5 kW/m above (below) the mean. 74

Figure 28: Composites created from monthly wave energy flux and mean wave direction anomalies for various combinations of different phases of the atmospheric modes. Shading indicates the 95% significance. 75

List of Acronyms:

AVISO	Archiving, Validation and Interpretation of Satellite Oceanographic Data
CAWCR	Centre for Australian Weather and Climate Research
CFSR	Climate Forecast System Reanalysis
CFSv2	Climate Forecast System Version 2
CMEMS	Copernicus Marine Service
CSIR	Council for Industrial and Scientific Research
CSIRO	Commonwealth Scientific and Industrial Research Organisation
CgE	Wave energy flux (kW/m)
Dp	Peak wave direction (º)
ECMWF	European Centre for Medium-range Weather Forecasting
ENSO	El Niño Southern Oscillation
EOF	Empirical Orthogonal Function
ERA5	European Reanalysis 5
f	Frequency
Fs	Peak spreading factor
GEBCO	General Bathymetric Chart of the Oceans
GPH	Geopotential Height
Hmax	Maximum wave height (m)
Hs	Significant wave height (m)
MFWAM	Meteo France Wave Model

MSLP	Mean Sea Level Pressure
MWD	Mean Wave Direction (º)
MWP	Mean Wave Period (s)
NOAA	National Oceanic and Atmospheric Administration
NRF	National Research Foundation
SAM	The Antarctic Oscillation / Southern Annular Mode
SAWS	South African Weather Service
SAO	The Semi-annual Oscillation
SAEON	The South African Environment Observation Network
SOI	Southern Oscillation Index
SST	Sea Surface Temperature
TEMP	Air temperature
Tcz	Spectral crest period
Tp	Peak wave period
Tz	Average zero down-crossing period
r	Correlation coefficient
RCP	Representative Concentration Pathway
UKMO	United Kingdom Meteorological Office
WAM	WAve Model
WW3	Wavewatch 3
λ	Wavelength
η	Surface elevation
ω	Wavenumber

1. Introduction

The proximity of the Southern African coastline to the intense surface winds of the high southern latitudes causes it to regularly experience high wave energy events. These events can lead to fatalities, substantial coastal inundation, and flooding, structural erosion as well as seriously hinder offshore and coastal marine operations. However, this high wave energy environment is not all bad. When considering the fast-improving efficiency and dropping cost of wave energy converters our energetic coastline could prove to be part of a green solution to South Africa's current energy crisis (Joubert and van Niekerk, 2013; Lavidas and Venugopal, 2018). For both the protection of coastal communities and ocean users as well as the conversion of this power source it is vital that we know when and how frequently this flux is going to reach detrimental levels. Understanding when and how these events have occurred in the past requires understanding what drives the long-term variability in the wavefield around the coastline. Once the drivers of these intense wave energy events are identified we may be able to forecast the severity of a coming season.

An understanding of the long-term variations in wave energy has previously been achieved using visual observations from ships, in-situ wave buoys, altimeter wave heights, and numerical ocean wave models. Arguably the wave models have the ability to provide the most consistent, continuous record of the past long-term variability. This continuity is achieved using validated global and regional 3rd generation wave models driven by ocean surface winds from atmospheric models as well as in situ and satellite altimeter observations. Currently, several modeling centers run different versions of global coupled and uncoupled 3rd generation wave models, supplying the public with accurate hindcasts, nowcasts, and forecasts. Ultimately the accuracy of a wave model's forecast depends on both how well it can be tuned to match the past, its hindcast, and more so on the accuracy of the atmospheric forcing used to generate the forecast.

This thesis sets out to assess two global wave hindcasts against the in-situ data collected around the southern African coastline since 1979. It then uses the best-performing product to assess the long-term variations and trends in the wave energy flux around the South African coastline and the relations to the large-scale modes of atmospheric variability. Previous work on the wind and wave climate of the oceans surrounding Southern Africa has found significant relations to the large-scale modes of atmospheric variability (Reason and Rouault, 2005; Birkett, 2010; Veitch *et al.*, 2019). Using the best-performing hindcast product and the in-situ wave buoy data, this research then aims to gain an in-depth understanding of the role of these modes in the long-term changes in both the magnitude and direction of the wave energy flux impacting the Southern African coastline.

Following on from here there is a discussion of ocean waves, the theory used to model them, and a review of the research on global and regional wave climate variability (Section 2). The data, methods

used as well as the evaluation of the hindcasts used in this research are found in Section 3. The chosen hindcasts monthly fields of wave energy flux, direction, 10m wind, and cyclone density anomalies are then used to assess the seasonal and long-term variations in Section 4. This section ends with a summary of the results followed by the conclusion (Section 5).

2. Literature Review

2.1 Wave Theory

Any person observing the sea notices the periodic rise and fall of its surface. This oscillation is due to the propagation of energy through the ocean surface in the form of gravity waves, the most noticeable of these being the shorter period surface waves. These are called ocean surface gravity waves and are generated by an external input of energy into the ocean surface from the wind stress of the overlying surface winds. Other external forces such as the gravitational pull of the moon and sun or the seismic waves from an earthquake generate the tides and tsunamis, but this investigation is solely focused on surface ocean gravity waves generated by surface winds. These waves are characterized by wave heights between 0.1 – 20m and periods between 1 – 25s (Laing *et al.*, 1998). Different types of ocean waves exist outside of this range. With shorter periods and lower wave heights, they are classified as capillary waves, due to the restoring force at this scale being the surface tension of the water. With larger periods they are classified, in increasing wavelength, as seiches, storm surges, tsunamis, Rossby waves, and tidal waves. Like this classification of different waves, sea states can also be defined by the dominant wave period and height.

A sea state which appears ordered with a consistent period and the waves arriving in groups – called sets – is dominated by swell waves. These are waves that have long since dispersed from their generation zone becoming more sorted as they travel. On the other hand, a sea state which appears messy with a shorter less consistent period between waves and little to no grouping is dominated by locally generated wind-waves. These waves have not dispersed far, if at all, from their generation zone and are generally less powerful and are strongly influenced by local winds. These states of the sea are represented mathematically by their characteristic energy density spectrums. A wind sea state is classified by a wide spectrum due to the presence of multiple frequencies whereas a swell-dominated sea state is classified by a narrow spectrum with the dominance of one or two frequencies. The energy density spectrum follows from the idea that any complex sea state or wavefield can be represented by an infinite number of separate wave trains through a Fourier transformation (Laing *et al.*, 1998; Holthuijsen, 2010). At any one point, the ocean observer experiences the complex interference between many different wave trains, being a function of both the strong winds of distant storms (swell waves) and the local winds. To further understand and discuss surface ocean gravity waves, their spectrum, and variability the linear wave theory which has historically been used to understand these waves and their evolution must be discussed.

Linear wave theory is the theory used to model and describe ocean waves (Laing *et al.*, 1998; Holthuijsen, 2010). Although ocean surface gravity waves are rarely perfect sinusoidal waves, this

simplification has proven practically useful in describing their variability at both high and low frequencies. There are other wave theories such as Stokes waves, cnoidal waves, etc… which better fit the shape of ocean surface waves particularly in shallow waters and wind seas, but these theories are nonlinear and much more mathematically dense. A lot can be understood about ocean waves by first understanding the simple linear wave theory and then building up to more complex waveforms where necessary.

One solution to the momentum and continuity equations for the case of one fluid flowing over another fluid with a different density follows by making some broad assumptions: the incompressibility of seawater, the neglection of the viscosity of seawater, neglecting the Coriolis force, and that the energy propagates along a 2D plane, is a disturbance in the underlying fluid which requires an oscillating solution. Linear wave theory provides the ability to understand the movement of this disturbance through space and time. The full derivation can be found in many textbooks (Laing *et al.*, 1998; Holthuijsen, 2010) and is not necessary for the topics discussed in this thesis.

Firstly, the waves are classified by their height, length, period or frequency, and direction. To discuss surface ocean gravity waves these terms and others must be defined: a trough is the lowest point between consecutive crests; a crest is the local maximum of the sea surface elevation between 2 consecutive troughs; amplitude (A(m)) is the vertical distance from mean sea-level to the crest or trough, wave height (H(m)) is the vertical distance from trough to crest and is equal to 2A (Figure 1); wavelength (λ(m)) is the horizontal distance between 2 consecutive crests; period (T(s)) is defined as the time for 2 consecutive crests to pass a fixed point and frequency (f(Hz)) is its inverse i.e. the number of waves passing a fixed point over a given amount of time. The derived equations describe the evolution of long parallel crested, small amplitude, sinusoidal waves that are restored by gravity and are used as an approximation to model ocean surface gravity waves (Figure 1). Below is an example of the equation for one wave train in one dimension:

$$\eta = Asin(\omega t - kx) \quad (1)$$

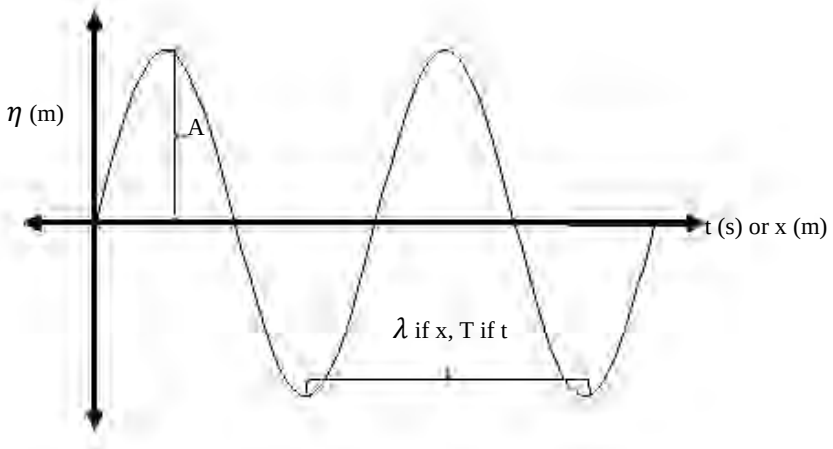

Figure 1: A snapshot of a 1-dimension wave train in time (x on the x-axis) or a graph of the surface elevation (η) at one point for all times (t on the x-axis).

where η is the surface elevation at any point in time (t) and space (x); A is the amplitude – the height above mean sea level; ω is the angular frequency which is equal to 2π/T; and k is the wavenumber which equals $2\pi/\lambda$. This equation describes a single wave train that has a particular wave height, period and wavelength, or angular frequency and wavenumber. Since the time it takes one wave to travel its wavelength is the period, the wave speed is given by: c = λ/T or c = λf or c = $\frac{\omega}{k}$ giving each wave train a characteristic speed, known as its phase speed (c). It is important to clarify that these parameters describe the amount of energy propagating through the surface ocean. Therefore, increases in amplitude or height and period or length indicate that the magnitude of the energy flux is increasing. When observing the waves arriving at the shore it becomes clear that the larger waves arrive in groups less frequently. These groups are known as sets and form due to the wave energy travelling at half the phase speed of the individual wave train, known as the group speed (c_g). These pulses of energy periodically arrive at the shore every 2 to 15 minutes depending on the combination of frequencies present in the wavefield. The magnitude of this wave energy flux (CgE) is a function of both the height and period of the waves:

$$CgE = \rho g^2 g^2 H_s^2 \frac{Te}{64\pi} \quad (2)$$

where ρ is water density – assumed constant here at 1025 kgm^{-3}; g is the gravitational constant (9.81 ms^{-2}), H_s is significant wave height – the average height of the third highest waves; and T_e is the energy period – 0.82 x the peak period which is the wave period at the spectral peak. A result of each wave train having a unique speed is that waves with longer wavelengths travel faster than those with shorter wavelengths. In deep water, this leads to longer waves travelling out of generation areas faster than shorter ones, known as dispersion. This co-dependence of wavelength on period and vice versa is known as the dispersion relationship:

$$\omega^2 = gktanh(kd) \text{ or } \lambda = \frac{gT^2}{2\pi} tanh\left(\frac{2\pi d}{\lambda}\right) \quad (3)$$

where g is again the gravitational constant; d is water depth; T is period and λ is wavelength. This is the dispersion relationship for an arbitrary water depth. As can be seen from the dependence on depth in this relationship, waves behave differently in different water depths. In deep water, d > $\frac{\lambda}{4}$, the ocean waves do not interact with the ocean floor, allowing for longer waves to disperse faster than shorter ones. In this case tanh(kd) approximates to 1 as kd approaches infinity, and the dispersion relationship becomes:

$$\omega = \sqrt{gk_0} \text{ or } \lambda_0 = gT^2/(2\pi) \quad (4)$$

where k_0 and λ_0 are the deep-water wave number and wavelengths. The phase speed becomes $c = g/\omega$ and the is entirely dependent on ω. In shallow water, $d < \frac{\lambda}{25}$, ocean waves undergo a wide range of changes with only the period being conserved. The dispersion relationship is again simplified because tanh(kd) approximates kd as kd approaches 0.

$$\omega = k\sqrt{gd} \text{ or } \lambda = \frac{gT^2 d}{\lambda} \quad (5)$$

This simplification shows that the wave speed is no longer a function of wavelength or period. It is rather a function of only the water depth and gravity: $c = \sqrt{gd}$, therefore the waves are no longer dispersive. In between deep and shallow water where $\frac{\lambda}{25} < d < \frac{\lambda}{4}$ the dispersion relation does not simplify, and iteration is required to solve for the wavelength and speed. The phase speed is dependent on both wavelength and depth, making things more complex over these depth ranges. The changes in the wavefield between deep and shallow water are discussed in Section 2.2.4. Thus far, linear wave theory has allowed us to understand the propagation of sinusoidal ocean waves through different water depths but if we want to understand the long-term changes in these waves, then we must first understand how these waves are created.

2.1.1 Wave Generation

The research in this thesis is solely focused on surface waves that have been generated by wind. In this type of wave generation, strong surface winds input energy into the underlying ocean through friction, known as wind stress, roughly in proportion to the square of the wind speed. Starting from a flat ocean the wind first generates small perturbations in the surface ocean through Phillips' resonance (Laing *et al.*, 1998). These small perturbations, called capillary waves, are generated on the ocean surface and restored by surface tension. These perturbations then undergo linear growth as they move in resonance with the turbulent airflow fluctuations above them (Phillips, 1957). As they grow gravity takes over as the restoring force and the waves continue to propagate roughly in the direction of the generating winds. Once reaching a height large enough to affect the airflow above them Phillips' resonance is no longer significant and shear flow instability takes over. These larger waves are now pulled at the crests and pushed on the troughs by the drag of the wind in what is known as shear flow instability (Laing *et al.*, 1998).

This wavefield – with waves existing in a range of heights, frequencies, and directions – can be mathematically represented through the summation of the different wave trains giving the energy density spectrum that has three main drivers of change known as source terms:

$$\frac{\partial E(f,\theta)}{\partial t} + c_{gx}\frac{\partial E(f,\theta)}{\partial x} + c_{gy}\frac{\partial E(f,\theta)}{\partial y} = Sin + Snl + Sds \quad (6)$$

where E(f, θ) is the energy density spectrum, $c_{gx,y}$ is the group velocity in the x and y dimension, f is frequency, θ is direction, S_{in} is the input from winds, S_{nl} is the non-linear interaction term and S_{ds} is the dissipation due to white-capping (Holthuijsen, 2010). Of these source terms, S_{in} is relevant here as it describes how the wind affects the spectrum. Miles (1957) theorized that S_{in} depends not only on the wind input but also on the spectrum (underlying wavefield) (Miles, 1957). Field and laboratory research found Miles' formulation to predict growth rates below the observed rates. This theory was later built upon by Janssen (1991) who found that the drag coefficient varies with respect to the age of the wind-wave field such that the growth rate is quicker for young wind sea (Laing *et al.*, 1998). It also allowed for a deeper understanding of wave generation and a more accurate representation within computer models.

Wave growth has also been empirically studied (Sverdrup and Munk, 1947; Pierson, 1955; Hasselmann *et al.*, 1973). These studies used large ocean datasets to derive empirical wave growth curves as a function of wind-speed, fetch, and duration. These curves proved operationally useful for forecasting until 3rd generation wave models became computationally feasible.

The growth of surface waves continues if they are still under the influence of the wind, i.e., within the fetch. Over the fetch area, the wind continuously inputs energy generating waves that travel in the direction in which it is blowing and roughly 25º either side of the wind direction (Laing *et al.*, 1998). The longer the wavefield is under the wind the longer it will accumulate energy. This energy is input as high-frequency wind-waves but as the different wave trains begin to interact and resonate the energy is transferred toward the lower frequencies. This movement of energy occurs through the non-linear quadruplet wave-wave interaction and is the main source of energy for low-frequency wave growth (Mitsuyasu, 1971; Hasselmann *et al.*, 1973) . Due to the heavy computing required to account for this non-linear phenomenon, it was only properly incorporated into 3rd generation wave models and is one of the main improvement areas when comparing to the 1st and 2nd generation models (see Section 2.3: Modelling Waves).

Another important process occurring during wave generation is white capping. When ocean waves reach a limiting steepness > 0.55 (steepness = kH/2) they are forced by gravity to break (Toffoli *et al.*, 2010). This is enhanced by the wind in the fetch area, which creates greater instability and leads to more white capping. This process is dissipative as the energy is transformed into tangential surface currents and lost from the wavefield. Through these processes, the wavefield develops. Once the waves leave the fetch, they are no longer receiving energy from the airflow. The wind-waves now begin to transform/sort into swells through angular spreading and dispersion.

2.1.2 Wave Propagation

Through propagation wind-waves transform into swell waves, becoming more sinusoidal with time. Over the fetch area, the wind continuously inputs energy generating waves that travel in the direction and roughly 25º either side in which the wind is blowing (Laing et al., 1998). The energy also spreads out with a $\cos^2()$ distribution, known as angular spreading (Laing *et al.*, 1998). The swell spreads as it moves through deep water propagating through the ocean surface at the group speed.

With time and distance, these effects cause the wave energy to become more spread out eventually dissipating on shorelines far from their fetch areas. Most of this journey will be through deep water, in which surface layer currents and different wind fields will cause the most variability in the wave direction. However, as the waves enter intermediate and shallow water they change through the processes of refraction, shoaling, diffraction, and reflection (Section 2.1.4). In certain special cases, namely, when waves are propagating under fast-moving tropical and extratropical cyclonic systems, they will not escape their generating winds before reaching the coastline. In these cases, the ocean continuously receives energy from the wind and multiple frequencies arrive simultaneously at the coast. This process leads to high broad spectrum wave energy and a rise in the mean sea level, known as a storm surge, which can be detrimental to coastal communities. However, before the wave energy reaches the coast it must first traverse any ocean currents in its trajectory.

2.1.3 Waves and Currents

When waves propagate through the surface ocean, they ultimately travel through ocean currents. In certain cases, these interactions modify the wavefield and have led to significant amplification and bunching of this wave energy, creating conditions favorable to rogue wave development (Grundlingh and Rossouw, 1995; Laing *et al.*, 1998; Lavrenov, 1998; Holthuijsen, 2010; Quilfen and Chapron, 2019; Barnes and Rautenbach, 2020). This modification is of particular importance on the western side of ocean basins, where strong warm-core western boundary currents are found. Previous research has highlighted the importance of these strong currents, but how do they affect the wavefield?

The interactions between waves and currents are reasonably well understood in theory and they mainly occur due to energy density not being conserved when waves propagate through current fields. This lack of energy density conservation allows for refraction, wave bunching, and energy transfers between the current and wavefield which have significant impacts on the height and direction of the waves (Holthuijsen, 2010). The effects are well explained using idealized cases by Barnes and Rautenbach (2020): waves propagating into an opposing (following) current will be amplified (stepdown), however the stepdown is far more gradual than the amplification which is exponential until the limiting steepness is reached. In a uniform current, the degree of amplification (stepdown) directly depends on the period of the waves, with shorter periods being more significantly impacted by current fields. For example, if a 3m wave with a 12s (8s) period propagated into a $3ms^{-1}$ opposing

flow the height would enhance by 60% (250%). The wave direction also changes significantly depending on the period and whether the incident angle is positive (current following) or negative (current opposing), here current following waves respond stronger.

These responses of the wavefield are significant particularly for waves propagating into strong ocean currents, but what happens when waves are generated within a current field? This question was addressed by Rapizo *et al.* (2018), who investigated the impacts of Southern Ocean surface currents on the wave generation in this region. They found that due to the relative wind speed effect- the reduction of the wind speed felt by the surface ocean due to it being in motion – the energy input into the surface ocean was lower and the waves were less energetic. When compared to satellite observations, there was an increase in performance which emerged through the reduction of the large positive bias present in the high southern latitudes. Compared to in-situ moored data, they found this had a more significant effect on long-period swells generated far from the site. These long-period swells are generated closer to the center of the Antarctic Circumpolar current and therefore more influenced by the inclusion of surface currents in their generation region (Rapizo, Durrant, and Babanin, 2018). Clearly ocean waves are significantly affected by the current field where they are generated through the relative wind effect, and in the regions they travel, through the bunching and focusing of wave energy. These modifications change how the waves arrive at the coastline, where the waves undergo another set of changes due to the shoaling depth.

2.1.4 Intermediate to Shallow Waters

In the discussion of linear wave theory, it was noted that only deep water waves are truly dispersive as the wave speed depends only on the length or period of the wave in deep water. When waves approach the coastline, the depth becomes shallower until the waves are forced to break but before they break the shoaling depth significantly modifies the wavefield. This primarily occurs through changes in the response of tanh(kd) because as d approaches zero, tanh(kd) approaches kd. Thus, the wave speed is only a function of depth in waters shallower than $\frac{\lambda}{25}$ (Holthuijsen, 2010).

This dependence on depth leads to the bending of the wave crests to almost orthogonal to the coastline once reaching the shore, known as refraction (see Figure 2). Refraction is also responsible for wave energy focusing on headlands, rocky outcrops, underwater seamounts, and reefs (Figure 2). Shoaling also occurs as waves propagate into shallow waters: they initially decrease, then ultimately increase in height as the waves approach the coast. It occurs through the conservation of energy: the decrease in wave speed and wavelength is balanced by an overall increase in wave height until the breaking point is reached. Diffraction is the bending of wave rays around obstructions such as harbour walls, headlands, or rocky outcrops. The last process occurring in shallow water is reflection, which is the bouncing of waves off rocky outcrops or the shoreline and occurs orthogonal to the incident angle

between the wave and the object. Once the waves reach a height > $\frac{1}{7}\lambda$; or the height is > $\frac{3}{4}d$ or the angle between crest and trough is < 120º, they break. The breaking transfers the momentum of the wave into tangential currents, leading to longshore flow which significantly controls the movement of sediment along the coast.

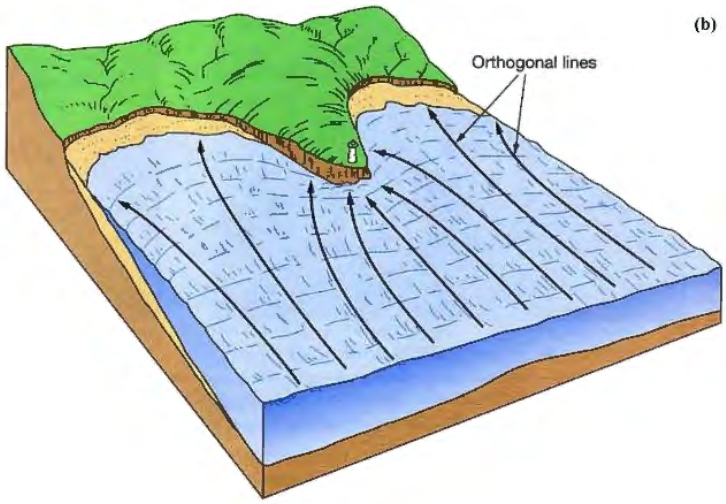

Figure 2: A diagram of the bending of waves and focusing of wave energy due to the depth-induced refraction (from Trujillo and Thurman 2014).

2.1.5 Coastal Processes

At the coastline, waves are responsible for the stability of the shoreline driving the processes of shoreline erosion through wave-induced currents. In the surf zone, wave energy is converted into alongshore transport through the process of wave breaking. This area between the shore and behind the breakers is thought of as the river of sand with wave energy being the driving force (Holthuijsen, 2010). The conversion of wave energy into longshore currents transports sediment in the direction of the wave propagation. For example, a shoreline with orientation NW-SE impacted by a southerly swell will cause sediment transport 'up' the shoreline, toward the north. This process is happening every day and drives the seasonal episodic erosion of the coastline. This erosion peaks with the peak of wave energy, usually in winter months, and then slows over the summer even allowing some of the sediment placed offshore by large wave events to return causing no net loss in sediment and no progradation of the coastline.

Whereas in extreme cases i.e., when wave energy reaches a 1 in 100-year maximum, large sediment transport is brought about, leading to the structural erosion and possible progradation of the coastline. This structural erosion is worsened by the encroachment of housing onto the dune system as the dune system acts as a natural stability barrier against these high wave energy events (Theron, 2016). As well as decreasing the stability of the shoreline, coastal housing developments put their inhabitants at high risk during these events, primarily due to the storm surge effect often present during these

intense wave energy events. The resulting rise in the sea-level, allows the wave energy to reach further inland past the setback line, which damages infrastructure and endangers human life.

Even more worrying for low elevation coastal developments are the future projections of sea-level rise, and cyclone intensity. The combination of sea-level rise with more intense cyclonic systems leads to greater reach inland and a higher destructive power of high wave energy events particularly when they occur simultaneously with spring tides (Corbella and Stretch, 2012). It is vital to understand the drivers of wave variability at various temporal scales along the coastline. This is achieved via in situ and satellite observations in combination with ocean wave modelling. The latter can give accurate forecasts up to 7 days in advance, giving those vulnerable the ability to prepare/evacuate. Such forecasting partially reduces the vulnerability of these coastal inhabitants as well as aids coastal developers and in the preservation of coastal infrastructure.

2.2 Observing Waves

The main way that wave variability is understood is through the long-term observation and modeling of ocean waves. Observations can be made visually from shore or ship, using in situ measurements from wave rider buoys or acoustic doppler current profilers, or using satellite altimeter data. Visual observations are and have been useful and they certainly can be used to understand wave variability, however, due to the inconsistencies between different observers as well as the lack of continuity they are not ideal. A more continuous record is obtained using unmanned observations via buoys or altimeters, their main advantage being continuity and consistency.

Wave rider buoy records have been used extensively to understand wave variability at various temporal scales (Shillington, 1974). These instruments were originally non-directional but have been further developed to measure wave direction as well. They work through the assumption that the wave record is stationary over the observation period, 15 – 30 minutes. From the measured wave spectrum, they report derived variables valid for this stationary period. This data is then transmitted to land-based observation centers where it is made available to the public in near real-time.

The most commonly reported variables derived from the observed energy density spectrum are significant wave height (Hs), peak period (Tp), and peak direction (Dp). Significant wave height is the average height of the highest third of all waves in a wave record and is thought to be most representative of the wave height due to the above-mentioned wave grouping (Laing *et al.*, 1998). Peak period and peak direction are defined as the period and direction at the peak of the observed spectrum and represent the dominant period and direction over the stationary period (Holthuijsen, 2010). Other commonly reported variables are maximum wave height (Hmax), mean wave period and

direction (Mwp, Mwd), and wave energy flux (CgE). These parameters all ultimately describe the magnitude and direction of the wave energy flux as per equation (2).

Altimeters have been measuring wave height almost continuously since the launch of GEOSAT in 1985 bar approximately 2 years between GEOSAT and ERS-1 missions. They provide global coverage which is not temporally consistent due to the varying return periods of each satellite. Satellite altimeters work through the emission of a radar pulse, with the waveform of this return pulse indicating surface roughness. For a smooth ocean surface, the return signal is almost instantaneous and is measured as a pulse. Whereas for a rough surface there is a temporal delay that slopes and broadens the return signal. It is through measurements of this distortion of the signal that the significant wave height under the radar footprint is empirically derived. Generally, altimeters measure along-track at a 1Hz frequency, giving a spatial resolution of approximately 6-10km but take between 10 and 40 days to return to the same geographic location (Figure 4). These data are then used to study short- and long-term variability (Young *et al.*, 2011; Young *et al*., 2020). Along-track allows for the analysis of waves within a system, for example studying ocean waves within the Agulhas current (Grundlingh and Rossouw, 1995; Quilfen and Chapron, 2019; Barnes and Rautenbach, 2020). Whereas through binning, spatial averaging, and re-gridding this along-track data global climatologies of wave height can be created. Such as in Young *et al.* (1999) who highlighted the global importance of Southern Ocean swells using 10-years of gridded altimeter data. However only wave height and period data can be derived from these altimeters therefore, to understand how the direction of these waves varies altimeter data needs to be combined with in-situ direction measurements or with wave direction outputs from an ocean wave model.

2.3 Modelling Waves

Using numerical approximations to the linear wave theory discussed above, ocean wave models have been designed and run on supercomputers since the 1960s. The need to accurately model ocean waves was first realized in the early 1940s when naval fleets needed to know the future wave conditions to plan for landing operations during World War II (Komen *et al.*, 1996; Mandal and Prabaharan, 2010). These forecasts were performed using empirical wind sea and swell laws which were based on the work of Sverdrup and Munk (1947) (SWAMP Group, 1985; Mandal and Prabaharan, 2010). They provided wave variables for a particular location derived from the length and intensity of ocean winds over the fetch area.

Throughout the 1950s significant developments in the understanding of linear wave theory and our ability to mathematically represent it occurred. These were the idea of the wave spectrum and theory of its evolution (Pierson, 1955; Gelci, 1957), the theory of wave generation by wind (Miles, 1957; Phillips, 1957), the concept of the universal equilibrium range of the spectrum (Phillips, 1958), and

Hasselmann's (1962) work on deriving the non-linear energy source function. These developments allowed for the mathematical description of the evolution of the wave spectrum, as per equation 6.

This source function serves as the building blocks for first- and second-generation models throughout the 1960s and 70s. First-generation wave models neglected the S_{nl} term and were generally known as decoupled propagation models (Hasselmann, 1963; Laing *et al.*, 1998). They proved useful in providing forecasts, but the research community quickly realized the lack of accuracy when compared to in-situ observations (SWAMP Group, 1985). It was found that under very strong winds the physics of wave growth appeared misrepresented, and the parameterization had to be increased by several orders of magnitude to achieve the observed wave growth (Barnett and Sutherland, 1968).

Throughout the 1970s extensive fieldwork revealed a new view of the energy balance of a growing wind-sea, pointing to the non-linear energy transfers as the principal low-frequency energy source (Mitsuyasu, 1971; Hasselmann *et al.*, 1973). This put the focus on understanding the S_{nl} term and drove the development of 2nd generation wave models. The models contained 2 attempts to parameterize this term: coupled hybrid and coupled discrete. The main distinction being the difference between discrete and parametrical regions of the energy spectrum. In coupled hybrid models, only swell waves are treated discretely whereas in coupled discrete models only the tail end, beyond the wind and swell peaks is treated parametrically (SWAMP Group, 1985; Laing *et al.*, 1998).
Research by the SWAMP Group (1985) revealed that these 1st and 2nd generation models provided widely varying results under the same intense winds, and the wave modelling community was pushed to develop a more accurate representation and forecast. Simultaneously computing power was on the up and the development of 3rd generation wave models, which explicitly calculate the non-linear interactions using the discrete interaction approximation of Hasselmann and Hasslemann (1985), was underway.

In 1988 the WAMDI group successfully implemented the first 3rd generation spectral wave model, the WAM (WAve Model) (Hasselmann *et al.*, 1988). This model has been run operationally at the Fleet Numerical Meteorology and Oceanographic Center since 1994 (Wingeart, 2001). Another 3rd generation spectral model was concurrently being developed through the late 1980s and early 1990s at the Delft University of Technology, known as the WAVEWATCH (WAVE height, WATer depth, and Current Hindcasting) model (Tolman, 1989, 1991). It was further developed at the North American Space Agency (NASA) into WAVEWATCH II and then at the Nation Center for Environmental Prediction (NCEP) into WAVEWATCH III (Tolman, 1992; NOAA, 2009).

These 2 models proved far more accurate in their representation of the wavefields and served as the building blocks for the current state of the art reanalysis products. They have been extensively validated at both the global and regional scale (Janssen, *et al.*, 1997; Sterl, *et al.*, 1998; Wingeart,

2001; Cox and Swail, 2001, Hanson, *et al.,* 2006; Gorman, *et al.,* 2010; Chawla, *et al.* 2013). Janssen, *et al.* (1997) assessed forecasts from this WAM model run at the European Center for Medium-range Weather Forecasting (ECMWF) finding them reliable out to 5 days in the northern hemisphere and less so in the southern hemisphere.

The worse performance in the southern hemisphere is a common trend in global hindcast products, which is mainly due to the extensive in-situ observations in the northern compared to the southern hemisphere (Chawla *et al.*, 2009). This abundance of wind and wave observations in the north compared to the south led to the first hindcast attempts being north hemisphere based (Corson and Resio, 1981; Kushnir *et al.*, 1997; Günther *et al.*, 1998). These studies successfully assessed the long-term variability in the North Atlantic and North Pacific basins. Kushnir *et al.* (1997) significantly linked the variations to mean sea level pressure (MSLP) changes and the North Atlantic Oscillation (NAO). Gutnther *et al.* (1998) inferred significant trends and changes in the North Atlantic using US Navy analysis winds driving a 40 year (1954 – 1994) hindcast. These trends were later found to be due to the inhomogeneity in the wind product, leading to creeping within the wave model and highlighting the need for the use of homogeneous wind forcing (Cox and Swail, 2001). Ultimately these first hindcasts served as a valuable learning curve for the global numerical weather prediction community and were the first step in understanding the global wave climate and its variability.

2.4 Climate Modes important for the Southern Hemisphere

From the above discussion of wave generation (section 2.1.1), clearly surface winds generated by extratropical cyclones of the mid to high southern latitudes directly control the energy input to the underlying wavefield through wind stress. Variations in the intensity and positions of these systems directly cause variations in the wave climate of much of the southern hemisphere, therefore understanding the driver of these changes is vital to understand long-term wave variability. Within the climate system there exist several large-scale modes of climate variability. These generally consist of reoccurring shifts in atmospheric mass or oceanic heat content and ultimately drive shifts in both the position, frequency, and intensity of these wave-generating systems.

The Southern Annular Mode or Antarctic Oscillation (SAM) is the principal mode of variability for the extra-tropical southern hemisphere and has been shown to explain 30% of its climate variability (Thompson and Solomon, 2002; Gillett *et al.*, 2006). Arising from a positive feedback loop between average zonal wind anomalies and eddy momentum flux it has a timescale of around 2 weeks (Lorenz and Hartmann, 2001). The changes to the westerly flow affect the baroclinicity of the mid and high latitudes leading to opposing baroclinic anomalies which ultimately shift the extratropical cyclones and positively feedback on the original baroclinic anomalies (Thompson and Wallace, 2000; Birkett, 2010). The phase of SAM describes the zonally symmetric shift of atmospheric mass, pressure

gradients, and the westerly wind belt between the mid and high southern latitudes. In its positive (negative) phase mass shifts equatorward (poleward), westerlies between 30ºS and 50ºS weaken (strengthen) and negative (positive) pressure anomalies over Antarctica (Gillett *et al.*, 2006; Veitch *et al.*, 2019). These shifts, in turn, significantly affect rainfall and ocean waves across the southern hemisphere (Wang and Swail, 2002; Silvestri and Vera, 2003; Reason and Rouault, 2005; Hemer, Church and Hunter, 2010; Marshall *et al.*, 2018). SAM is most active between October and December due to changes in stratospheric ozone levels (Thompson and Wallace, 2000). During this period, the phase of SAM indirectly impacts the strength of the mid-latitude westerlies and the positions of extratropical cyclones.

Like SAM, the El Niño Southern Oscillation (ENSO) seasonally impacts southern hemisphere climate, with the strongest and most direct impacts occurring in the Pacific sector during the mature phase of ENSO events (austral summer). ENSO is a phenomenon occurring in the tropical Indo-Pacific with basin-scale changes in the trade winds, sea surface temperature (SST), and atmospheric circulation that occurs with a 2 – 8-year period. It consists of two phases, El Niño (positive) and La Niña (negative) which are best described by the mean SST anomalies between 5ºN – 5ºS, 170 ºW – 120ºW (Niño3.4 region). On average, there is lower surface pressure and ascending air over Indonesia (west Pacific) and higher surface pressure and descending air over South America (east Pacific), completing the Pacific cell of the Walker circulation. An El Niño event occurs when the central to east equatorial Pacific Ocean warms, the equatorial trades slacken and the Pacific Walker circulation cell splits into 2 cells, with ascending air over the dateline and the eastern equatorial Pacific and descending air east of the dateline and over the west equatorial Pacific. La Niña events are in the simplest terms an intensification of the average conditions: colder water in the eastern equatorial Pacific, and stronger than average east-west pressure gradient, and equatorial trade winds.

It achieves global scale impacts primarily through the modification of both the Walker circulation and the Pacific equator to pole temperature gradient, which in turn drives changes in the pressure fields across the southern hemisphere leading to negative (positive) mean sea level pressure (MSLP) anomalies over the mid-latitude Indian, Atlantic, and Pacific Oceans during El Niño (La Niña) events. During El Niño events the increased meridional pressure gradient causes the Hadley cell to contract and strengthen, leading to a stronger subtropical jet and more northerly Pacific storm track, however, the northward shift in the storm tracks does not hold across the hemisphere. In the South Atlantic, due to descending air over the Atlantic associated with the shift in the Walker circulation the Atlantic Hadley cell weakens and expands, the subtropical jet strengthens and shifts southward leading to anomalously south storm tracks (Rind *et al.*, 2001; Ashok *et al.*, 2007; Birkett, 2010). The South Atlantic MSLP response to ENSO was investigated by (Colberg *et al.* , 2004), finding that during El Niño events a negative MSLP anomaly exists implying weaker southeasterly trade-winds. Rouault *et*

al. (2010) similarly found that during El Niño (La Niña) events the prevailing summer southeasterly winds decrease (increase).

Since the early 1990s, the ENSO has begun to significantly interact with the SAM. This is primarily due to a shift in ENSO from an eastern-basin type toward a more central Pacific/Modoki ENSO (Ashok and Yamagata, 2009) and the ability of these events to modify the Hadley cell. Lim *et al.* (2013) used the Australian Bureau of Meteorology seasonal forecast system to investigate this association and the possibility for providing seasonal forecasts of the SAM, which are currently only reliable out to 10 days. They found the significance in the ability of ENSO to predict the SAM to depend on the timing and type of event. Central Pacific El Niño (La Niña) events significantly predict negative (positive) SAM in the late austral autumn to early winter months, whereas canonical El Niño (La Niña) events significantly predict negative (positive) SAM in the late austral spring to summer months (Lim *et al.*, 2013). Similarly, the mid-basin ENSO was found by (Yu *et al.*, 2015) to modulate SAM after the early 1990s, which has led to ENSO having a stronger influence on Southern Hemisphere climate post-1990s. On top of this strengthening ENSO relationship, the SAM has been found to be trending toward a positive phase, in line with research showing the expansion of the Hadley cell due to current climate change-induced heating (Previdi and Liepert, 2007; Nguyen *et al.*, 2018; Burls, Blamey, B.A. Cash, *et al.*, 2019; Fahad, Burls and Strasberg, 2020). The SAM is not the only large-scale mode showing the signal of a changing climate.

The final mode of relevance to this discussion of Southern Hemisphere climate is the semiannual oscillation (SAO). The SAO describes changes in the circumpolar trough in its latitudinal extent and is measured through the difference in mean zonal 500hPa temperature between 50ºS and 65ºS (van Loon, 1967). This trough moves poleward and deepens in summer and winter and moves equatorward and weakens over the transition seasons leading to mid-latitude (35 – 60ºS) pressure and geopotential height maxima in the transition seasons and minima over early winter and summer (van Loon, 1967; Burnett and McNicoll, 2000). These delayed peaks are caused by the lag in the annual cycles of SST and sea ice extent.

A weaker SAO implies a stronger meridional equatorward flow over the South Atlantic and a contraction of the mid-latitude polar vortex (Burnett and McNicoll, 2000). Research has highlighted a weakening in the winter to spring SAO since 1979 (Hurrell and van Loon, 1994; Meehl, Hurrell and Loon, 1998), in which the spring MSLP maxima disappears. This weakening has significantly impacted not only the meridional flow in the South Atlantic, but also the seasonal occurrence of cut-off lows around the South African coastline. Singleton and Reason (2007) found the 1980 changes in the SAO to drive a shift in the seasonality of cut-off lows, shifting from March-May to July-August. From the above discussion, clearly extratropical cyclones and their surface winds vary significantly with respect to these large-scale modes. As interannual to inter-seasonal variability in these systems

directly drives the variations in the wavefield, it comes as no surprise that these signals significantly emerge in the wave climate.

2.5 Southern Hemisphere Wave Climate

In the southern hemisphere, ocean waves are primarily generated by the surface winds of eastward propagating extratropical cyclones in the high latitudes. In this hemisphere, there is near-continuous fetch south of 40ºS bar in the Drake passage where South America extends down to 55ºS. The unlimited fetch allows for constant input of energy into the surface ocean through wind stress, generating large waves with a consistent band of strong westerly winds and rough seas present between 40ºS and 50ºS known as the roaring forties. The waves generated propagate great distances affecting the wave climate across the globe. These waves generally arrive at the coastlines of the southern hemisphere continents with an SW to WSW direction as both swell and wind waves depending on whether they escaped the generating system. When the waves can disperse out of the system they arrive as well sorted high energy swells, creating near-perfect ocean waves. Whereas when the waves cannot escape the generating systems, they arrive at the coastline unsorted high energy wind-waves.

The waves arriving at the coastlines of these continents are highly seasonal mainly due to the strong seasonality of the tracks and intensities of these generating systems. The seasonality in these systems is ultimately driven by the development and strength of the Antarctic polar vortex. The Antarctic polar vortex is caused by the strong temperature gradient between the mid and high southern latitudes. The gradient drives the flow of air, which is deflected by the Coriolis force, leading to constant westerly cyclonic flow around the continent from the tropopause (9-11km) up to the stratopause (50km) when fully developed (Schoeberl and Newman, 2015). Over the autumn the Antarctic polar vortex develops, reaching maximum strength over the winter and eventually breaking down in spring. When fully developed the extratropical cyclones shift equatorward, the fetch area grows and the ocean is generally rougher, whereas over summer the systems are shifted poleward and less energic and the mid southern latitudes experience a calmer ocean. On top of this seasonal variation, the generating systems are also subject to shifts of atmospheric mass related to the large-scale modes of climate variability discussed above which can act to enhance or dampen the seasonal response through changes in the Antarctic polar vortex.

2.5.1 The Role of Large-Scale Modes of Climate Variability

The idea that ocean waves significantly respond to these modes was first investigated in the 1990s. Early research showed significant links between North Atlantic wave variability and the North Atlantic Oscillation (Kushnir *et al.*, 1997; A Sterl, Komen and Cotton, 1998), North Pacific high

wave energy events and the El Niño Southern Oscillation (Seymour *et al.*, 1985; Seymour, 1996), as well as the south-east Australian wave climate and ENSO (Phinn and Hastings, 1992). These early studies alerted the research community to the possibility to predict the severity of the coming season's wave events given the skill emerging in seasonal ENSO forecasting.

Through the early 2000s, a more comprehensive view of the southern hemisphere wave climate was achieved. These papers highlighted the global impact of large swells generated in the mid to high southern latitudes and sparked a greater interest in understanding the southern hemisphere wave variability due to the far-reaching impacts of large swells generated in its near-continuous fetch (Young, 1999a; Cox and Swail, 2001). Work throughout this decade ultimately culminated in the (Hemer, Church and Hunter, 2010)'s assessment of southern hemisphere wave variability.

Hemer *et al.* (2010) assessed inter-seasonal to interannual variations and trends against both the Southern Oscillation Index (SOI) and the Southern Annular Mode (SAM) and found significant inverse relationships with ENSO that shifts from the western south equatorial Pacific (winter and transition seasons) eastward over the summer months. The equatorial South Indian Ocean responds significantly in the western portion over summer in phase with ENSO. There was little influence over the South Atlantic bar a few small significant patches in summer. In the high southern latitudes, only the Eastern Pacific sector responds significantly in the Drake passage during winter in direct relation to the SOI (Hemer, Church and Hunter, 2010). The second mode investigated was the SAM, which showed a much larger influence. Year-round the wave energy around Antarctica is directly related to SAM, with the strongest impacts during autumn and winter. In autumn, the direct relationship extends across much of the western South Pacific, which also significantly responds over the winter. Summer shows strong inverse relationships across the South Atlantic and Indian Oceans, significantly impacting the coasts of both South Africa and Australia. The South Atlantic also responds similarly in both winter and spring (Hemer, Church and Hunter, 2010). These results showed how similar the effects of SAM on southern hemisphere winds are to the effects on the waves and were backed up by similar research using an updated hindcast (Stopa *et al.*, 2013).

Around this time, the research community was realizing the significance of ENSO in modulating SAM, with a tendency towards out of phase co-occurrences emerging since the 1990s as well as the increasing ability of ENSO to seasonally influence the SAM phase over late autumn to early winter months and late spring to summer months (Ashok and Yamagata, 2009; Lim *et al.*, 2013; Yu *et al.*, 2015). As mentioned above, the ability to drive changes in SAM depends directly on the type of ENSO event, but generally, El Niño is associated with negative SAM. This association and its promising ability to forecast SAM led to more thorough investigations into the role of these modes (Marshall *et al.*, 2018; Kumar *et al.*, 2019; Godoi and Torres Júnior, 2020). The main practical use of these modal relations is their predictability which can allow for weekly to seasonal forecasts of the

probable wave conditions. Marshall *et al.* (2018) showed the influence of the SAM on the global wind and wave climate, highlighting the differing responses to positive vs. negative phases and the role of the El Nino Southern Oscillation in damping the connections to Northern Hemisphere climate variations.

The idea is now that the variability is better understood through the co-occurrence of different phases of these large-scale modes. Kumar *et al.* (2018) studied the combined influence of SAM, ENSO, and the Indian Ocean Dipole (IOD) on the Indian Ocean wave climate using the ERA 20C product. Through partial regression analysis, the results revealed that for austral winter and spring an out of (in) phase ENSO – IOD relation serves to enhance (dampen) the wind and wave response. The IOD was also found to dampen the effect of SAM in the tropical and northern Indian oceans during spring. Recently, a similar method has been used by Godoi *et al.* (2020) and Godoi and Torres Junior (2020) to study the global influence of ENSO – Madden-Julian Oscillation (MJO) and SAM – ENSO combinations between November and March between 1979-2018 using a Wavewatch 3 CAWCR hindcast (Durrant *et al.*, 2014). The SAM – ENSO results show that previous research attributing an increase in Southern Ocean wave heights to ENSO were actually due to the SAM association, and that when a negative SAM phase combines with an El Niño event, the southern South Atlantic waves increase more so than when just a negative SAM is present, significantly impacting the summer wave climate of the southern African coastline.

The third mode of relevance to the SH wind and therefore wave variability investigated here is the semi-annual oscillation (SAO). Although the impacts on the southern hemisphere pressure, meridional wind, and strength of the Antarctic circumpolar trough are reasonably well understood, there has been little to no research into the potential impacts on the underlying wave spectrum. Based on the known impacts the SAO has on both the meridional flow and frequency of cut-off lows around the South African coastline (Singleton and Reason, 2007), it appears that waves might be similarly affected, becoming more meridional and more wind-sea dominated (near-coast generation) under a weaker SAO. The recent research into the southern to eastern coastlines' wave variability highlights the importance of cut-off lows on generating high wave energy flux over this section of coastline (Jury, 2019). Overall, these 3 modes have the potential to describe southern hemisphere wave climate variability, but questions remain into how these waves have changed over time and how future climate change will impact their characteristics.

2.6 Long Term Trends and Waves in a Changing Climate

As the Earth's climate changes and warms there is a net increase in the energy within the system. This warming has primarily been absorbed by the oceans, leading to the general increase in SSTs observed (Reguero *et al.*, 2019; Lyu *et al.*, 2020). These warm SSTs provide more energy to the overlying

atmosphere, leading to more energetic weather systems. A more energetic cyclonic system has much stronger surface winds, which input more energy into the surface ocean as waves. From this simplistic view of global warming's effect on ocean waves, it becomes clear that the global temperature increase should lead to global wave energy increases.

Since the beginning of global wave climate research, there has been a focus on deriving long-term trends (A. Sterl, Komen and Cotton, 1998; Young, 1999a; Cox and Swail, 2001; Hemer, Church and Hunter, 2010; Young, Zieger and Babanin, 2011). Many of these early papers did not have sufficiently long records for robust trends to be derived and had to confirm their results with in-situ data. This led to confidence in the northern hemisphere trends where many observations have been made, but a lack of in the southern hemisphere trends. Hemer *et al.* (2010) provided the first reliable estimates of southern hemisphere wave climate trends, finding significant regional increases in significant wave height around the hemisphere that varied monthly. Young *et al.* (2011) similarly assessed trends, but also looked at 90th and 99th percentile trends finding these extremes were increasing faster than the means.

From the above discussions of both long-term trends, and relationships with large-scale modes of variability, particularly SAM, clearly changes in the southern hemisphere wavefields are occurring.

The above discussion of long-term trends highlights clear changes in the southern hemisphere wavefields in line with anthropogenic induced climate change. More recently the basin-scale trends in all ocean basins were assessed, finding a significant increase in all basins that was linked to rising ocean temperatures (Reguero *et al.*, 2019). This trend was most prominent in the Southern Ocean, with an increase of 0.58% per annum since 1948 found, which was later confirmed using both altimeter and ERA5 reanalysis data (Young and Ribal, 2019; Takbash and Young, 2020).

Variations in the waves generated have been previously found to significantly explain 15% of global wave variability and even more so for countries located in the mid-southern latitudes (Caires and Sterl, 2005). Using their empirical relationship between SST and global wave power combined with SST temperature projections under relative concentration pathways (RCP) 2.6 and 8.5, corresponding to 0.6ºC and 2ºC increases in mean global temperature by 2100 respectively, Reguero *et al.* (2019) estimated that global wave energy flux would increase by between 32% and 122% by the end of this century, in line with an Hs increase ranging between 16% and 48%. These estimates are higher than, but in agreement with those projected in other recent wave climate research (Morim *et al.*, 2019; Meucci *et al.*, 2020).

Morim *et al.* (2019) found that ~50% of the world's coastline will be impacted by changes in at least one wave variable (height, period, or direction). They highlighted the need to use ensemble

projections which allow for much more robust projections of the future changes. Relevant to South Africa, they found a significant decreasing trend in wave direction (anticlockwise rotation) up to 3º under RCP 8.5, which represents the projected climate for 2100 under a business-as-usual scenario where there is no reduction in CO_2 emissions and a global temperature increase of around 4ºC. Similarly, Meucci *et al*. (2020) assessed Hs changes by the end of the 21st century relative to the 1979-2005 period using ensemble projections under RCP 4.5 and RCP 8.5. Finding the 100-year return Hs to be increasing by 5% to 15% across the Southern Ocean and around 5% along SA's southern coastline.

Given these projections of future wave climate combined with the projections of sea-level rise, we can expect significant changes to occur along the Southern African coast. These changes will drive a stronger northward alongshore sediment flux as well as more severe episodic erosion combined with the increase in river dam construction and coastal mining could significantly deplete areas of the Southern African coastline. In order to better understand the changes and variability particular to the South African coastline, our discussion must shift to a more detailed discussion of the waves and their drivers around the coast.

2.7 A Regional Perspective: South Africa

2.7.1 Regional Atmospheric forcing

High wave energy flux regularly impacts the South African coastline. This wave energy originates from the South Atlantic, Southwest Indian, and Southern Oceans where it is generated by strong surface winds associated with the passage of low-pressure systems such as extratropical cyclones, cut-off lows, and occasionally tropical cyclones. The intensity and paths of these systems are ultimately controlled by variations in the atmospheric pressure field, which are driven by variations in the distribution of energy in the atmosphere and ocean in an attempt to balance the net heating in the low southern latitudes with the net cooling of the high southern latitudes.

In the tropics, there is a net heating, causing the air to rise in the ascending branch of the Hadley Cell and travel poleward in the upper levels. As it flows poleward, the air cools and sinks in the subtropics completing the Hadley cell. This sinking air causes the anticyclonic high-pressure circulation responsible for the subtropical ridge. Poleward of the Hadley cell a strong thermal gradient exists which drives the westerly flow characteristic of the mid-latitudes. Within this mean westerly flow, there can be two high-level jet streams: the subtropical jet, and the subpolar jet. During summer, the polar vortex contracts, and the two jet streams merge, whereas in winter they split, and the mid-latitude weather systems can travel further north. Meanders in this upper-level flow combined with the strong thermal gradient leads to high baroclinicity, favoring the formation of cyclonic disturbances which deepen into the extratropical cyclones forming the circumpolar trough.

These systems dominate the variability in the wave record creating large swells as they propagate eastward across the South Atlantic and Southern Oceans. They are generated due to baroclinic instability in the mean westerly flow of the high southern latitudes deepening as they propagate, developing warm and cold fronts. Due both to the intense wind speeds and the large areas of uniform winds around the systems (fetch), they input significant energy into the underlying ocean in the form of ocean surface waves. These waves propagate with the systems continuing to receive energy if they move under strong surface winds or, dispersing out the fetch arriving at the coastline as well sorted swell waves. The cold fronts of these extratropical systems either make landfall on the southwest coastline of South Africa or pass just south of the continent depending on the position of the South Atlantic and South Indian Ocean Anticyclones.

These anticyclonic near stationary systems are the other dominant feature of the southern African climate, inducing strong meridional flow along both the western and eastern coastlines and subsidence over the subtropical South Atlantic and South Indian oceans. Over the summer months, these systems spread out and are centered more poleward, acting as high-pressure barriers to the passing extratropical cyclones. Whereas over winter, this high-pressure band is located further north, allowing for the cold fronts of these systems to make landfall with an approximate 3 – 5-day cycle (Reason, 2017).

The most intense wave energy events are characterized by continued generation until they arrive at the coastline and are therefore more common over winter when the mid-latitude weather systems can propagate further north. They arrive with a general SW to WSW direction and travel up both the western and eastern coastlines. Here they encounter the strong Agulhas current which, due to the near-perfect opposing direction of these storm waves, can lead to extremely large rogue waves and cause substantial damage to the offshore shipping industry (Barnes and Rautenbach, 2020).
Also important to the wave climate around southern African are cut-off low systems. These are cold-core systems that form in the upper troposphere on the equatorward side of the subtropical jet, becoming cut-off from the mean westerly flow and often have an anomalously south ridging high pressure behind them (Singleton and Reason, 2007). They are almost always associated with Rossby wave breaking (Ndarana and Waugh, 2010). They have been shown to be particularly important for large wave events along the southern and eastern coastlines of South Africa due to the long fetch created by the interaction between the cut-off low and the following ridging high pressure (Corbella and Strech, 2012; Jury, 2019). Using in-situ data van der Borch van Verwolde, (2004) found that cut-off lows are responsible for 17% and 35% of extreme wave events at the East London and Richards Bay locations respectively. Cut-off lows are most frequent in the transition seasons, leading to significant rainfall and SSW wave energy flux as well as an early or late peak in the climatology when compared to the southwest region. Singleton and Reason (2007) found that the preferred cut-off low

season to be shifting from autumn to late winter/early spring in line with a weakening of the SAO since the 1980s.

The final low-pressure system of importance to South African wave climate are the tropical cyclones which travel down the Mozambique channel and seldomly make landfall over the northern KwaZulu Natal region, bringing large waves and storm surges with them. Their landfall along the South African coast is relatively infrequent, Fitchett and Grab, (2014) found that only 5% of these systems impacted the southeastern African mainland. Often these systems bypass the South African coastline, having a much more significant impact along the Mozambican coast. These systems develop between November and March, with peaks in mid-January and mid-February (Rossouw, 1999). Although only about 5% of these systems currently make landfall on the mainland coast of southeastern Africa (Reason and Keibel, 2004), the waves generated by those passing the coastline will still impart a strong signal in the wave climate. These systems will become more frequent with the global rise in both seas surface and atmospheric temperature (Fitchett and Grab, 2014; Fitchett, 2018). Mawren and Reason, (2017) found a significant increase in the number of intense systems in the western tropical South Indian Ocean related to the general increase in heat content. The systems discussed above significantly control the magnitude of wave energy flux impacting the southern African coastline. The following section assesses the work done on these wavefields up until present.

2.7.2 South African Wave Climate

The regular high wave energy events which have a direct impact on coastal communities and marine operations as well as severe structural erosion have led to many investigations into both the representation and long-term variability of the wave climate surround South Africa. The earliest investigations into the southern African wave climate occurred in the early 1960s in the form of ship-borne echo sounder and accelerometer recordings. These observations gave early researchers an idea of the wave spectra present around the South African coastline (Darbyshire and Darbyshire, 1964). Using data recorded aboard the RV Africana II vessel between 31-38ºS and 15-22ºE over the period 1962 – 1965 (Darbyshire and Pritchard, 1966) found the modal wave height and period to be 3m and 10s respectively. Before the 1970s all wave recordings around the South Africa coast were obtained from ship-borne echo sounders and accelerometers. These observations gave early researchers an idea of the wave spectra and mean wave conditions present around the Southern African coastline, however continuous monitoring was required to understand the nature of South Africa's wave climate (Darbyshire and Darbyshire, 1964; Darbyshire and Pritchard, 1966).

In 1971 a sea tower was erected at Melkbosstrand for the purpose of continuous wave recording, which would give a better understanding of how these waves vary over time. This dataset revealed the pulsed nature of the swells arriving at the southwest coast of South Africa (Shillington, 1974). Shillington (1974) linked the spectral width of these waves to the nature of the generating weather

systems. Narrow spectra were associated with slow-moving fetches with low-pressure centers south of 45ºS, whereas wide spectra are characterized by fast-moving systems with centers between 40 and 45ºS. Later that decade (Shillington and Britten-Jones, 1979) assessed a high wave energy event along the southern coast using in-situ recordings off Port Elizabeth. Their research highlighted the possibility of large period southerly waves due to the interaction of two frontal systems, as well as the devastating effects of a southerly swell interacting with the strong Agulhas current along the South African east coast.

Throughout the 1980s, a more comprehensive view of the waves around the coast was achieved through research and the implementation of in-situ wave buoys around the coastline. Rossouw *et al.* (1982) used all the available in-situ data to gain a view on the distribution of wave heights, direction, and period around the coast. Their analysis revealed that the southwestern and southern coastlines generally receive larger wave heights, periods, and more southwesterly wave directions than the northern western and eastern coastlines. Research on the wave climate up until the 1990s mainly consisted of in-situ observations. Post-1990s, the use of wave models began to gain more traction due to their impressive performance against northern hemisphere in-situ data and their ability to accurately forecast ocean waves, which up until then was done using manual forecasting methods (Laing *et al.*, 1998).

Rossouw and Phelp, (1996) evaluated 2 of these wave models around the South African coastline, the WAM model and a 2nd generation model obtained from the United Kingdom Meteorological Office (UKMO). They found the WAM model 3-day forecasts outperformed the older UKMO model, providing 35% more satisfactory forecasts. However, they only used approximately one month of in-situ data from four locations around the coast and pointed to the necessity of this same evaluation over the winter months.

Around the early 2000s, international studies on the Southern Hemisphere wave climate gained traction. These studies used combinations of in-situ (where available), satellite observations and wave hindcasts to understand the long-term variations and trends in the past wave climate (Young, 1999; Cox and Swail, 2001). Initial links to large-scale atmospheric modes were made, as well as early estimates of trends across the globe. Using only in-situ data around the South African coast the trends were investigated by van der Borch van Verwolde (2004), finding increasing trends in wave height at both the Slangkop and Richards Bay in-situ records. Later in the decade more robust work was done, which confirmed these trends and found significant relations to both ENSO and SAM across the southern hemisphere wavefields (Hemer *et al.*, 2010). Their work also showed significant increasing trends in wave height around the southwest South African coast for both March and August. Birkett (2010) looked at just the Cape Point wave record and its relationships with both SAM and ENSO, finding that SAM significantly impacts the Cape Point wave variability during spring and summer. A

negative SAM was associated with positive wave height and direction (more westerly) anomalies. Similar relationships were found with ENSO, however, these proved less robust and only significant over January and June. The analysis also highlighted the amplified effect during the co-occurrence of out of phase ENSO and SAM, with significantly larger and more westerly waves during negative SAM and positive ENSO particularly over summer months (Birkett, 2010).

The KwaZulu Natal wave climate was assessed using 18 years of in-situ measurements, finding the largest waves tended to occur over autumn and that the largest event on record (Hs of 8.5m 2007) which caused substantial coastal erosion had a 32-year return period and was associated with cut-off low wave generation Corbella and Strech (2012a). Corbella and Stretch (2012b) then combined this data with beach profile data stretching from the Bluff to up to the North Coast. They found significant decreasing trends in the beach volume across much of the measuring sites. Although they found some weak increasing trends in the 18 years of in-situ wave data, no significance was found in wave height and the net loss of sand was attributed to recent dam construction and river sand mining which lowered the sediment supply. Interestingly they found a 4.5-year cycle in tidal range coincided with increases in the frequency of large wave events. This phase-locking could enhance the coastal impacts of storm events as large waves push the mean sea-level up through the storm surge effect.

All the assessments so far have noted the high energy environment of particularly the south and southwest coastlines. Although this high energy can prove detrimental to coastal communities, it also has the potential to become part of a green solution to South Africa's current energy crisis. Joubert, (2008) used a high-resolution coastal model to map the southwest coasts wave energy distribution, noting the potential of wave energy converters to generate significant electricity if able to harness the long-period southwesterly swells characteristic of this region. The regions seasonal average wave power (wave energy flux) ranged from 20 kW/m (summer) to 50kW/m (winter), with specific focal points identified. Building on this work Joubert and van Niekerk, (2013) increased the shallow water model resolution obtaining an even more detailed view of the general wave energy distribution, focusing on the Granger Bay area as a potential deployment site for a wave energy converter. These papers are significant as they provide some of the first high-resolution shallow water wave model hindcast data computed for the South African coastline. Shallow water wave models also allowed for the study of high-resolution wave variability around communities that directly depend on the ocean.

Lyttle *et al.* (2018) studied the nearshore wave variability along the South Coast using both a high resolution near-coast SWAN model driven by NCEP/NCAR winds over the period 1994 – 2014 (Theron *et al.*, 2014) and interviews with local fishermen. They found that the sub-daily wave variability has increased particularly over the wind-sea dominated summer months, in line with other research showing a shift in the South Atlantic High favoring stronger winds surrounding the study area. This regime shift was detected post-2006, where daily wave variations became more pronounced

in the 2007-2014 period compared to the 1994-2006 period. This was attributed to the lengthening of summer as well as the increase in southeasterly winds in the latter period and was also noted by the local fishing communities. Lyttle *et al.* (2018) also postulated the influence of SAM on the changes seen in the wave variability.

The influence of both SAM and ENSO in the Cape Point wave record was assessed by Veitch *et al.* (2019). Using data between 1979 – 2010, a high wave and low wave regime were detected. Noting that the 1979-1992 period had higher and more westerly waves than 1994-2006 where lower and more southerly waves were observed. This change was attributed to SAM and ENSO phase-locking and more prominent positive SAM and negative ENSO compared to the latter period. The wave record showed significant responses to SAM over both summer and winter, and ENSO mainly over summer months, with the response amplified during out of phase periods. Research into the meteorological controls on large wave energy events off East London found that the 6 largest SSW 2-day duration wave events on record were associated with slow-moving cut-off low systems that occurred during negative phases of SAM (Jury, 2019). The response to SAM is not linear, i.e. the largest events do not correspond to the largest negative SAM phase (Jury, 2019).

Around this time, the performance of global wave models against 2 years of in-situ data was assessed, finding the Meteo France Wave Model (MFWAM) outperformed both the ERA-Interim and NCEP hindcasts (Gweba and Krug, 2019). On top of this, the South African Weather Service (SAWS) released its high-resolution wave, tide, and storm surge data through the SAWS marine portal (Morris *et al.*, 2019). This represents a huge step forward in marine forecasting along our coastline with nested grids up to 2km resolution for all the major ports. Using this system and hindcasted current fields Barnes and Rautenbach (2020) were able to assess the impact of the strong Agulhas current on the wavefields. Finding up to 60% amplification in wave heights, particularly during near-coast generated storm waves travelling with an SW-SSW direction. This coupled model was then implemented using CMEMS current forecast to forecast wave-current interactions out to 3 days, becoming the first wave-current coupled operational forecast for the region (Barnes and Rautenbach, 2020).

The research in this thesis aims to extend the work of Veitch *et al.* (2019) to the whole Southern African coastline and surrounding oceans aiming to gain a holistic view of the role of large-scale atmospheric modes. It will follow a similar method as recent global research (Marshall *et al.*, 2018; Godoi and Torres Júnior, 2020; Takbash and Young 2020). Although using a high resolution coupled wave model would provide a better representation of the current-wave-atmosphere feedback mechanisms and wave field modifications, unfortunately, a freely available wave-current coupled product does not currently exist. Instead, this research uses the latest freely available ocean wave hindcasts to address two main questions: first to determine which product best represents the Southern

African wave climate and second to use the most representative product to show how these waves have changed over time particularly concerning the phases of large-scale climate modes

3. Data and Methods

3.1 Wave Data

3.1.1 Buoy Data

The Council for Scientific Industrial Research (CSIR) has been recording wave data along the South African coastline using in-situ wave buoys since 1978. Figure 3 shows the locations of these buoys and Table 1 describes each data record. There have been several different wave recorders used throughout the observation period. They can generally be split into directional and non-directional types (Birkett, 2010). Non-directional buoys measure significant wave height (Hs), maximum wave height (Hmax), peak period (Tp), average zero down-crossing wave period (Tz), spectral crest period (Tcz), and mean wave period (Mwp). The directional buoys add peak direction (Dp) and peak spreading factor (Fs) to the list. Directional measurements started at Cape Point in October 1998, later these were also made at East London, Richards Bay, Durban, and the Port of Ngqura.

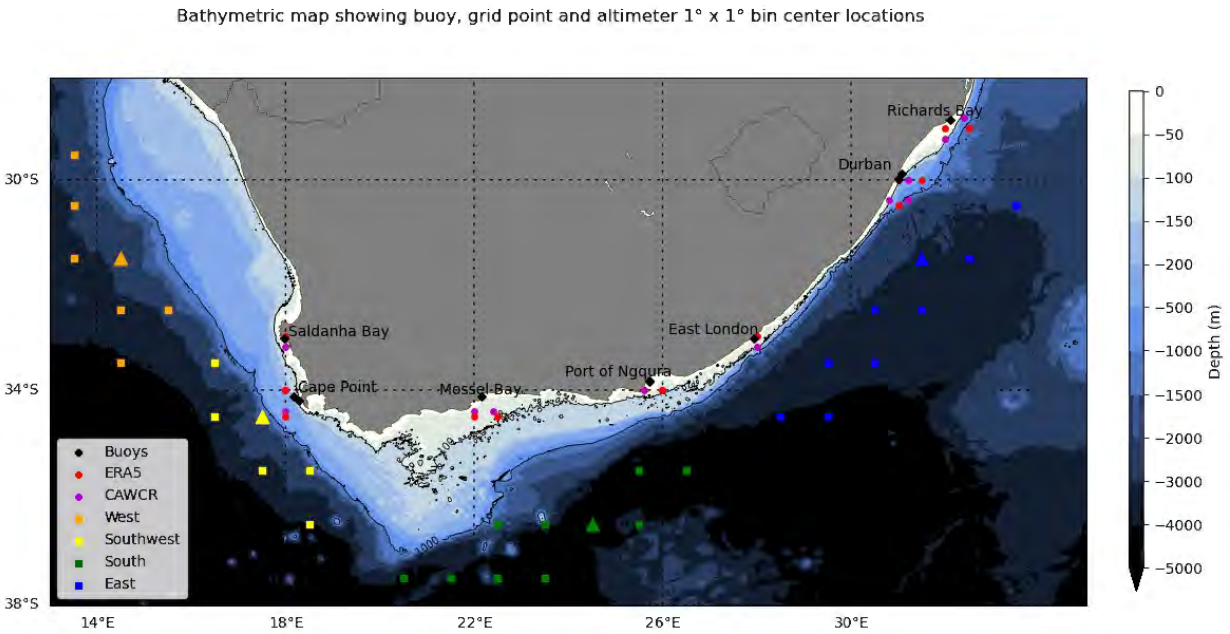

Figure 3: GEBCO 2020 15 arcsec bathymetry. Shows the buoy locations (black diamonds), the chosen grid points (red (ERA5) and purple (CAWCR) dots), and the center of the offshore (>50km) 1º x 1º altimeter bins coloured by region (orange, yellow, green, and red squares). The coloured triangles represent the offshore nodes used to assess the long-term variability, with the region following the same name as the squares. The contour lines represent the – 1000m and – 100m depths.

Most of the wave data are recorded in shallow to intermediate water depths (Table 1, water depth). Only the Slangkop station (pre-1990s Cape Point buoy location) can be considered deep-water for wave periods < 15s. For all other stations, the wave height and direction measurements will be significantly influenced by the local headlands and bathymetry when compared to the offshore wavefield. Keeping these shallow water discrepancies in mind, the dataset is used as ground truth to evaluate wave model hindcasts along the South African coastline as well as to validate the offshore altimeter-derived wave climate. It is expected that persistent biases will arise due to the difference in geographic location and the low resolution of the hindcast products. These in situ datasets will also be used to assess whether the relations to the large-scale climate modes translate to the coastal zone.

Buoy location:	**Latitude (ºS)**	**Longitude (ºE)**	**Water Depth (m)**	**Recording Period**	**Frequency**	**Variables**	**Hs % availability**
Saldanha Bay (SB)	33.05	17.98	23	1981-05-01 – 1987-03-17 ;1991-11-08 – 2020-05-31	6 hourly, 3 hourly	Hs, Hmax, Tp, Tz, Tcz, MWP	90%
Slangkop (SL)	34.13	18.18	170	1978-10-03 – 1989-09-28 ;1989-09-28 – 1993-05-14	6-hourly, 3-hourly	Hs, Hmax, Tp, Tz, Tcz, MWP	80%
Cape Point (CP)	34.20	18.29	70	1994-06-07 – 2020-05-31	3-hourly	Hs, Hmax, Tp, Tz, Tcz, MWP, Dp, Fs	92%
Mossel Bay (MB)	34.12	22.15	24	2007-05-22 – 2020-05-31	3-hourly	Hs, Hmax, Tp, Tz, Tcz, MWP	95%
Port of Ngqura (PN)	33.83	25.72	21	2011-03-05 – 2020-05-31	3-hourly	Hs, Hmax, Tp, Dp, Fs	94%
East London (EL)	33.04	27.93	27	1992-04-28 – 2020-05-31	3-hourly	Hs, Hmax, Tp, Tz, Tcz, MWP, Dp, Fs	80%
Cooper Light (CL)	29.99	30.99	42	1992-08-11 – 2001-10-31	3-hourly	Hs, Hmax, Tp, Tz, Tc, MWP	74%
Durban (DB)	29.88	31.07	30	2007-08-23 – 2020-05-31	3-hourly	Hs, Hmax, Tp, Tz, Dp, Fs	91%

Richards Bay (RB)	28.83	32.10	22	1979-01-02 – 1989-10-25 ;1989-10-25 – 2020-05-31	6-hourly, 3-hourly	Hs, Hmax, Tp, Tz, Tcz, MWP, Dp, Fs	71%

Table 1: A table describing the in-situ data recorded along the South African coastline since 1978.

3.1.2 Altimeter Data

Altimeters have been collecting wave and wind data almost continuously since the launch of Geosat in 1985 bar a 1-year, 8-month period between the Geosat and ERS1 missions. The full list of altimeters used as well as their mission and return periods are seen in Figure 4. The use of this long-term dataset requires large amounts of pre-processing and extensive validation against offshore in situ wave and wind data. Fortunately, this gap between the acquisition and use of the data has been filled by both Young, Sanina and Babanin, (2017) through the RADWave project, as well as by the AVISO team.

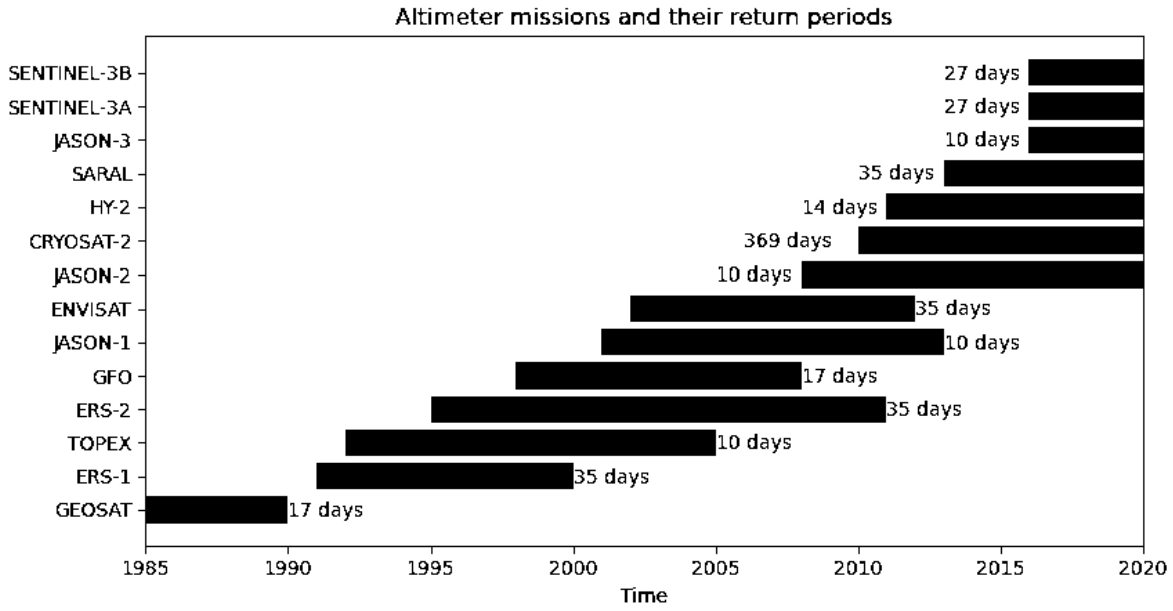

Figure 4: All the altimeter missions used in this study and their respective return periods.

Using all the openly available altimeter data, Young, Sanina and Babanin, (2017) created a calibrated global wind/wave dataset containing all the quality-controlled available data since 1985. See Young, Sanina and Babanin, (2017) for details on the calibration and validation of this dataset. It is openly available through the Australian Ocean Data Network (AODN) as raw NetCDF files or through the co-developed python package RADWave (https://radwave.readthedocs.io/en/latest/). Subsets of all the available altimeter data can be made, and a list of their paths downloaded. This list can then be parsed to the RADWave python functions for acquisition and analysis.

In this thesis, all available altimeter significant wave height and period data are used to assess the performance of the offshore wave hindcasts around the Southern African coast where offshore is defined as > 50 km from the coastline. It is necessary to exclude data near the coast due to moisture gradients between the land and the ocean interfering with the return signal used to measure wave heights. Along-track measurements are made at ~ 1 Hz, with a spatial footprint of 6 – 10km. These offshore satellite tracks are spatially binned into 1º x 1º boxes. For each box, all data is resampled to a daily frequency and the missing values are dropped. The remaining time series is assumed to represent the central point of each box, which is grouped by region: west, southwest, south, and east (Figure 3). This dataset is then used to regionally assess the wave hindcasts.

In terms of assessing performance across the South Atlantic basin, it is more useful to compare Hs fields. AVISO provides a level 4 processed altimeter dataset on a 1º x 1º spatial grid (https://aviso.altimetry.fr). It contains all the altimeter data recorded by Jason-3, Sentinel-3A, and SARAL/Altika between 2009 and 2019 at a daily frequency and will be used to seasonally assess hindcasts performance across the South Atlantic basin.

3.1.3 Wave Models

Several freely available ocean wave hindcasts have been conducted by various research centres around the world. This thesis uses 2 of the most recently updated versions of these hindcasts to assess performance along the South African coastline and the surrounding oceans. The Centre for Australian Weather Research (CAWCR) used the CFSR (0.33º) and CFSv2 (0.125º) winds with a native 38km resolution to drive a 40-year global wave hindcast with a focus on the Australian and eastern Pacific (Durrant *et al.*, 2014). The hindcast uses WW3 v4.08 from 1979 – 2010 and then version 4.18 from 2010 until the present. No altimeter wave data are assimilated into this product, although the wind forcing product does assimilate and has known inconsistencies making it unsuitable for trend analysis (Smith *et al.*, 2021). For our study region, the data is available at a 0.4 degree spatial and hourly temporal resolution. This open dataset is acquired through the CSIRO and henceforth is referred to as the CAWCR hindcast.

The European Centre for Medium-range Weather Forecasting (ECMWF) recently updated its hindcast database, adding the new and improved European Reanalysis 5 product (ERA5). Unlike the above-mentioned CSIRO product, in ERA5 the atmospheric and ocean models are explicitly coupled allowing for a more accurate representation of the energy fluxes. ERA5 currently covers the period 1979-present with plans to extend the dataset back to 1950 (Hersbach *et al.*, 2020). This dataset uses the ECMWF's 4D-Var data assimilation version CY41R2, which includes, among other data, altimeter wave height data from ERS-1/2, ENVISAT, JASON-1, JASON-2, CRYOSAT-2, and SARAL missions. Although the highest available resolution is 0.3ºx0.3º at an hourly frequency, the Copernicus

Climate Change Service provides an open version which has been interpolated down to 0.5º x 0.5º ocean and 0.25º x 0.25º atmospheric spatial grid and is used in this thesis. The full details, validation, and improvements relative to its predecessor (ERA Interim) of this dataset are available in (Hersbach *et al.*, 2020). The performance of the relevant variables from these respective hindcasts will be assessed against the coastal buoy data as well as the offshore altimeter wave data. The best-performing hindcast will then be used to assess the long-term variability of the wave climate of Southern Africa.

3.2 Climate Indices

The large-scale modes of climate variability are represented by various indices. These are either derived from observed or modelled mean sea level pressure (MSLP), sea surface temperature (SST), geopotential height (GPH), or upper troposphere air temperature (TEMP) data. There is an abundance of research showing how teleconnections to these modes influence wind, precipitation, and ocean waves across the globe (Reason and Rouault, 2005; Singleton and Reason, 2007; Hemer *et al.*, 2010; Marshall *et al.*, 2018; Veitch *et al.*, 2019; Godoi *et al.*, 2019). The required fields (10m winds, SST, MSLP, GPH, and TEMP) are obtained from the chosen reanalysis product. This thesis also uses South Atlantic cyclone tracks from (Gramcianinov *et al.*, 2020) to assess the impact of each mode. Following the leading research, each index known to best represent the mode is derived.

The Southern Annular Mode (SAM) is the leading mode of variability describing ~30% of Southern Hemisphere extra-tropical climate variability (Gong and Wang, 1999; Marshall, 2003). In its positive (negative) phase, the MSLP anomaly at the pole is low (high) and the westerly jet is shifted poleward (equatorward). Following Marshall *et al.* (2018), the SAM index is defined as the leading Empirical Orthogonal Function (EOF) of the weighted (by the cosine of the latitude) monthly mean MSLP anomalies between 25ºS and 75ºS. This gives a monthly SAM index which can be transformed into a daily index by projecting the zonal mean MSLP anomalies onto this monthly index. The phase is defined when the index is greater than 1 standard deviation away from the mean in either direction.

The El Niño Southern Oscillation (ENSO) describes the change in SST, MSLP, and surface winds in the equatorial Pacific. Through the Walker circulation and changes in the Hadley cell, ENSO has global teleconnections which significantly influence sea surface temperature, precipitation, surface winds, sea ice, and ocean waves in the South Atlantic and Southern Oceans (Rind *et al.*, 2001; Colberg *et al.*, 2004; Hemer *et al.*, 2010; Rouault *et al.*, 2010; Veitch *et al.*, 2019; Godoi *et al.*, 2020). ENSO is best represented by the Nino3.4 and Southern Oscillation (SOI) indices. Niño3.4 is defined as the mean SST anomalies between 5ºN – 5ºS, 170 ºW – 120ºW smoothed by a 5-month rolling mean (Trenberth and Stepaniak, 2001). A positive phase (El Niño) occurs when the values exceed 1 standard deviation for 3 consecutive months. La Niña (negative phase) occurs when the values fall

below – 1 standard deviation for 3 consecutive months. The SOI describes this same change but uses observed SLP at Tahiti and Darwin. It is defined as the difference between the normalized monthly mean SLP anomalies at Tahiti – Darwin. The time series is then smoothed by a 5-month running mean with the phase defined as exceeding +-1 standard deviation for 3 consecutive months. The difference between the SOI and Niño3.4 is that a positive SOI phase = La Niña = negative Niño3.4 phase.

The semi-annual oscillation (SAO) describes the twice-annualpeak in mid-latitude pressures over the transition seasons (Hurrell and van Loon, 1994). The strength of the SAO moderates the strength of the South Atlantic and South Indian Ocean anticyclones, thereby significantly impacting cut-off low generation around the South African coast (Singleton and Reason, 2007). These systems are associated with large-wave events along the southern and eastern coastlines of South Africa (van der Borch van Verwolde, 2004; Jury, 2019). The SAO is defined as the difference between zonal mean 500hPa air temperature at 50ºS and 65ºS.

3.3 Model Evaluation Strategy

3.3.1 Preparation of Buoy Comparisons

All the buoy locations are in intermediate to shallow water (Figure 1, Table 1). Due to the low spatial resolution and the deep-water nature of the hindcasts, there are no exact co-locations. Figure 3 shows the difference in geographical location between the grid points and the buoys. The shallow water effects caused by sub-grid scale variations in bathymetry will lead to strong biases in significant wave height and peak direction between the hindcast and in situ data. These differences will be considered through the validation process. The mean of the nearest grid points, shown in Figure 3, will be compared to the in-situ data. The grid points were chosen to ensure waves from all the dominant wave directions were captured. The time series are compared through the mean (including climatologies), standard deviation, and bias. They are then transformed into anomalies through the removal of the seasonal signal. These anomaly time series are compared using Pearson correlation coefficients, normalized standard deviation, and normalized centred root mean square difference using Taylor diagrams (Taylor, 2001).

3.3.2 Preparation of Altimeter Comparisons

Wave height and period data derived from radar altimeters are used to assess the offshore performance. Due to the return cycles of the satellites over any given point of the ocean (Figure 4), the dataset is discontinuous in time and there are temporal gaps in between collocated tracks. Along-track, the satellite altimeters record data at a 1Hz temporal and 6-10km spatial frequency. To generate a long-term time series, the altimeter tracks are binned into a 1º square box and then resampled to a daily frequency dropping the missing values/days without data. The centre of these bins are shown in

Figure 3. The model grid points nearest to the centre of the bin which is temporally equivalent to the quasi-daily altimeter data is extracted from the hindcasts. These subsets of the respective hindcasts are then regionally (Figure 3) compared to this binned altimeter dataset using the same method as for the buoys.

This thesis also uses an AVISO gridded level 4 processed satellite dataset to evaluate hindcast performance across the South Atlantic basin. Seasonal composites of each hindcast are compared to the AVISO composites through their biases. As this dataset is not truly daily it is resampled to monthly for this comparison.

3.3.3 Statistical Approach

The hindcast which shows the strongest skill metrics in both the altimeter and buoy evaluations will be deemed the best representation of the South African wave climate. The long-term variability and trends will then be assessed against the large-scale modes of climate variability mentioned above. First, we perform seasonal annual trend analysis on the mean spatial fields of zonal and meridional flux. The trends are assessed using the pre-whitening Mann-Kendall trend estimation method which does not depend on the distribution of the underlying data (Mann, 1945; Kendall, 1948). Only trends significant at the 95% level are discussed.

Next, monthly time series of standardized wave energy flux and direction anomalies for each section of the coastline (west, southwest, south, and east: Figure 3) are used to assess the long-term trends with an 11-month rolling mean as well as create wavelets that show if any periods contain significant cycles. Wavelet analysis provides a powerful way of assessing the significance of the different frequency cycles in a given time series (Sreelakshmi and Bhaskaran, 2020). There are various methods, both normal and complex by which a wavelet can be performed. Here we use the commonly employed Morlet wavelet transform and the red noise process at the 95% significance level using the method of (Torrence and Compo, 1998).

The respective index derived from the best-suited hindcast is assessed against the observation/ model-based index (not shown). This step ensures that the hindcast captures the past variability correctly and is essential to assess the teleconnections within the product. The relations to each mode will be assessed using 2 main methods: detrended spatial correlations and composites. Pearson correlations between the detrended zonal and meridional 10m wind and wave energy flux monthly anomaly fields and the detrended mode of interest are computed for the entire period (1979 – 2020) and using seasonal subsets. Both the timeseries – the climate mode, and each grid node in question – are detrended by removing the linear trend along the time axis. This thesis uses the effective degrees of freedom of the field in question defined by Bretherton *et al.* (1999): $N_{eff} = N[(1 - \rho)/(1 + \rho)]$ where ρ

is the lag-1 autocorrelation. The significance of these correlations is assessed using p-values. Only relationships with >= 95% significance ($p < 0.05$) are shown and discussed.

To further the investigation, composite analysis of the anomaly fields is also performed. The respective index is grouped by its phase. Wave variable anomalies are subset temporally using the positive, negative, and neutral phase of the index. These subsets are used to create a composite map per phase (and per season). A student's t-test, using N_{eff} defined above, is performed assessing whether the positive or negative phase composite is significantly different from the equivalent neutral phase composite. Only composites that are significantly different at >= 95% are shown. This method is done for all the above-mentioned modes.

Often more than one active mode influences the climate, complicating the method used to assess and understand the relationships. Partial correlations and composites grouped by more than one index phase (multi-mode composites) are used to remedy this modal interference. Partial correlations give the relationship between the wavefield anomalies and a climate mode controlling for the influence of the other modes, giving a more realistic view of the actual influence. Whereas composites grouped by more than one phase can show how the influence of a mode is strengthened or weakened by the presence of another mode. Where the seasonal composite and correlation maps show similar patterns of significant influence multi-mode composites will be used to assess how the wave climate responds to this modal interference. Partial correlations are used to assess how the strength of the correlations to the in-situ data changes when controlling for the variability associated with the other modes.

3.4 Evaluation Results

3.4.1 Evaluation Against In-situ Buoy Data

The time series of the mean of the nearest grid points shown in Figure 3 are compared to the in-situ data. The Hs annual cycle is clearly replicated by both hindcasts at most stations, bar Mossel Bay, Port of Ngqura, and the Cooper Light stations which all show a difference in the winter months compared to the observed (Figure 5). At the south coast stations – Port of Ngqura and Mossel Bay – the in-situ climatologies peak in October and not over the winter months as both the offshore hindcasts do. This is attributed to the heavy headland shadowing and shallow water effects which significantly shelter these locations from the large westerly to south-westerly winter swells. The observed climatology at the Cooper Light station has a bi-annual peak over autumn and spring, with an apparent winter minimum whereas the hindcasts do show a slight bimodal peak the in-situ winter trough is not as pronounced.

As expected, there is a positive bias which can in part be attributed to the shallow water effects (Figure 5). The hindcast climatology falls within the in-situ climatology plus one standard deviation

except at the heavily shadowed buoys in water shallower than 30m (Saldanha Bay, Mossel Bay, and Port of Ngqura). The bias is smaller for the deeper water locations (Slangkop, Cape Point, and Cooper Light) than for the shallower stations (Figure 5). ERA5 more accurately matches the in-situ data at west and southwest coast stations whereas the CAWCR shows a more accurate representation at the Mossel Bay, Port of Ngqura, and Cooper Light stations. For the east coast stations – Durban and Richards Bay – ERA5 shows marginally more accuracy over summer. The seasonal cycle progresses from west to east. In the west, it peaks in June, this peak shifts to July in the southwest whereas on the south and east coastline the peak occurs in spring. The later peak as we move eastwards around the coast is due to large wave events being driven by cut-off lows over this region, whereas along the western to southwestern coast these events are driven by extratropical cyclones (van der Borch van Verwolde, 2004; Corbella and Stretch 2012a).

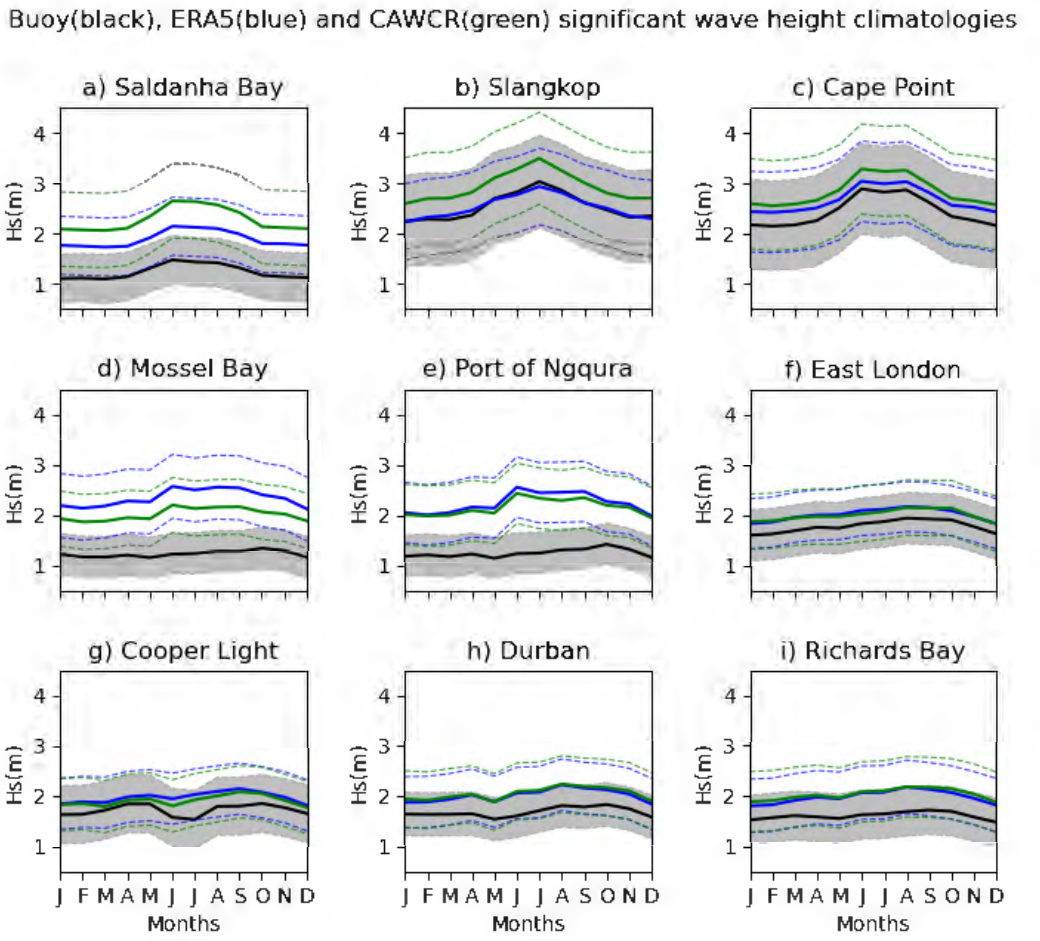

Figure 5: Climatology of Hs for the in-situ data vs ERA5 (blue) and CAWCR (green) per location. The locations go from west to east. The standard deviations of each hindcast are shown by the dotted lines of the corresponding dataset. The in-situ standard deviation is shown by the shaded envelope.

The peak is largest at the southwest coast stations, with lower peak values as we move north up both the west and east coasts. Interestingly there has been a change in the seasonal cycle at the Cape Point station compared to the early Slangkop station which is present in both the hindcasts and therefore is

not due to the change in location. In the Slangkop era, there was a clear winter peak in July, whereas since 1994 the peak splits to both June and August (Figure 5), pointing to a change in the wave climate. The climatologies of peak period and direction are shown in Figures 6 and 7 respectively. Both hindcasts show a much more accurate Tp climatology than they did for Hs. The shallow water effects that modify the Hs field near the coast do not affect Tp as it is conserved when waves move from deep to shallow water. At 4 out of the 8 stations, ERA5 outperforms the CAWCR product although both are well within one standard deviation of the observed. The seasonal cycle is less progressive than it was for Hs with a persistent winter peak. This homogeneity shows the prominence of the large extratropical systems in the generation of large period swells over the winter months.

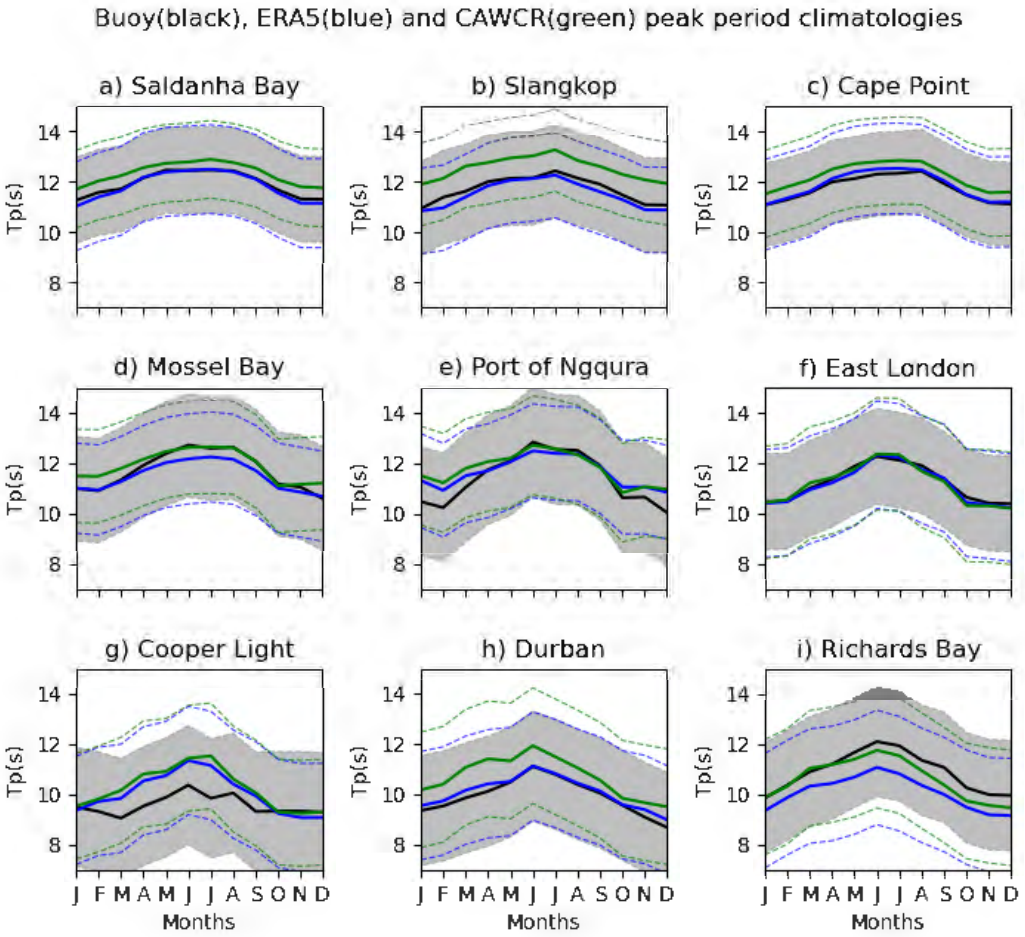

Figure 6: As for Figure 6 but for peak period (Tp).

For wave direction, the variable peak direction (Dp) is measured by the buoys and is available from the CAWCR product however ERA5 only supplies mean wave direction (Mwd). Figure 5 shows much larger discrepancies than the other wave variables. These are due to the shallow water effects, ocean currents, and the difference in wave variables. Closer to the coast, the wave direction becomes orthogonal to the coastline, leading to the generally smaller observed standard deviation than is present in the hindcasts. Only at Cape Point is the standard deviation accurately captured and this is by the CAWCR product, all other stations give large over-estimates of the variability. ERA5's Mwd

does best at Durban and Richards Bay, but it shows a more southerly wave direction at Cape Point over the summer months. From this comparison, we cannot draw real conclusions on which product performs best due to the differences in wave variables.

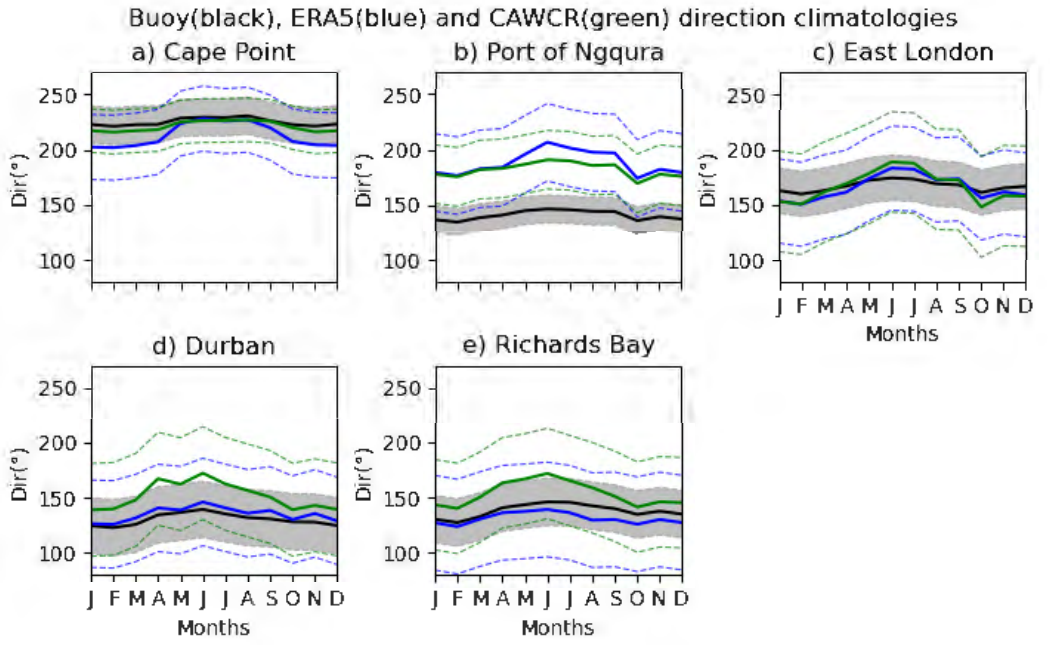

Figure 7: As for figure 4 but for CAWCR and buoy peak direction and ERA5 mean wave direction. Only for stations measuring wave direction.

Both hindcasts capture the annual variability reasonably well considering there are no exact collocations and the shallow water effects are not included. A decision on best performance cannot be made from only the climatology, in fact using this climatology we can create daily anomalies (differences from the climatological mean). The concurrent daily anomalies are compared using scatter plots and Taylor diagrams (Figures 8 and 9). The ERA5 correlation coefficients are slightly higher at 8 of the 9 stations, with the CAWCR only doing better at the Richards Bay station.

Taylor diagrams comparing Pearson correlation coefficients, normalized centred root mean square difference, and normalized standard deviations for each wave variable are shown in Figure 9. Taylor diagrams provide a concise way of evaluating the agreement of time series data using their Pearson correlations, normalized standard deviation, and normalized centred root mean square difference (Taylor, 2001). The normalization of the standard deviation and centred root mean square difference using the in-situ standard deviation allows for multiple co-locations and/or wave variables on the same plot. The actual values are found in Table 2, where the bold text indicates the stronger statistic. At six out of the nine stations, ERA5 outperforms the CAWCR with stronger correlations, closer to the observed standard deviation and smaller normalized centred root mean square difference (Table 2). The CAWCR hindcast does better at the Slangkop, Cape Point, and Mossel Bay stations. Overall ERA5 gives a better representation of the South African coastal significant wave height climate.

The same analysis was done for peak direction and peak period. The equivalent figures and tables are shown in appendix A (Figures A3 and A4; Tables A1 and A2). CAWCR gives a more realistic peak direction climate at 4 of the 5 stations however, ERA5's data is for the mean as opposed to the peak wave direction. For peak period ERA5 outperforms the CAWCR hindcast at all stations (appendix A, Table A1). This coastal wave data evaluation points to ERA5 as the more realistic hindcast for this region. The final step is an evaluation of the deep-water performance using satellite altimeter data.

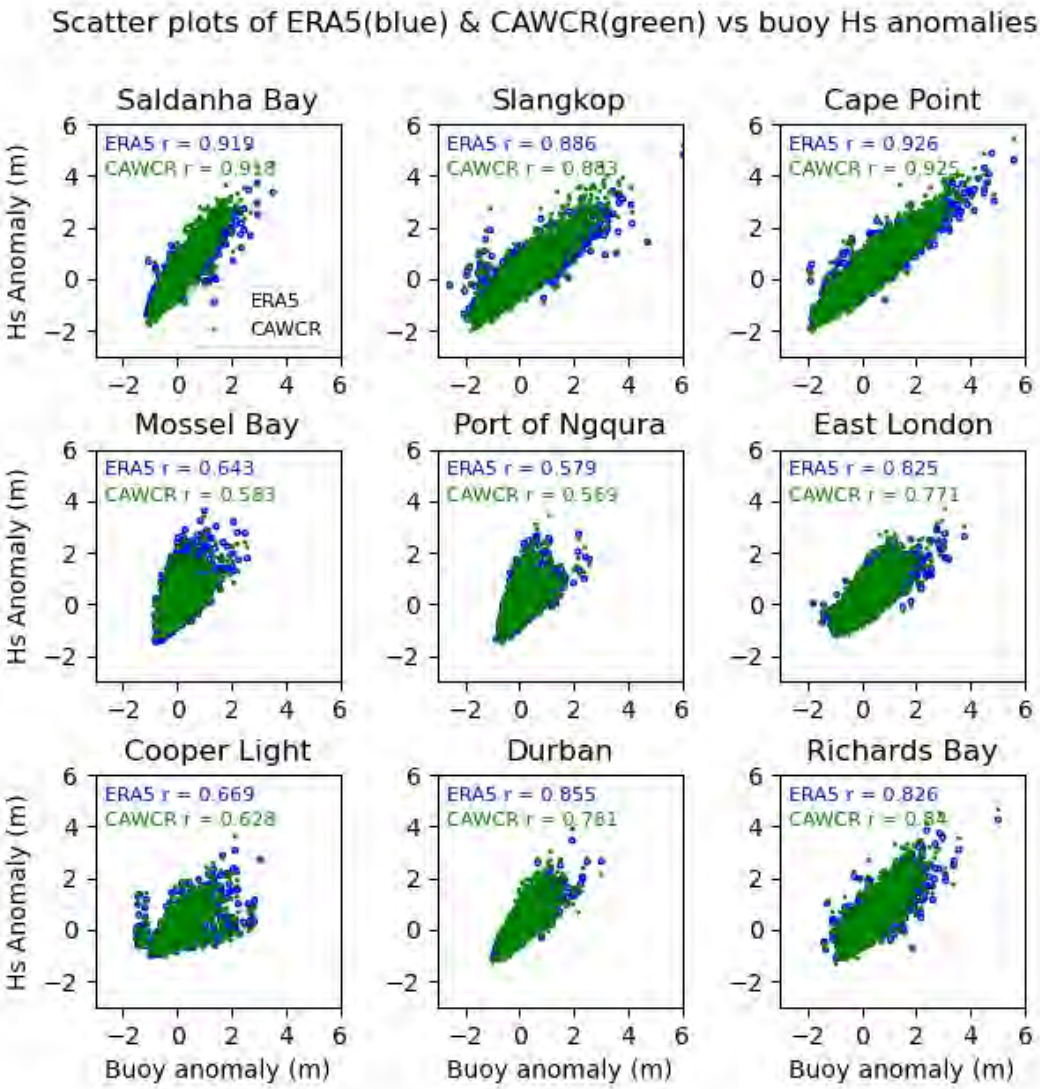

Figure 8: Scatter plots of ERA5 and CAWCR Hs anomalies vs in-situ buoy anomalies. Pearson correlation coefficients are shown on each plot.

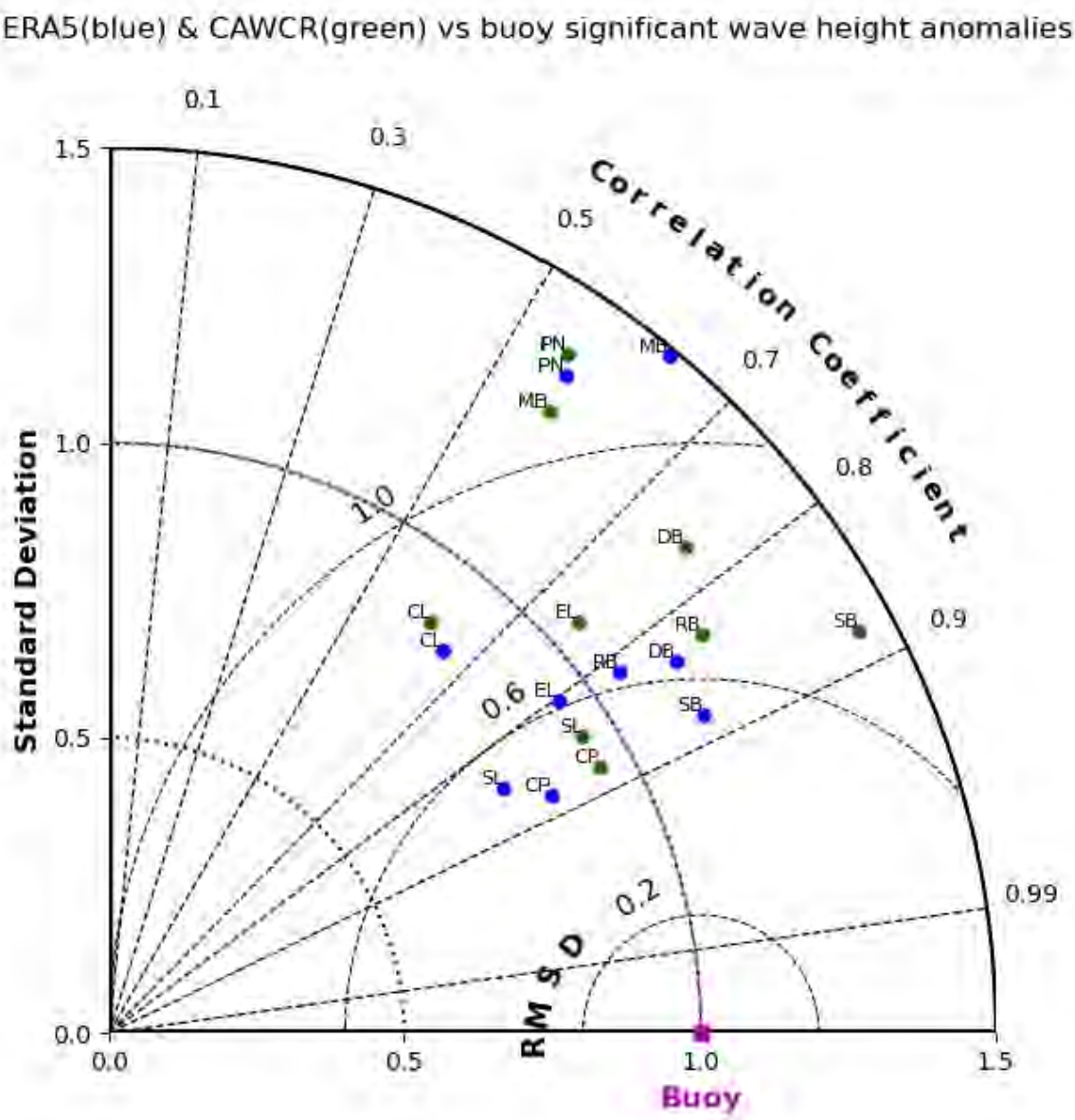

Figure 9: Taylor diagram showing ERA5 (red) vs CAWCR (magenta) Hs anomalies against buoy (blue) Hs anomalies.

Buoy Location:	Correlation coefficient (r)		Normalised standard deviation (sd)		Normalised centred root mean square difference (crmsd)		Best performing: 2r - |sd - 1| - crmsd	
	ERA5	**CAWCR**	**ERA5**	**CAWCR**	**ERA5**	**CAWCR**	**ERA5**	**CAWCR**
Saldanha Bay	**0.92**	0.92	**1.19**	1.50	**0.48**	0.70	**1.17**	0.63
Slangkop	**0.89**	0.88	0.82	**0.99**	**0.47**	0.48	1.12	**1.27**
Cape Point	**0.93**	0.92	0.89	**0.99**	**0.38**	0.38	1.37	**1.46**
Mossel Bay	**0.64**	0.58	1.50	**1.30**	1.15	**1.09**	-0.36	**-0.23**
Port of Ngqura	**0.58**	0.57	**1.38**	1.41	**1.14**	1.18	**-0.36**	-0.45
East London	**0.82**	0.77	**0.97**	1.08	**0.58**	0.71	**1.04**	0.75
Cooper Light	**0.67**	0.63	0.88	**0.90**	**0.77**	0.82	**0.44**	0.33
Durban	**0.85**	0.78	**1.17**	1.30	**0.61**	0.81	**0.93**	0.45
Richards Bay	0.83	**0.84**	**1.07**	1.22	**0.61**	0.66	**0.97**	0.79

Table 2: The statistics used to plot Figure 9. The bold indicates the stronger statistic. The standard deviations and centred root mean square differences have been normalized by the observed standard deviation

3.4.2 Evaluation Against Altimeter Data

The altimeter data does not have a regular frequency due to the varying return periods of the satellites (Figure 4). The climatologies for the concurrent dates are shown in Figure 10. ERA5 assimilates a large amount of this altimeter data so good comparisons are expected (Hersbach *et al.*, 2020). Both products show an accurate seasonal cycle with the CAWCR slightly overestimating and ERA5 slightly underestimating. The persistent positive bias in the buoy vs hindcast climatologies (Figure 5) is expectedly gone at these deep-water locations. The hindcasts adequately represent the annual cycle, so to distinguish between the two the anomalies and spatial bias are considered.

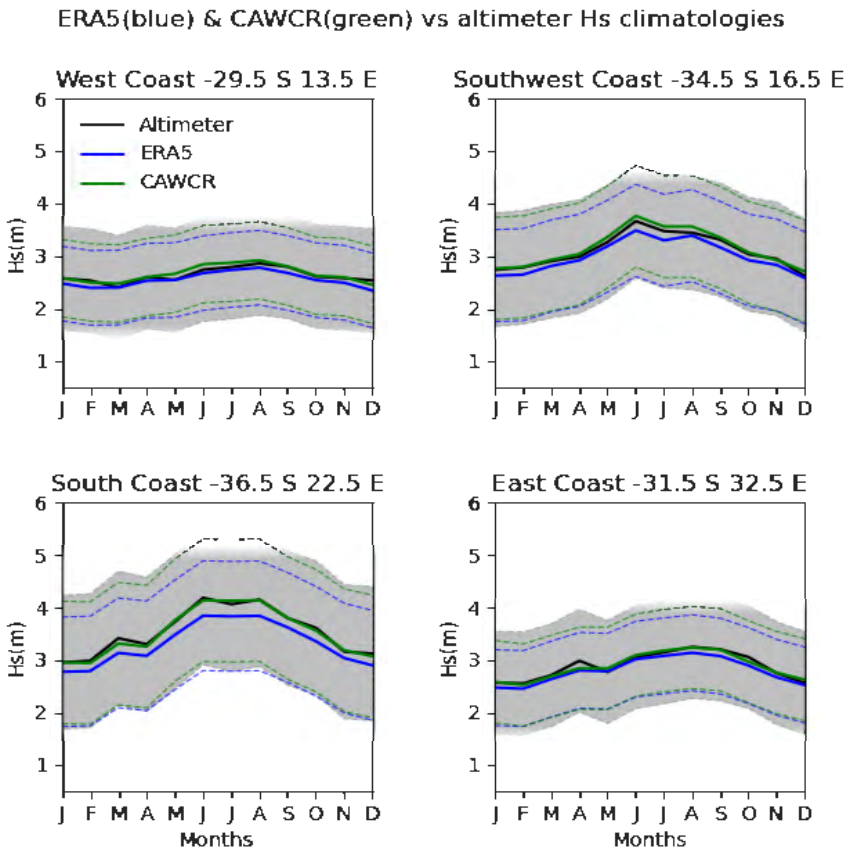

Figure 10: Climatologies of Hs derived from altimeter data compared to hindcast data. The grey envelope represents the altimeter standard deviation. ERA5's standard deviation is represented by the blue dashed line and the CAWCR's by the green.

Performance was first assessed using scatter plots of modelled vs observed anomalies (not shown). For all regions, ERA5 showed a stronger relationship to the observed Hs anomalies (Table 3). The performance was then regionally assessed using Taylor diagrams (Figure 11). The dataset is split into four regions – west, southwest, south, and east (Figure 3). The mean: correlation coefficients, normalized standard deviations, and normalized centred root mean square difference are then used to represent each region on the diagram (Figure 11). All the points are within the normalized standard deviation of the observation. CAWCR has a standard deviation closer to the observed but ERA5 has higher correlation coefficients and lower normalized centred root mean square difference values. The end column of Table 3 shows that ERA5 outperforms the CAWCR for the west, southwest, and east coast offshore regions with both hindcasts performing worse over the east coast region. Finally, the wavefield performance is assessed using the AVISO gridded merged altimeter product. Figure 12 clearly shows the superiority of the ERA5 product. The CAWCR shows a persistent positive bias which is strongest in the south, particularly over summer and autumn. In contrast, ERA5's bias decreases to the south, becoming slightly negative particularly over winter and spring. ERA5 also shows a weak near-coast positive bias which has a year-round presence along the eastern coastline.

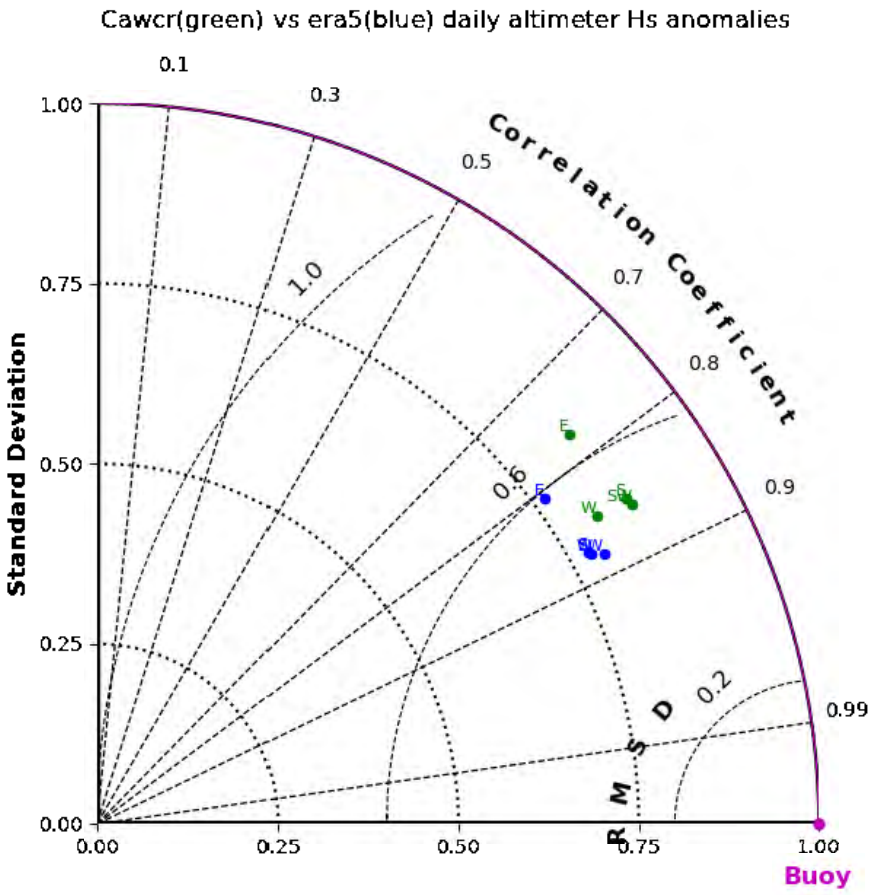

Figure 11: Taylor diagram showing the average regional performance of ERA5 (green) and CAWCR (blue) anomalies against the altimeter anomalies of Hs.

Offshore Region:	**Correlation coefficient (r)**		**Normalized standard deviation (sd)**		**Normalized centred root mean square difference (crmsd)**		**Best Performing: 2r - |sd – 1| - crmsd**	
	ERA5	**CAWCR**	**ERA5**	**CAWCR**	**ERA5**	**CAWCR**	**ERA5**	**CAWCR**
West	**0.88**	0.85	0.78	**0.81**	**0.49**	0.52	**1.05**	0.99
Southwest	**0.88**	0.86	0.80	**0.86**	**0.48**	0.51	**1.08**	1.07
South	**0.87**	0.85	0.78	**0.86**	**0.50**	0.53	1.03	**1.04**
East	**0.81**	0.77	0.77	**0.85**	**0.59**	0.64	**0.80**	0.75

Table 3: The statistics used to plot Figure 11, bold text indicates a stronger statistic.

Overall, the coastal and offshore results agree: ERA5 marginally outperforms the CAWCR hindcast. The outperformance is most clear in Figure 12 wherein the CAWCR gives up to a 0.8m bias. Due to the assimilation of altimeter data into the ERA5 reanalysis product, this comes as no surprise, it does however show the areas in which the CAWCR product does worse. Recent research into the accuracy

of hindcasted wind agrees with this marginal outperforming of ERA5 surface winds vs. other products. Ramon *et al.* (2019) found ERA5 to perform 30% better than an ensemble mean, which included the CAWCR wind forcing (CFSR and CFSv2). On top of this ERA5 is a coupled reanalysis product, with no apparent inconsistencies in the wind forcing or wave model used, unlike the CAWCR product which updated its wind forcing and wave model physics around 2014 (Durrant *et al.*, 2014). These facts make ERA5 superior for the study of both long-term trends and relations to large-scale modes of variability, as has been done for recent assessments of global and regional wave variability (Sreelakshmi and Bhaskaran, 2020; Takbash and Young, 2020; Timmermans *et al.*, 2020).

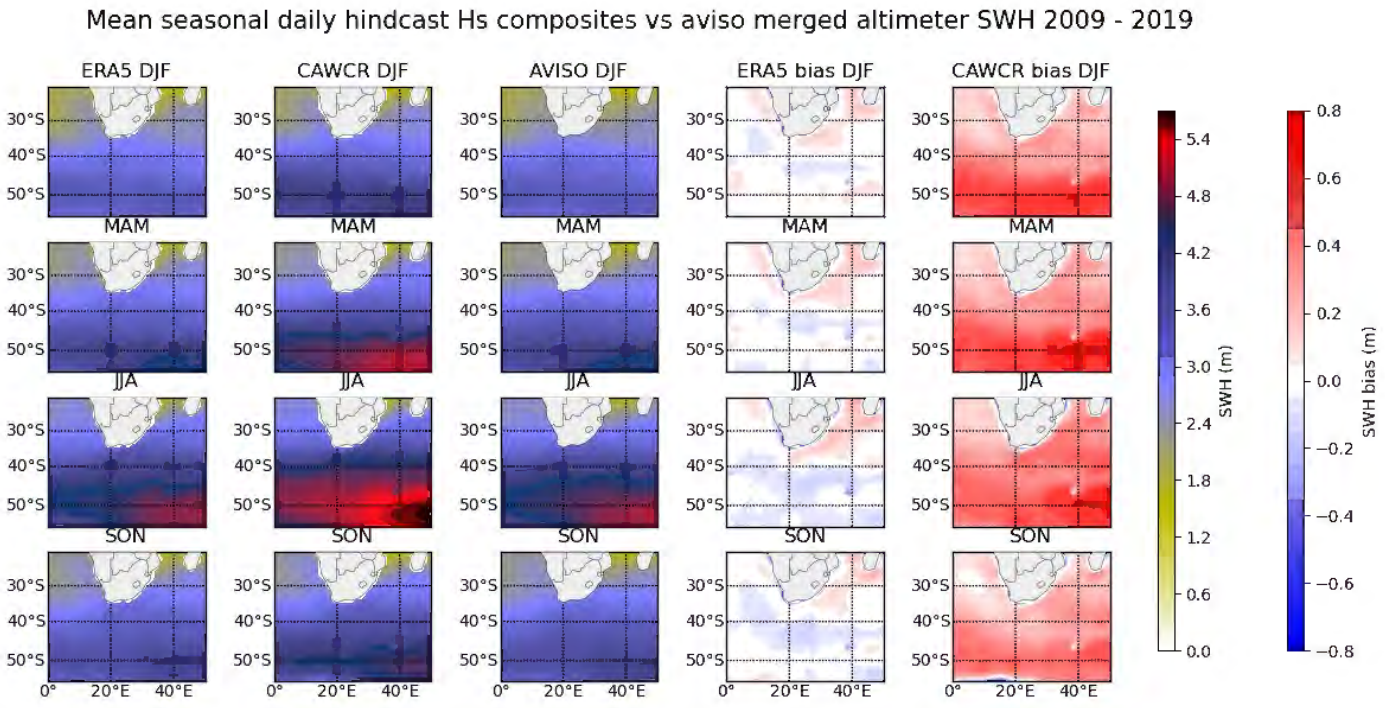

Figure 12: Seasonal composite maps of wave height and their respective bias with the AVISO product. From the left: ERA5, CAWCR, AVISO, ERA5 bias, and CAWCR bias.

4. Results and Discussion

4.1 Seasonal Variability

The mean seasonal fields of 10m wind and wave energy flux are shown to contextualize the changes associated with the various climate modes, and long-term trends. Here it becomes more convenient to show wave energy flux (CgE (kW/m) or flux) which is derived from significant wave height and wave period and travels with the wave direction, therefore allowing for one rather than three plots to provide essentially the same information (equation (2)). All the following plots are done using monthly ERA5 data over the period 1979-01 to 2020-12 based on the austral seasons of summer (DJF), autumn (MAM), winter (JJA), and spring (SON).

The 10m wind shows a persistent westerly band through all seasons which reaches its maximum northward extent in winter. This expansion of the wind belt leads to the expansion of the extratropical cyclone tracks evident in Figure 13. The southerly wind along the west coast follows this meridional migration, starting furthest south in summer. This clear seasonal variation directly translates into the wave energy flux and direction field. Figure 13 shows a winter maximum mean wave energy flux of 50 kWm^{-1} occurring along the southern coastline over the winter months. This seasonality comes from the expansion of the westerlies over the winter months, allowing for larger fetch areas (Figure 13, b)) leading to more input of energy and the turning the mean direction of this flux more west south-westerly and is observed in both the in-situ and altimeter data (Figures 7 and 10). The average annual change is well represented in these plots.

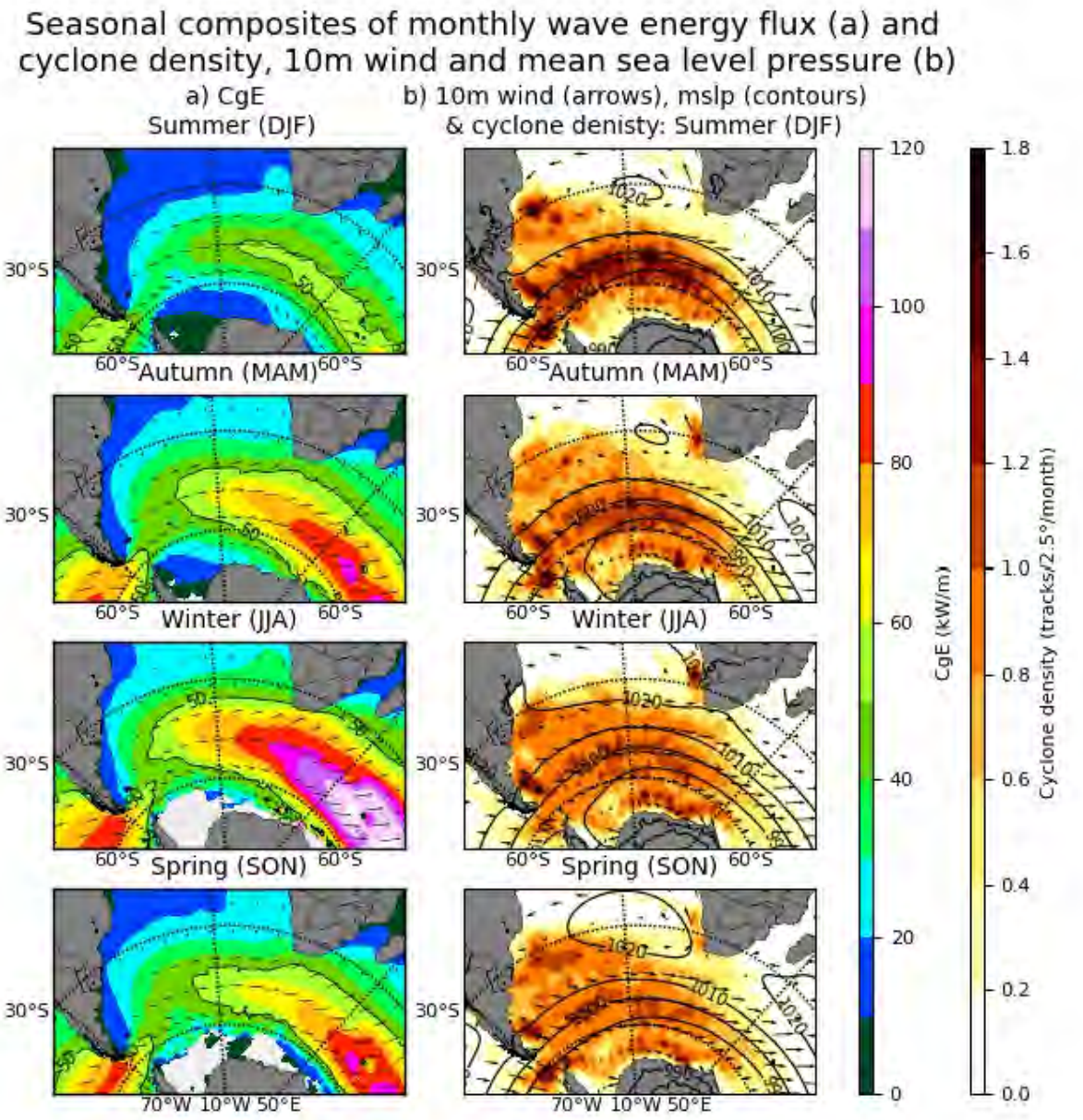

Figure 13: Seasonal composites of monthly wave energy flux (a) and monthly 10m wind, cyclone density and mean sea level pressure (MSLP). The arrows indicate the direction of the flux (a) and wind (b) and the contour lines represent 50 kW/m flux (a) and MSLP levels (b).

The long-term changes in the flux and direction can be better understood by removing this climatology characteristic of the southern African coast, allowing for the identification of anomalously high and low periods as well as the detection of trends. Figure 14 shows the annual trend for each season in both the wave energy flux and direction. Across all seasons the flux is increasing. Over summer the flux is increasing significantly by around 0.3 kWm^{-1} from Namibia round to Mozambique. In autumn the increases are only significant on the southeast African coast, whereas in winter they are only significant along the southwest African coast and over much of the South Atlantic equatorward of 30ºS. Moving into spring the significant patch reaches further east around the coast.

The mean wave direction shows much less significant trends, particularly in the coastal zone. Generally, the wave direction appears to be rotating anticlockwise (decreasing trend), however not enough to be significance at the 95% level. Only in summer and spring are there significant anticlockwise rotations offshore in the mid-South Atlantic, implying the waves are becoming significantly more southerly in these areas. Autumn is the only season during which there are significant coastal changes in wave direction, with clockwise rotations on the east coast near Durban and anticlockwise rotations on the west coast along the Namibian border. Splitting these trends into their respective zonal and meridional components revealed that it is the meridional component that is increasing significantly near the coast across all seasons (see Appendix, Figure A4). On top of the general increase in energy seen in Figure 14, the splitting into meridional components point to a change in the wavefield, where the mean energy flux direction rotates anticlockwise due to a more southerly input of energy into the ocean. These changes in meridional flux are in line with a strengthening polar vortex and southward shift in the subtropical ridge leading to more southerly located storm systems which tend to be more intense (Pezza *et al.*, 2008; Lyttle *et al.*, 2018; Veitch *et al.*, 2019), as well as with research highlighting the global increase in wave power and direction trends around the southern African coastline (Reguero, Losada and Méndez, 2019; Meucci *et al.*, 2020).

Seasonal trends give a good idea of how the wavefield has changed over the entire period 1979-2020, however within these long-term trends there exists variability at both the intra-seasonal and interannual scale. Using the monthly anomaly fields and wavelet analysis this variation can be investigated, giving us a deeper understanding of the driving factors behind this variability.

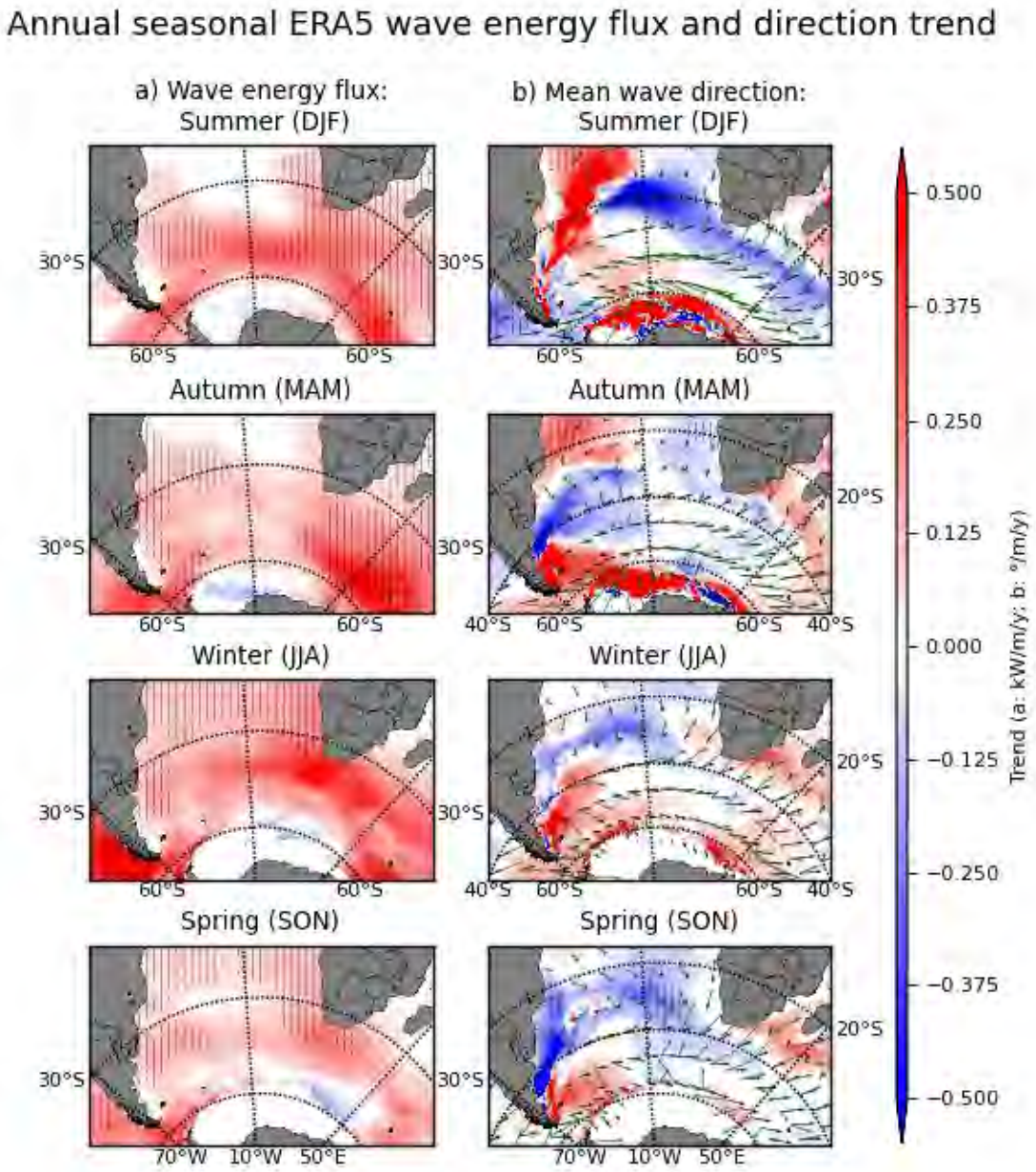

Figure 14: The annual trend in the mean seasonal wave energy flux and direction fields. The shading indicates 95% significance as determined through the pre-whitened Mann-Kendal test over the period 1979 – 2021. The black arrows represent the seasonal mean and the green arrows show the trend.

4.2 Interannual Variability

The interannual variability around the South African coastline is investigated using monthly wave energy flux and mean wave direction anomalies at offshore ERA5 nodes representing each section of the coastline (west, southwest, south, and east, triangles Figure 3). Variations in the wave energy flux and direction anomalies are investigated in Figure 15. The standardized anomalies at each node are shown at a monthly frequency and with an 11-month rolling average filter to highlight the interannual

variations and trends. The series represents the long-term variability of each section of the southern African coastline and the right panel shows the associated wavelet analysis.

Wave energy shows clear periods of above and below normal flux, with a slight increasing trend around the coast (Figure 15) in line with the seasonal trend analysis (Figure 14). Pre-1992 the flux is less variable, with no monthly anomalies exceeding 2.5 standard deviations away from the mean. The 11-month mean is generally below the 1980-2020 climatology. Post-1992 more positive anomalies occur and begin to exceed 2.5 standard deviations away from the mean with the 11-month filtered mean sitting slightly above the long-term climatology. Around 2003, the flux begins to trend negative, and it stays lower than normal until 2006. The anomalies then peak in 2008, more so in the south and east, and again in 2010, more so in the west and southwest. 2005 stands out as the last anomalously low period, after which the variability stays closer to the mean, bar a dip in 2011. Overall, a positive trend in wave energy emerges, in agreement with Figure 14a.

The variation in mean wave direction shows both similarities and differences to the wave energy flux series. Mean wave direction shows more tendency to exceed 2.5 standard deviations in the negative (anti-clockwise rotated) direction. The 11-month filter reveals a slight decreasing trend, contrary to the flux, implying the waves have become more southerly (anti-clockwise rotated) with time. This shift is in line with research showing a southerly shift in the high-pressure belt and an intensification of the Antarctic polar vortex associated with global warming (Burls *et al.*, 2019; Fahad *et al.*, 2020) and the mean wave direction and meridional wave energy flux trend plots (Figures 14b and A4).

Generally positive direction anomalies (clockwise rotated) coincide with positive wave energy flux anomalies and vice versa, however, the magnitude of the anomaly is not always consistent. Correlations between standardized flux and direction anomalies show a significant positive relation does exist and is strongest at the eastern and southern nodes, $r \sim= 0.4$ (Table 4). This result follows since an expanded fetch area (westerly wind belt) is associated with above-average energy input as well as anomalously north extratropical cyclone tracks and therefore a more westerly wave direction. Although these correlations hold, there are numerous examples of both coupled and uncoupled anomalies. The 1992 positive anomalies are a good example of a synchronized spike, whereas the positive 1987 direction anomalies are absent in the flux series. In the winter of 2011, we see the largest negative direction anomalies in the series, this period also had weak negative to neutral flux anomalies. 2005 stands out as the largest negative flux anomaly, however, it does not reflect in the direction series. These differences could be explained by changes in not only storm track location but also intensity. For instance, a more intense period with tracks in their mean climatological position would lead to above-average flux but not direction as the waves would be generated at the same incident angle. Similarly, an expanded storm belt could consist of less intense systems, leading to only positive direction anomalies.

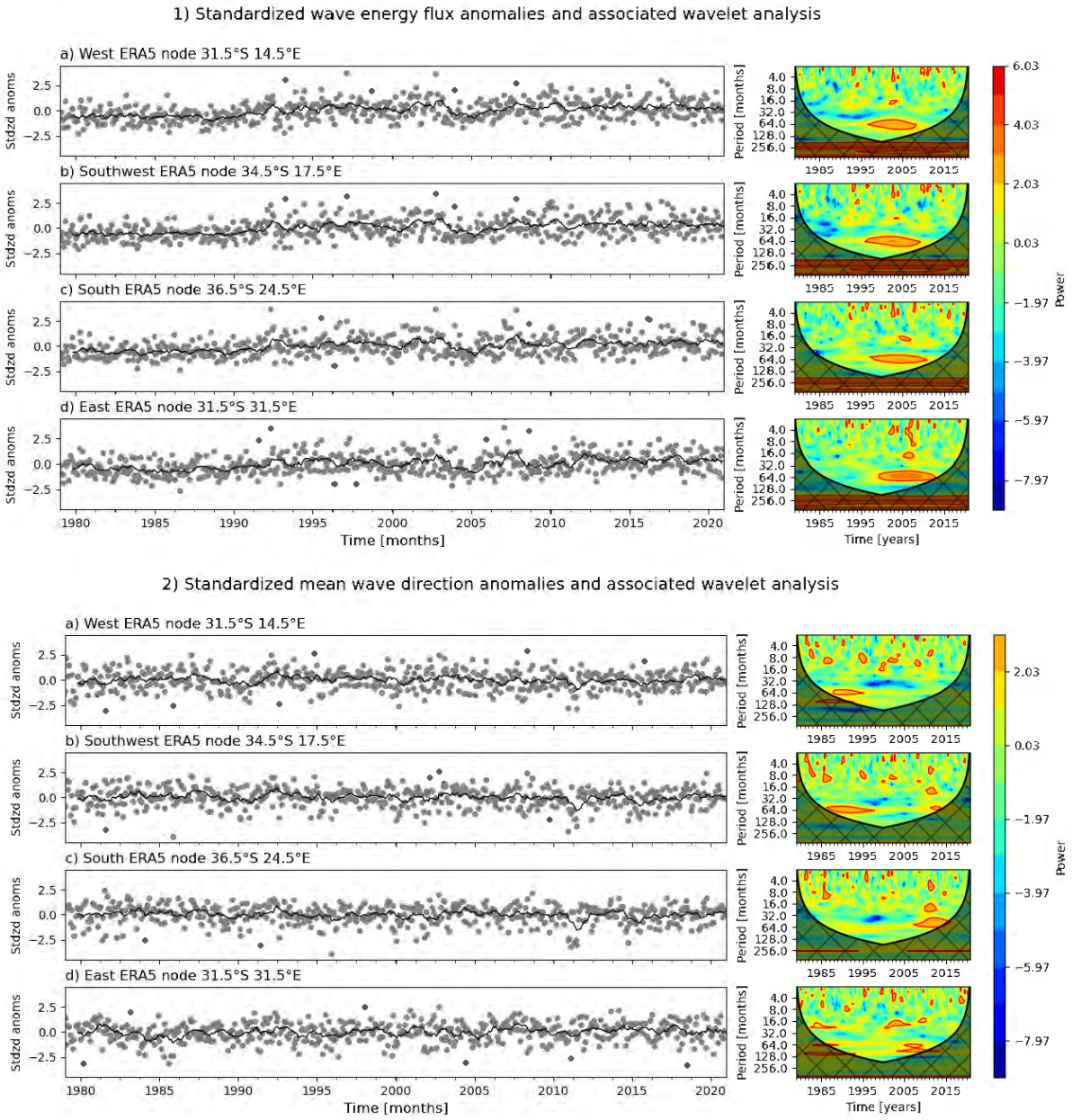

Figure 15: Standardized wave energy flux (1) and mean wave direction (2) anomalies and their associated wavelets for offshore nodes located along the west (a), southwest (b) , south (c), and east (d) sections of the South African coastline (see diamonds Figure 3) over the period 1979 – 2020.

Looking at the flux wavelets (right panel, Figure 15), a significant ($p < 0.05$) 5-year cycle emerges. The southwest is the first region to experience this variation in 1996, it then moves along the coastline, reaching the west and south in 1997 and finally appearing in the east in 1999. It persists longest in the south and east, ending in 2012 and 2013 respectively. This period represents the most variable 15 years that occurs between 1979 and 2020 around the southern African coastline, after which the variation tends to relax towards a higher mean state (Figure 15 panel 1). The direction wavelets are much less uniform, with no progressive 5-year cycle emerging as for the flux. The west and southwest wavelets are similar with a significant 5-year cycle between 86 and 96. The southern

node experiences significant cycles towards the end of the series with a 5-year cycle between 2007 and 2014 and an approximate 3-year cycle within that, between 2010 and 2012. These cycles are linked to the negative anomalies present in 2011 and 2015. This variation is present but damped in the southwestern node's series and wavelet. The eastern node differs from the other three, showing some significance in 2ish-year cycles centred around 1985 and 2004, and 10- and 5-year cycles starting around 2005 (Figure 15 panel 2).

The higher correlation between direction and flux at the east and south nodes could be due to this co-occurrence of significant 5-year cycles in both series. In fact, during these cycles the relationship strengthens. Table 4 shows the flux-direction correlations during which a significant 5-year cycle was present in the flux wavelet (Figure 15). All nodes experienced an increase in the strength of the direct relationship compared to the whole period implying that direction and flux are more synchronized in the latter period. Therefore, the driver of these cycles must be affecting both the intensity and position of the systems.

Period	West R	Southwest R	South R	East R
1979 – 2020	**0.18**	**0.28**	**0.4**	**0.43**
1997 – 2012	**0.31**	**0.41**	**0.45**	**0.47**

Table 4: Correlation coefficients from a Pearson correlation between detrended wave energy flux and mean wave direction standardized anomalies for the entire period and the subset 5-year cycle period. Bold indicates significance > 95%.

4.3 The Role of Large-Scale Modes of Variability

The long-term variations in the extratropical cyclone tracks, intensities, and their surface winds ultimately control the long-term variations in the wave energy flux and direction around the South African coastline (Shillington, 1974; Birkett, 2010). Anomalies in monthly wave energy flux and wave direction are used to select months for when both, only direction, or only flux are further than 1.5 standard deviations away from the mean in the positive and negative manner. Each group of months is then used to subset anomalies of cyclone track density, 10m wind, and MSLP. These subsets are then averaged to create composites characteristic of each combination, for example, positive flux and neutral direction, or negative flux and negative direction, etc. (Figure 16). Positive wave energy flux and direction anomalies are associated with cyclonic 10m wind anomalies, negative MSLP, and positive cyclone density anomalies along 40ºS to the southwest of South Africa (Figures 16a-c). During positive direction anomalies, the entire system is shifted northward with a near-coast WNW wind anomaly, whereas when there are only flux anomalies, a near-coast WSW wind with a weaker MSLP anomaly and slightly above normal cyclone density just south of 40ºS are present. The negative anomaly composites (Figures 16d-f) show generally the opposite, with positive MSLP, anticyclonic 10m wind, and below-average cyclone density anomalies around 40ºS. The negative direction

anomaly plots are again associated with a southward shift of the high-pressure centre and a strong near-coast ENE wind anomaly (Figure 16 e). When both are negative, the cyclone track density anomalies are negative between 40ºS – 50ºS and positive on either side of this high-pressure anomaly around 30ºS and 60ºS. These composites show how large positive anomalies in both flux and direction are associated with shifts in atmospheric mass, which in turn change the position and strength of extra-tropical cyclones and near-surface winds but what is driving these shifts of mass?

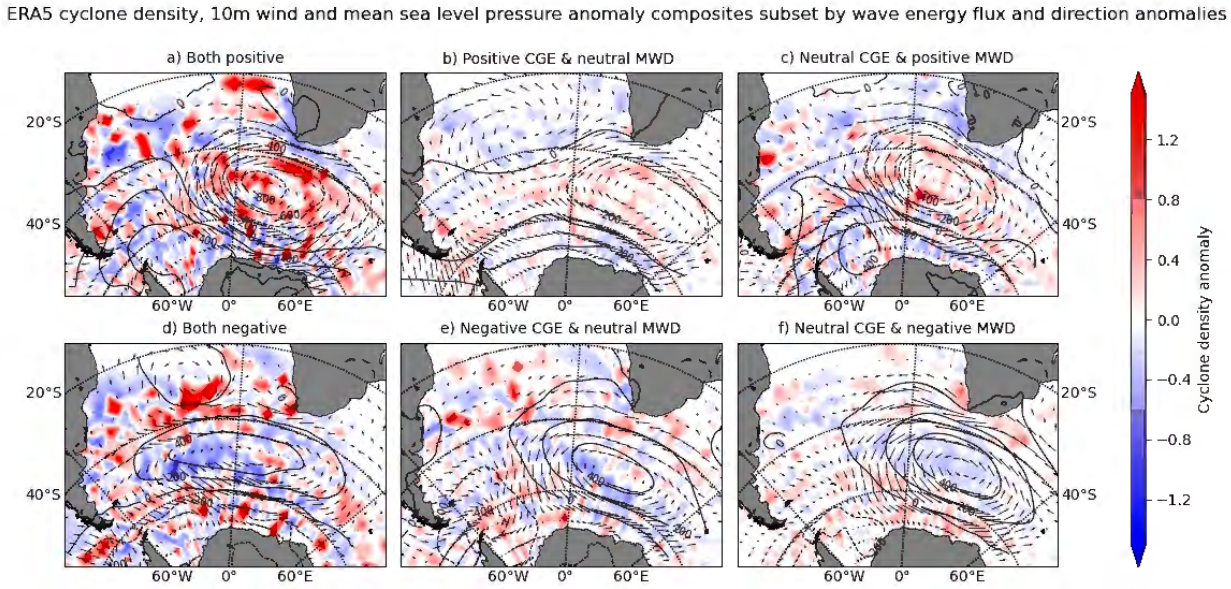

Figure 16: 10m wind (vectors), cyclone track density (colour shading) and mean sea level pressure (MSLP) (solid (positive) and dashed (negative) lines) anomaly composites for different combinations of positive/negative (> 1.5sd, <1.5sd) wave energy flux and direction anomalies at the south node.

The drivers behind these shifts have been investigated with regards to South African rainfall, winds, and waves (Rouault *et al.*, 2010; Burls, *et al.*, 2019; Veitch *et al.*, 2019). This research highlighted the SAM as important for winter rainfall over western South Africa via its influence on moisture fluxes and regional subsidence (Reason and Rouault, 2005). However, SAM is not the only mode impacting the circulation around the South African coastline. Rouault *et al.* (2010) found significant relationships between near-surface winds and the El Niño Southern Oscillation (ENSO), particularly over summer months with the strength of the South Atlantic Anticyclone system and its winds to be above-average during La Niña events. However, there is considerable variation in the regional circulation and rainfall anomalies over southern Africa during different ENSO events (Reason and Jagadheesha, 2005; Blamey *et al.*, 2018).

Veitch *et al.* (2019) recognized that combinations of these ENSO and SAM can lead to an anomalous summer season regarding wave power and direction in the Cape Point wave record. Similarly, Marshall *et al.* (2018) and Godoi and Torres Júnior (2020) considered such combinations on a global scale, investigating how phase combinations of various modes led to significant changes in sensitive

areas. For example, in the southeast Atlantic, there were positive anomalies in wave power under negative SAM, which intensified and had a greater coastal impact on South Africa when combined with El Niño over summer (Godoi and Torres Júnior, 2020). In addition to the SAM and ENSO, the semi-annual oscillation (SAO) has been found to significantly impact cut-off low frequency and winter rainfall (Singleton and Reason, 2007). Cut-off lows are generally responsible for large wave energy events along the south-eastern coastline (van der Borch van Verwolde, 2004; Corbella and Strech, 2012a, 2012b; Jury, 2019). Given these relations, the long-term wave variations are compared to the SAM, ENSO, and SAO time series to obtain a first glance at their potential impacts.

Figure 17 shows the flux and direction variations with a 5-month rolling filter for the west, south, and east nodes (triangles in Figure 3), as well as the 3-year rolling, mean highlighting the long-term trends. The figure also shows the SAM, ENSO, and SAO time series with a 5-month rolling mean and the positive and negative months highlighted. In this figure, the above relations previously found for SAM and ENSO begin to emerge. At the time of the 1992/1993 spike present in both flux and direction, weak El Niño, negative SAM and negative SAO conditions existed consistent with earlier work (Birkett, 2010; Marshall *et al.*, 2018; Veitch *et al.*, 2019; Godoi and Torres Júnior, 2020). Similarly, the negative anomalies in 2011 occurred during a La Niña, positive SAM, and positive SAO phase. However, care must be taken to properly understand the significance of the impact of each mode before concluding on their apparent influence over the variability present in Figure 17.

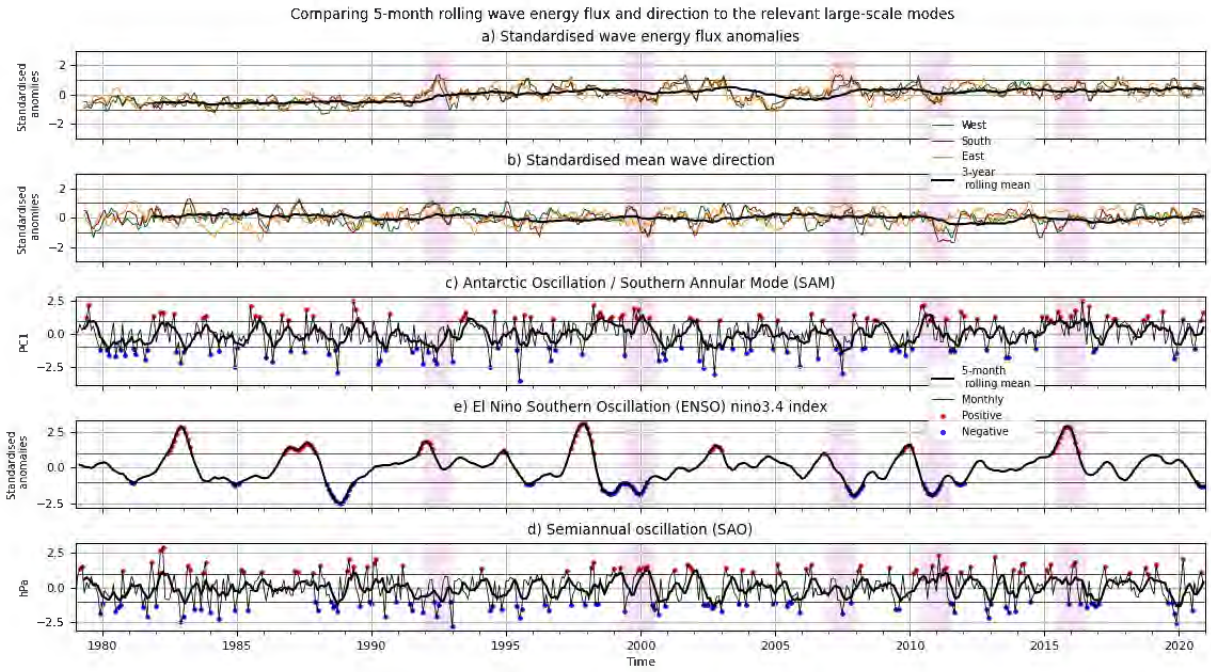

Figure 17: Time series of the 5 month-rolling mean standardized wave energy flux and direction anomalies compared to the ERA5 derived SAM, ENSO, and SAO indices over the period 1979 – 2020. The solid black line in plots c), d) and e) represents the 5-month rolling mean.

Figure 15 indicated a clear signal at about five years during which a strong direct association between flux and direction anomalies is present (Table 4). Given the relationships already found with SAM and ENSO, a similar correlation analysis was performed in which the correlations over the whole period were compared to the correlations during the significant 5-year cycle present in the wavelets of Figure 13. Table 5 shows how the correlations changed during the period 1997 – 2012 when compared to the correlations over the whole period. Both the SAM and the SAO inverse relationships with ENSO became significant while those computed for the whole period were not. The stronger association between SAM and ENSO since the 1990s has been noted in other research and is linked to the change of ENSO, toward more frequent mid-basin/Modoki events (Lim, Hendon and Rashid, 2013; Yu *et al.*, 2015). The out of phase nature of ENSO and SAM during this 5-year cycle could be behind this more variable period in the wave record. The following sections use validated ERA5 derived climate indices to assess the long-term variability in the wave energy flux and direction anomalies using detrended seasonal correlations and composites.

	Correlation Coefficient		
Period:	**SAM with ENSO**	**SAM with SAO**	**ENSO with SAO**
1979 – 2020	-0.062	**0.61**	-0.11
1997 – 2012	**-0.23**	**0.59**	**-0.27**

Table 5: Correlations between the modes in question over the whole period and during the 5-year cycle subset. Bold indicates significance at the 95% level

4.3.1 Antarctic Oscillation/Southern Annular Mode (SAM)

First, the effect of SAM on the wind at 10m is investigated. The drag between these surface winds and the underlying ocean is the primary source of ocean wave energy flux, therefore understanding the relations between SAM and the speed and direction of the wind will aid in understanding the wave energy flux response. The detrended seasonal correlations between monthly wind speed (a) and direction (b) are shown in Figure 18. Generally, there are inverse relations between wind speed and SAM across all seasons which are strongest, largest in area, and located furthest south over summer. This patch moves equatorward and shrinks in winter, with near-coast significant negative correlations over both autumn and winter. Above these negative correlations, there are positive correlations near the coastline during both summer and spring, stretching furthest into the South Atlantic in summer, and into the Southwest Indian in spring. Wind direction is also inversely correlated with SAM around the southern African coastline (Figure 18 b). These negative correlations are strongest over summer and weakest over winter where they are only significant on the western and eastern coastlines. The direction responds directly offshore of the coastline year-round.

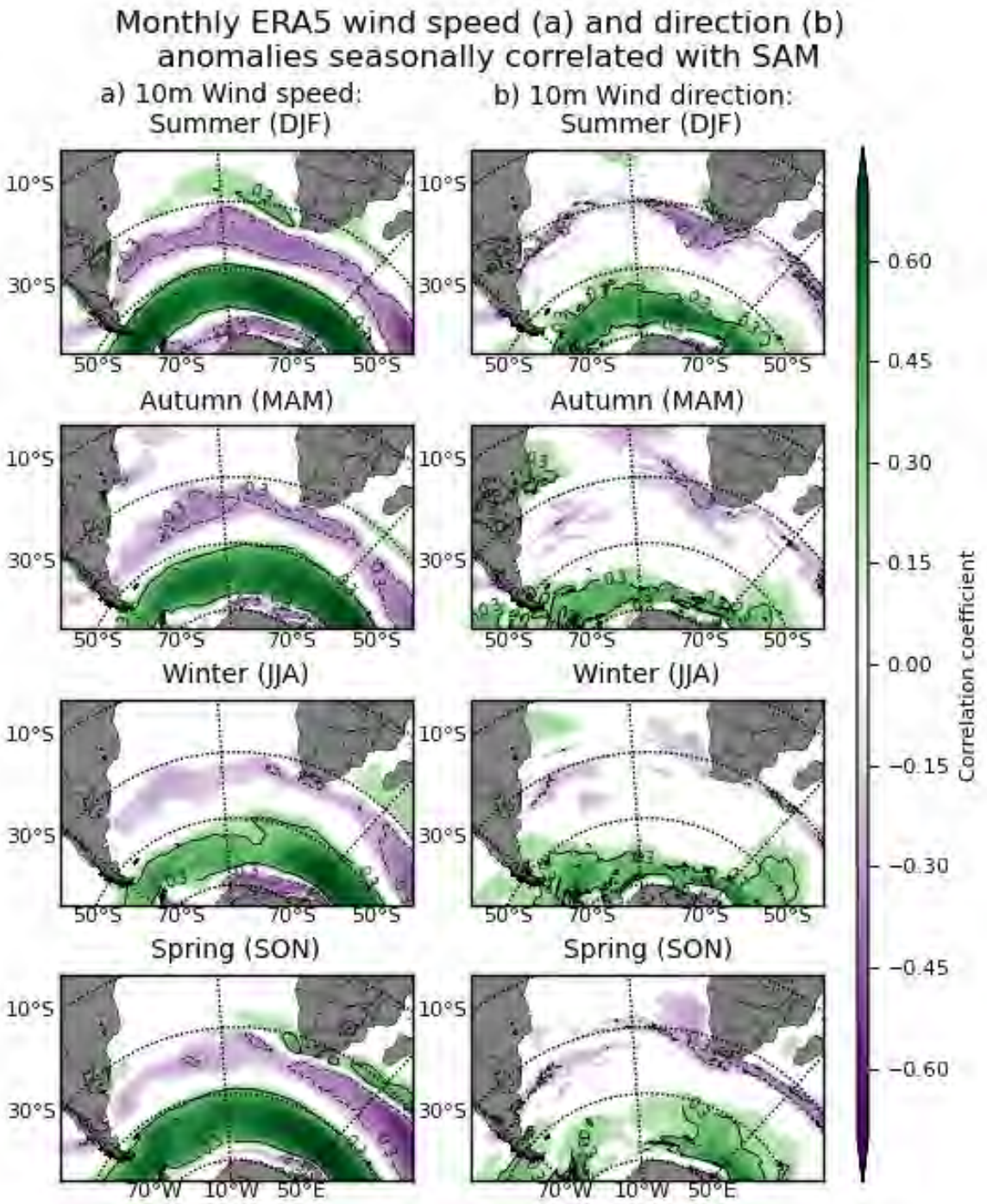

Figure 18: 10m wind speed (a) and direction (b) anomalies seasonally correlated with SAM. Only correlations significant at 95% and greater are shown. The darker the colour the stronger the correlation. The solid (dashed) contour line indicates correlations of 0.3 (– 0.3).

From these correlations the responses to positive and negative SAM months are determined. During the positive phase of SAM, the mean wind speed decreases between 35ºS and 50ºS and increases near the coastline. These near-coast increases are strongest over spring and summer, during which a positive SAM also rotates the mean wind direction anticlockwise implying above-average south-easterly winds. The response is reversed for negative SAM where the winds are stronger between

35ºS and 50ºS and the wind direction is rotated clockwise between 40ºS and the southern African coastline (Figure 18). South of 50ºS there is a strong direct relationship between SAM and wind speed ($r \sim 0.7$, $p < 0.05$) higher (lower) wind speeds under positive (negative) phases of SAM. Over roughly the same area the winds are rotated clockwise, becoming more north-westerly than the seasonal mean. From these responses, we expect inverse relations between the magnitude and direction of the wave energy reaching the southern African coastline and a direct one around the Antarctic peninsula.

The response of the wave energy flux and direction are similarly assessed using detrended seasonal correlations. Year-round the flux is negatively correlated to SAM north of 50ºS (Figure 19 a). The response is largest in areal extent over spring stretching from the Angolan coastline round to the southern Mozambiquan and Madagascan coastlines. Winter gives the strongest relations on the west coast of South Africa ($r = -0.4$, $p < 0.05$) with this patch moving eastwards to the south coast in spring. Summer sees a weaker but significant near-coast response that is not as spatially extensive as the other months. The direction of this flux is also significantly affected by SAM in all seasons. The strongest and most extensive response is in summer where the flux rotates anticlockwise between 60 ºS and the southern African coastline. Over winter only the direction of the flux along the eastern and Madagascan coastline responds significantly.

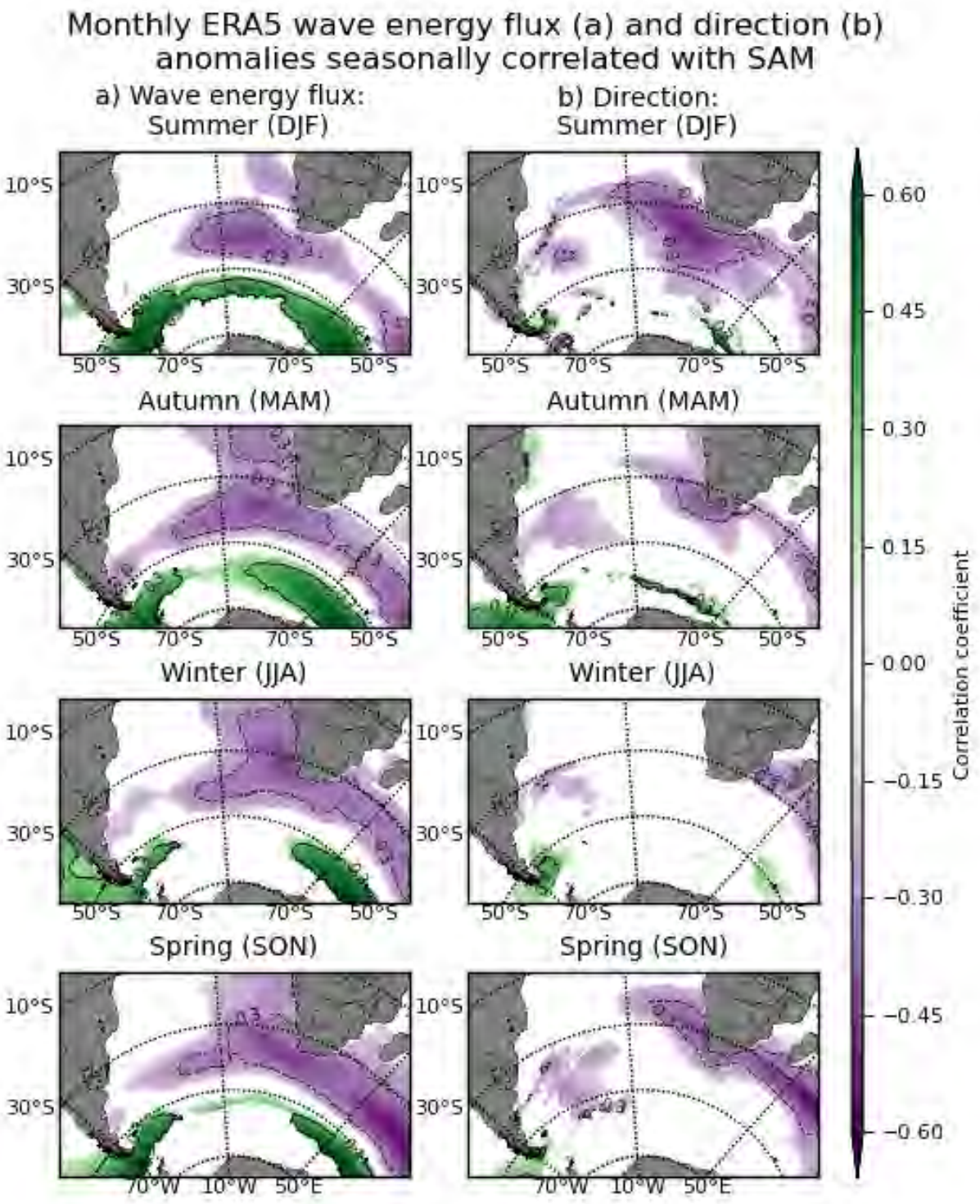

Figure 19: Monthly wave energy flux (CgE (kW/m)) (a) and direction (b) seasonally correlated with SAM. Only areas significant at the 95% level are shown. The solid (dashed) contour line indicates correlations of 0.3 (– 0.3).

These correlations show how SAM can significantly change the wave energy flux at a seasonal scale. The positive SAM phases drive below-average wave energy flux year-round, with this flux rotated anticlockwise from its seasonal mean state implying generally more southerly waves for all seasons

except winter where the response area is much smaller. The negative SAM has approximately the opposite effect, with above-average flux year-round. This flux is also more westerly (clockwise rotated) over the significant areas (Figure 19).

Next the seasonal wave energy flux anomaly composites, for positive and negative SAM phases, are investigated (Figure 20). They reveal that significant near-coast anomalies only occur under the positive phase in winter and under the negative phase in spring. In winter negative flux anomalies up to 8 kW/m below the mean occur under the positive phase, whereas in spring positive flux anomalies up to 4 kW/m above the mean are present (negative phase). Summer shows a stronger offshore response to negative SAM than to positive although both have significant regions. Also of note is the autumn response to negative SAM which has significant positive anomalies just off the south coast of South Africa. Although they are generally in agreement, the composites show a more varied response compared to the correlations mainly through the significant areas and the varied response to positive and negative phases of the SAM (Figures 19 and 20). These results agree with previous studies at both the global and regional scale (Birkett, 2010; Marshall *et al.*, 2018; Veitch *et al.*, 2019; Godoi and Torres Júnior, 2020) who found a significant response between the wavefields and SAM.

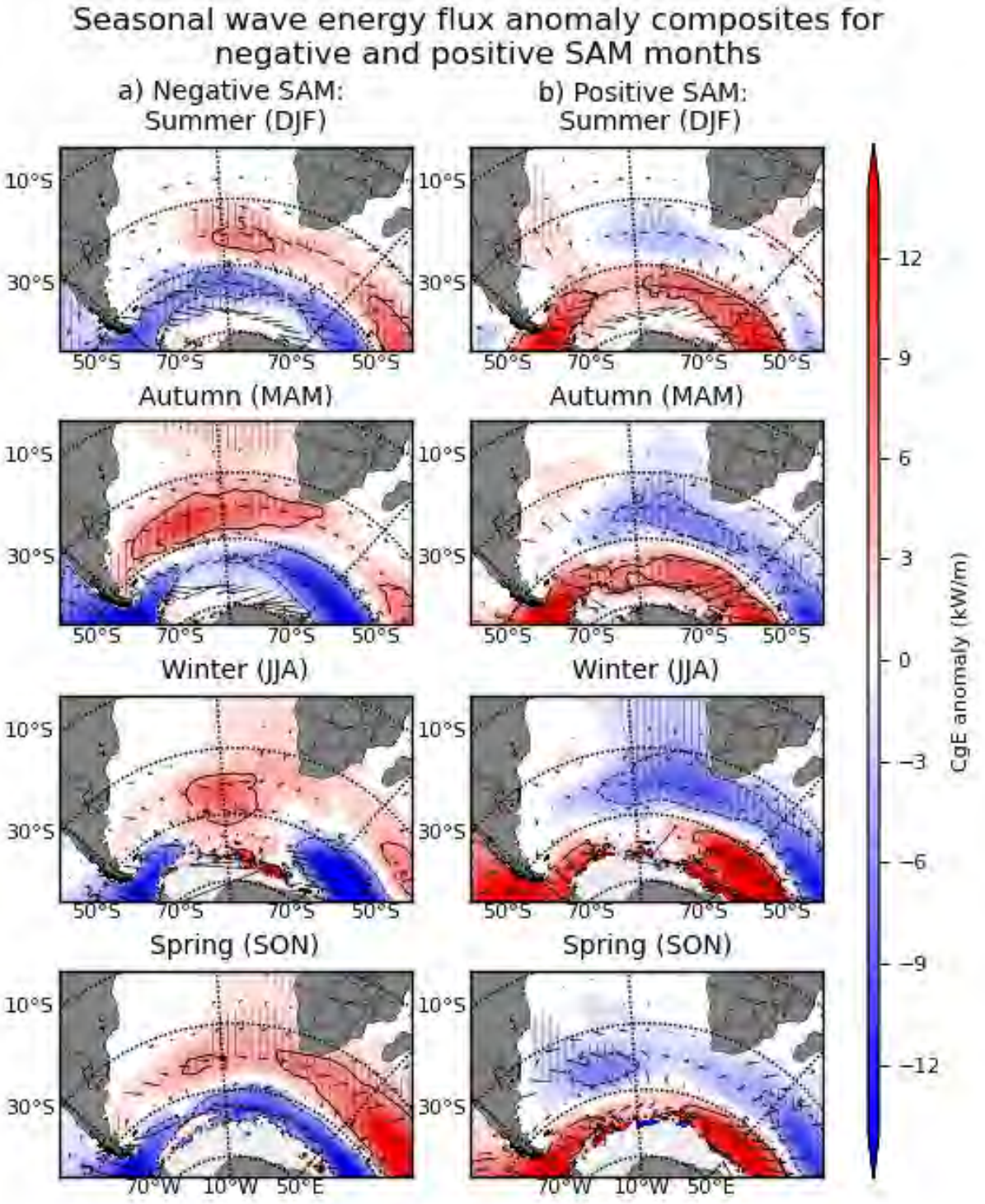

Figure 20: Wave energy flux and direction anomalies under negative (left) and positive (right) SAM by season. The shading indicates 95% significance in the wave energy flux anomalies. The solid (dashed) contour line indicates anomalies 5 kW/m (– 5 kW/m) above (below) the seasonal mean. The no. of months used for each composite are given in Table A1.

The relationships to the in-situ data are investigated to see if these relations are present in the coastal zone. Table 6 shows the seasonal correlations of significant wave height anomalies with the ERA5

derived SAM index. There are year-round significant negative correlations present at both the Saldanha Bay and Cape Point stations. At Saldanha, the relation is strongest over summer whereas at Cape Point it is strongest over spring. Slangkop shows the strongest inverse relation over spring with r = -0.56, but no significant relations over the autumn and winter months. These strong spring relations agree with those in Figure 20, where the strongest coastal response to negative SAM is over spring. Other significant inverse coastal relations are present at East London between autumn and spring, and Richards Bay over winter. The only direct relation occurs at the Port of Ngqura over autumn with an r = 0.47, implying increased wave heights during positive SAM which is likely a function of the increased easterly autumn flux negating the headland shadowing the buoy from the dominant south-westerly waves. These relations show slight differences to the ERA5 correlations due to shorter, inconsistent recording periods (Table 1), the proximity to nearshore bathymetry and headlands, and because these correlations are just to significant wave height. Generally, the relationships found between SAM and the wave flux fields agree with these Hs correlations as well as previous research(Veitch *et al.*, 2019; Godoi and Torres Júnior, 2020). These previous studies also highlighted the impact of the El Niño Southern Oscillation on the South Atlantic wavefield.

Buoy location:	Summer R	Autumn R	Winter R	Spring R
Saldanha Bay	**-0.41**	**-0.33**	**-0.40**	**-0.36**
Slangkop	**-0.38**	-0.13	-0.27	**-0.56**
Cape Point	**-0.37**	**-0.35**	**-0.39**	**-0.40**
Mossel Bay	-0.18	0.16	-0.04	-0.1
Port of Ngqura	0.08	**0.47**	-0.12	-0.01
East London	-0.18	**-0.24**	**-0.22**	**-0.31**
Cooper Light	0.18	-0.20	0.15	0.20
Durban	0.25	0.08	-0.18	0.24
Richards Bay	0.07	-0.001	**-0.29**	-0.03

Table 6: Seasonal correlations between ERA5 derived SAM index and in-situ significant wave height data recorded along the South African coastline at a monthly frequency. Bold indicates significance >= 95%.

4.3.2 El Niño Southern Oscillation (ENSO)

Previous research has found significant relations between the summer South Atlantic winds through modifications of the subtropical jet stream, which becomes stronger and moves poleward during El Niño events. Focussing on the changes to the wavefield, Veitch *et al.,* (2019) and Godoi and Torres Júnior (2020) showed how these changes impart changes in the amount of energy input into the wavefield and in some cases led to above-average flux and westerly direction anomalies over the

austral summer months. Given these results we expect summer to show the strongest relations in both 10m wind and wave energy flux.

The 10m wind speed and direction fields show significant responses to the Niño3.4 index overall seasons except winter. Summer shows the strongest near-coast relations to both wind speed and direction (Figure 21). The wind speed directly off the southern coastline is negatively correlated with this band stretching out along 35ºS into both ocean basins. Below this band, there is a significant positive correlation over much of the fetch area stretching from the mid-South Atlantic into the southwest Indian. During summer near-coast wind direction is also strongly associated with ENSO with positive correlations between the south coast and 40ºS. These relationships imply that La Niña (El Niño) events drive stronger (weaker) near-coast winds which are anticlockwise (clockwise) rotated, with the winds around 45ºS becoming weaker (stronger). Autumn and spring also show some interesting correlations. The wind speed is directly associated with ENSO over autumn stretching from the southwest Atlantic toward the African continent. This could lead to above-average energy input over this fetch area, potentially generating more long-period swells over the autumn months. Spring shows similar relationships to summer but shifted further offshore and no direct relation to wind speed over the fetch areas. Wind direction does seem to be significantly related to ENSO east of the mid-South Atlantic, implying clockwise rotated or westerly to north-westerly wind direction anomalies during El Niño events. Given these significant correlations, we expect a significant response in the wave energy flux and direction fields, particularly over summer.

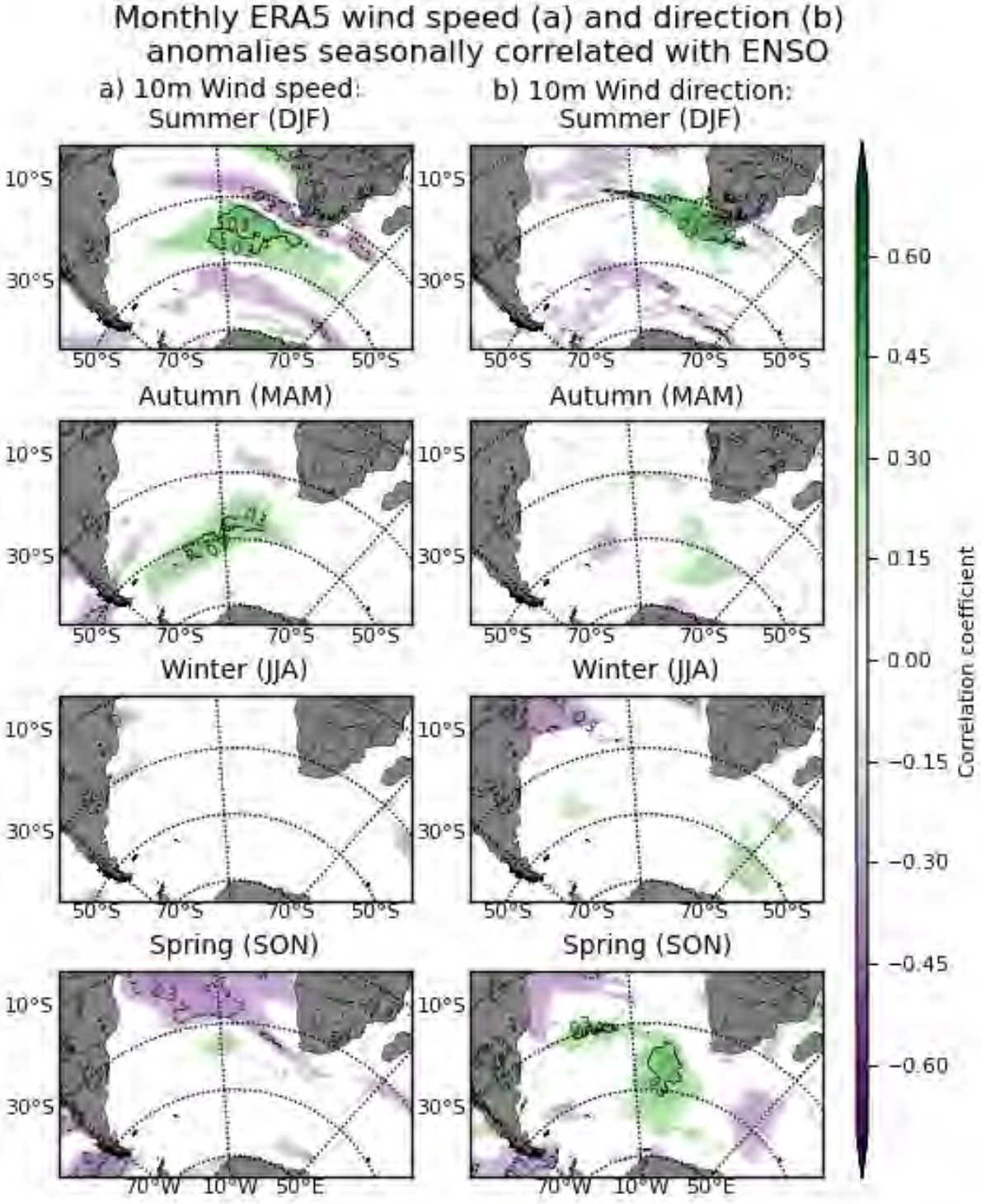

Figure 21: Same as Figure 19 but for detrended correlations with the ERA5 derived Niño3.4 index. Only correlations significant at 95% are shown. The solid (dashed) contour line indicates correlations of 0.3 (– 0.3). A positive (negative) correlation means the wind speed increases (decreases) and rotates clockwise (anti-clockwise) when the index is positive

The detrended spatial correlations between wave energy flux and direction and the Niño3.4 index again show significant responses for all seasons except winter (Figure 22). Summer is the only season

with significant coastal correlations for both flux and direction, although the flux response is stronger offshore in the southeast Atlantic. Both the direction and flux respond directly, with the strongest direction correlation on the west and southwest South African coastline. The flux arriving at the Namibian and Angolan coastlines is also significantly modified by ENSO. During summer La Niña (El Niño) events rotate the direction anticlockwise (clockwise) giving southerly to south-easterly (westerly to south-westerly) anomalies along the southern African coast this flux is also below (above) average along the southwest African coast and in the southeast Atlantic (Figure 22). Autumn is the only other season during which there is a significant coastal relation along the South African coast. The autumn wind speed relations over the southwest Atlantic translate to above-average flux along the coastline, with this flux being above (below) average during El Niño (La Niña) events. Spring has large patches of significant correlations to ENSO, but they are generally centred in the mid-South Atlantic. The direction equatorward of 30ºS is positively correlated with ENSO nearly across the basin significantly affecting the waves along the northern Namibian and Angolan coastline. However, do these regions respond uniformly to both La Niña and El Niño events, or is the response more sensitive to one or the other?

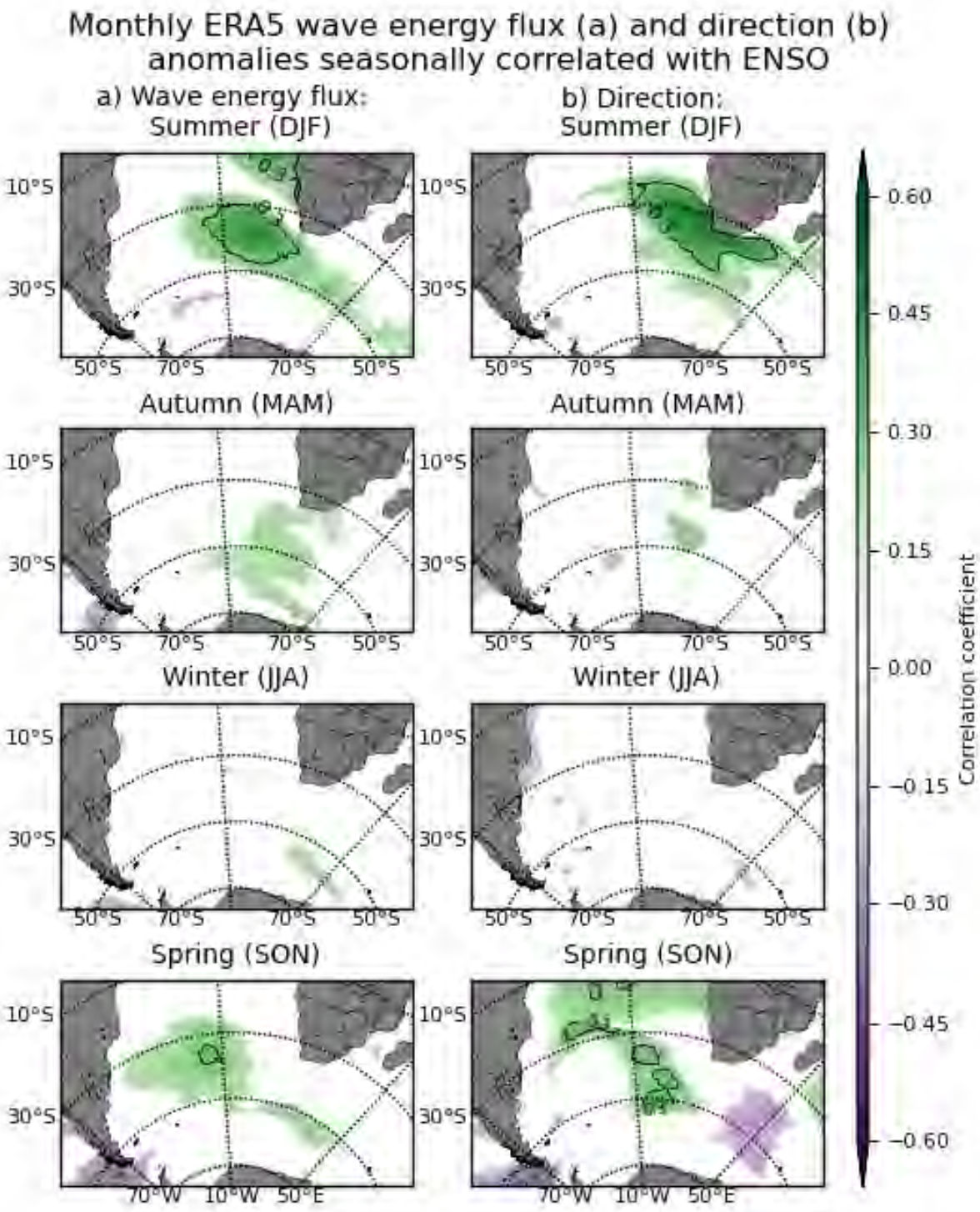

Figure 22: Same as Figure 20 but for detrended correlations with the ERA5 derived Niño3.4 index. Only correlations significant at 95% are shown. The solid (dashed) contour line indicates correlations of 0.3 (– 0.3).

Figure 23 gives a clearer picture of the seasonal wave energy flux response to the individual phases of ENSO using composites. During spring and summer, El Niño leads to significant positive flux anomalies in an NW to SE band across the South Atlantic into the South Indian Ocean. This band of

increased flux agrees with the view that El Niño tends to cause stronger and more unified storm tracks through the merging of the subtropical and subpolar jet streams (Pezza *et al.*, 2008). The direction tends to be more westerly over these months, although near the coast no significance is found in the flux anomalies. Near-coast significance is only associated with La Niña events. Autumn shows the largest extent of significance along the South African coastline (Figure 23). During summer, the impact leads to negative flux and easterly direction anomalies reaching from the Angolan/Namibian border down to the southwestern coastline of South Africa in agreement with the summer correlations. Winter shows significant negative anomalies along the east coast of South Africa. These negative winter anomalies under La Niña are not in line with the winter correlations (Figures 22 vs 23). Interestingly both El Niño and La Niña events lead to below average winter flux. Work by (Lim *et al.*, 2013) showed how Modoki ENSO events have a significant ability to excite the opposing SAM phase in the austral cold seasons. Given the strong relations that SAM had to the winter wavefields (Figures 19 and 20) it could be that during winter La Niña events the positive SAM is excited and the wavefield responds as seen in Figure 23.

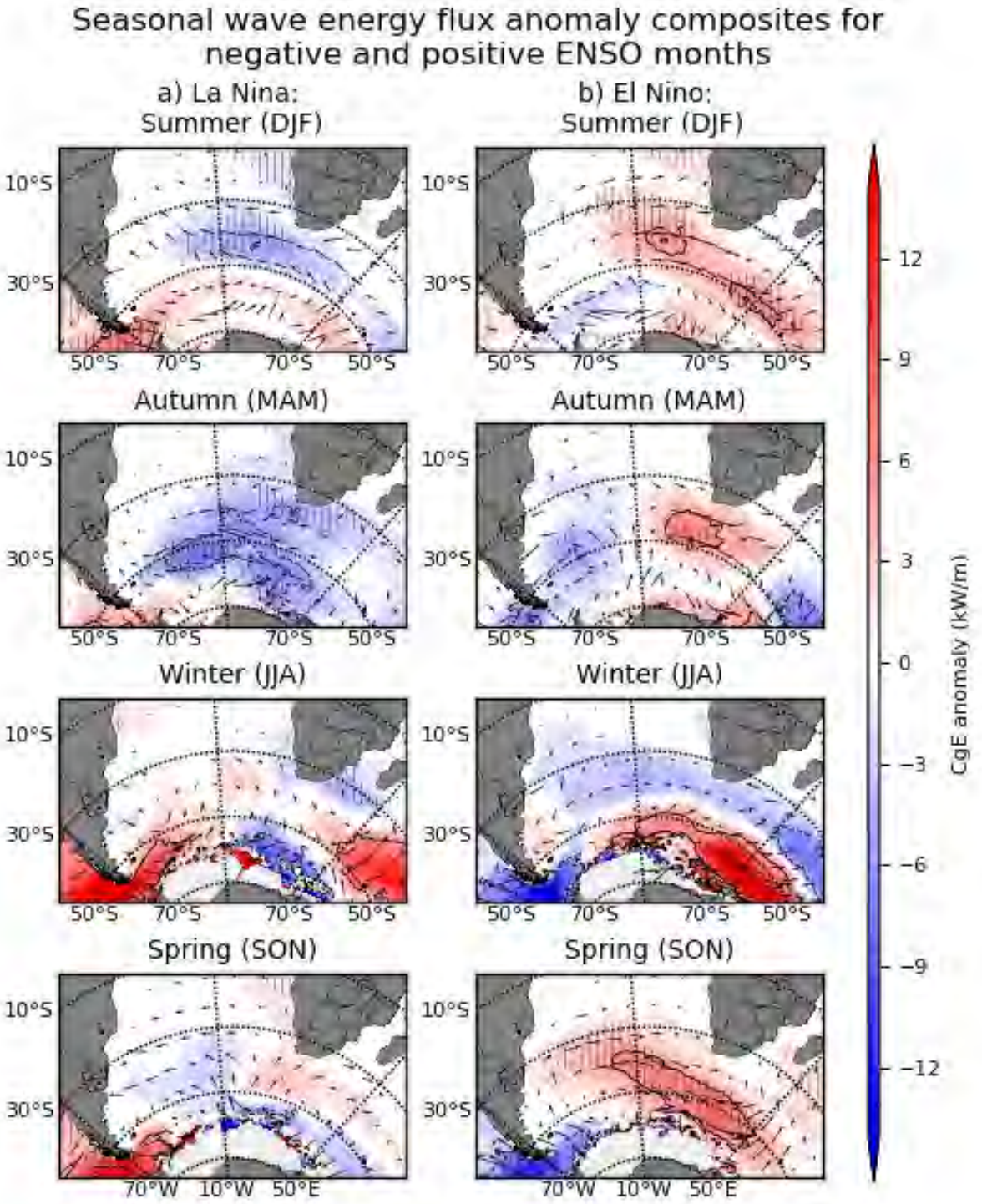

Figure 23: Same as Figure 21 but for negative (La Niña) and positive (El Niño) months. Shading indicates 95% significance. The solid (dashed) contour line indicates anomalies 5 kWm^{-1} above (below) the seasonal mean. The no. of months used for each composite are given in Table A1

Table 7 shows seasonal correlations between significant wave height and the Niño 3.4 index. There are unsurprisingly far fewer significant seasonal correlations when compared to Table 6. Saldanha Bay and Slangkop both show significant correlations with ENSO, in agreement with Figures 22 and 23. East London shows a direct relationship in autumn and winter, confirming the coastally significant

anomalies found in Figure 23. On the east coast, there are significant inverse relations in winter at Durban and in summer at Richards Bay. The Durban response is somewhat present in Figure 23, where El Niño is associated with negative easterly flux anomalies. The differences between the coastal correlations and the model are due to the varying recording period and data coverage as well as the changes due to near-coast bathymetry (Table 1). The SAM and ENSO plots (Figures 20 and 23) reveal that when these modes are out of phase the summer wave energy flux can be significantly enhanced or reduced depending on the combination. A positive SAM and La Niña typically leads to south-easterly wind anomalies and a smaller, more southerly wave energy flux. These relations will be further investigated in Section 4.3.4, but first relationships with the semi-annual oscillation are discussed.

Buoy location:	Summer R	Autumn R	Winter R	Spring R
Saldanha Bay	**0.27**	0.04	0.06	-0.10
Slangkop	**0.46**	-0.13	0.02	0.04
Cape Point	0.08	0.13	0.09	0.004
Mossel Bay	-0.13	0.03	-0.09	0.20
Port of Ngqura	-0.05	0.16	-0.17	-0.09
East London	0.04	**0.32**	**0.27**	0.17
Cooper Light	0.06	0.06	0.25	0.008
Durban	-0.21	0.001	**-0.40**	0.06
Richards Bay	**-0.25**	-0.06	0.01	0.14

Table 7: Seasonal correlations between in-situ significant wave height data and the ERA5 derived Niño3.4 index at a monthly frequency. Bold indicates significance >= 95%.

4.3.3 The Semi-annual Oscillation (SAO)

Similar to the above two assessments, the detrended correlations between the SAO and the 10m wind speed and direction are shown to understand how the wave energy flux and direction respond. The SAO is positively correlated with the SAM (Table 5) therefore, the wind and wavefields should show similar relations to those in section 4.3.1. Year-round both near the coast and offshore wind speed and direction significantly respond to the SAO (Figure 24). Generally, the wind speed over the fetch is negatively correlated, implying stronger winds during negative SAO phases. This patch of negative correlation moves equatorward in the winter months impacting the coastal winds of autumn, winter, and spring. In summer this patch is shifted poleward, and a second patch of positive correlations emerges around 30ºS in both the southeast Atlantic and southwest Indian oceans, a negative SAO phase in summer will dampen these winds. Wind direction is negatively correlated with the SAO from the coastline out into the surrounding oceans. Over summer and spring, this patch is more zonal centred roughly around 35ºS whereas in autumn and more so in winter the patch is far more

meridional, stretching in a northwest-southeast orientation into the southeast Atlantic. The wind direction in this patch rotates anticlockwise (becomes more southerly to south-easterly) during positive SAO events. Also of note is the positive correlation present between wind direction and speed around the Antarctic peninsula (between roughly 50ºS - 65ºS and 70ºW - 60ºE) which maximises in summer. Here the winds will become stronger and more westerly to north-westerly during positive SAO events. Overall, these relationships should translate to the wavefield and significantly influence the waves arriving at the southern African coastline.

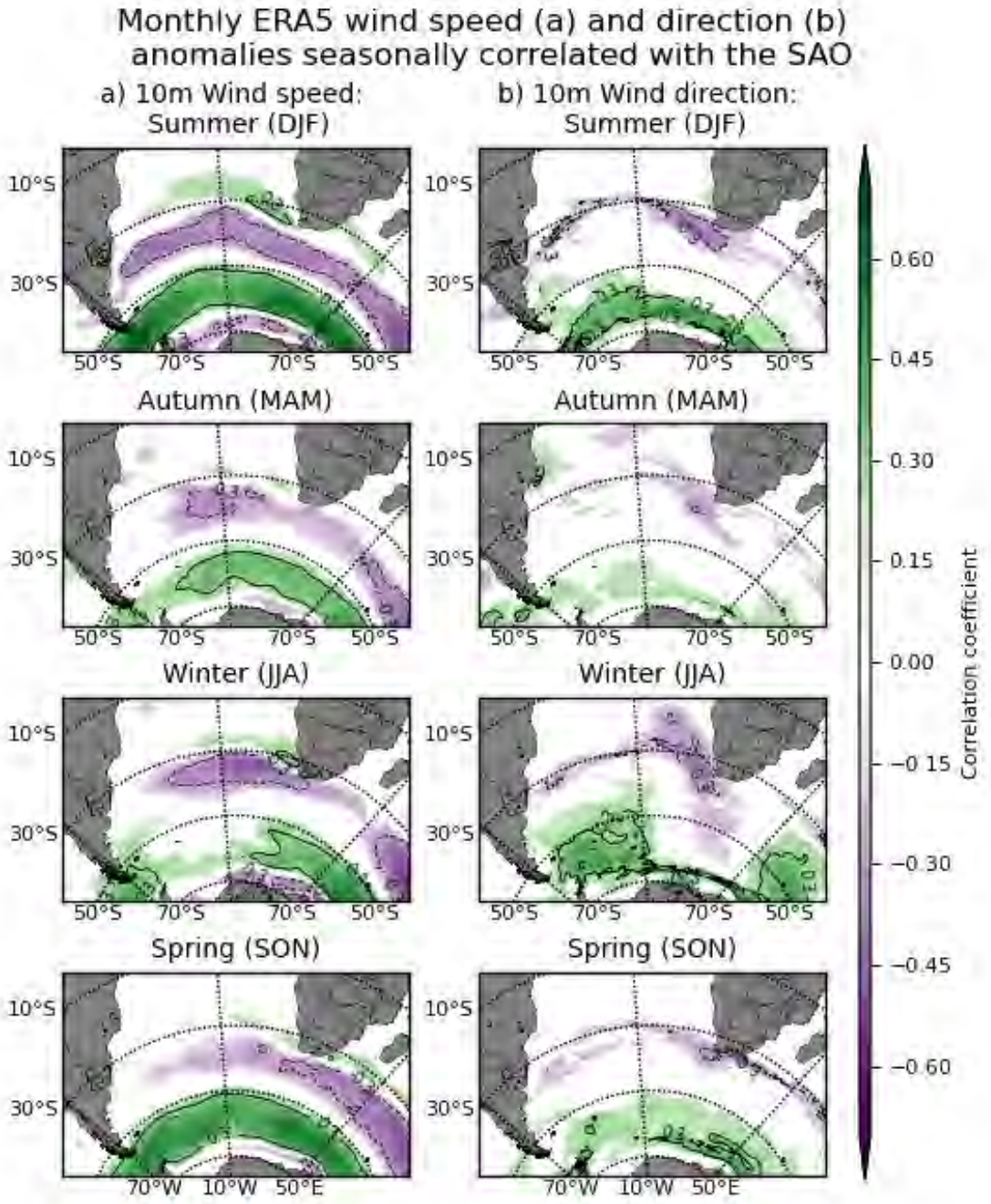

Figure 24: Detrended spatial correlations between the SAO index and 10m wind speed (a) and direction (b). Only correlations significant at the 95% level are shown. The solid (dashed) contour line indicates correlations of 0.3 (– 0.3).

Wave energy flux and direction both significantly respond to the SAO (Figure 25). Over every season there are negative correlations, implying that a positive (negative) SAO will drive below (above) average flux which is anticlockwise (clockwise) rotated or more southerly (westerly). Summer is the only season in which the magnitude of the flux does not significantly respond however it is the season with the strongest direction response affecting the entire South African coastline. The flux correlations maximise in strength over winter, particularly to the southwest of South Africa, and in spatial extent in spring where correlations are significant from the Angolan coastline round to the southern Mozambiquan. Similar to the change of the wind direction correlations, the significant areas of the mean wave direction correlations are more zonal over summer and spring and more meridional over autumn and winter. They show the most spatially extensive response in summer, with inverse relations across the South Atlantic and into the South Indian oceans.

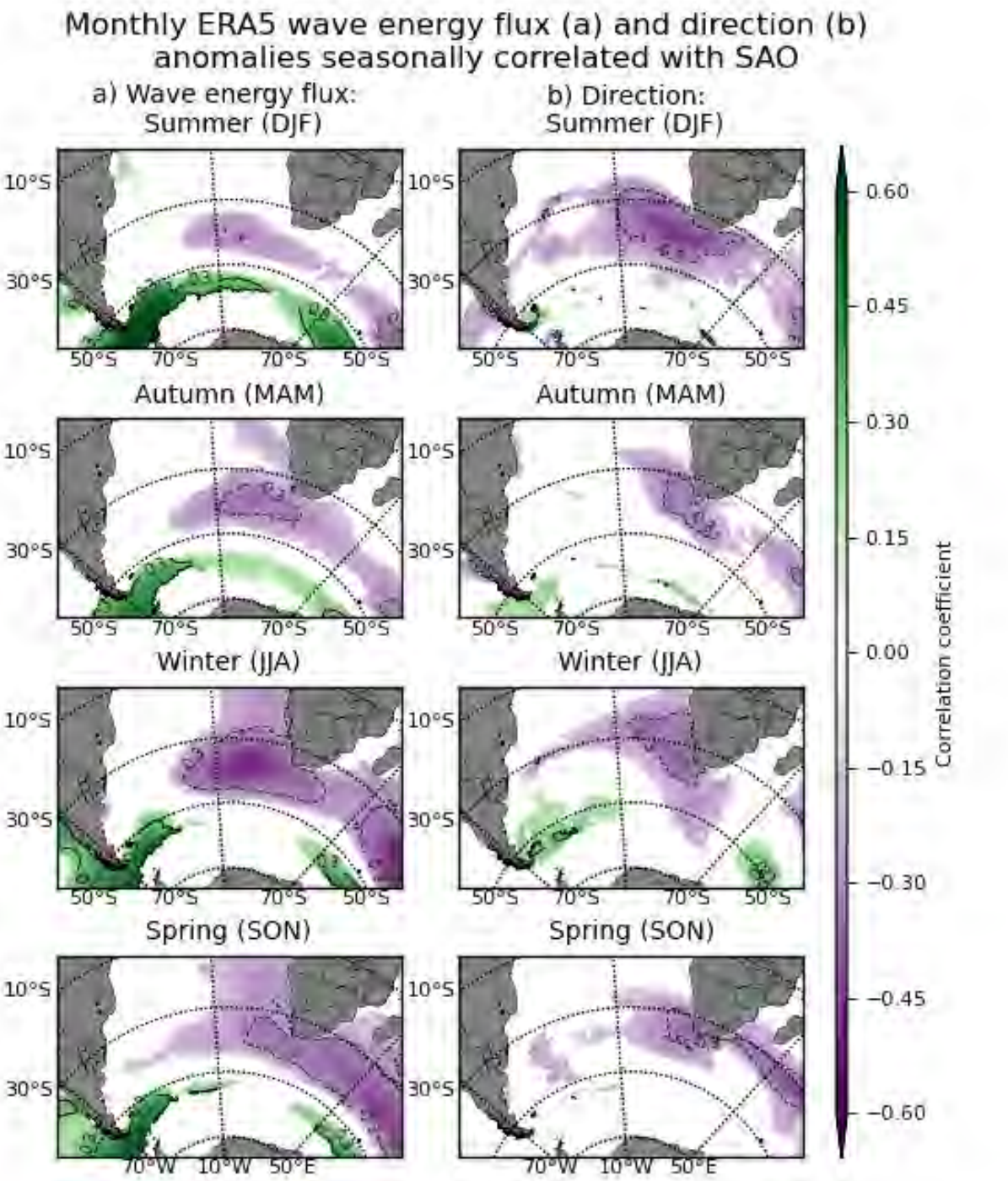

Figure 25: Same as for Figure 19 but for detrended correlations to the ERA5 derived semi-annual oscillation index. Only correlations significant at 95% or greater are shown. The solid (dashed) contour line indicates correlations of 0.3 (– 0.3).

Monthly flux anomaly composites are performed to test whether the waves respond equally to the positive or negative SAO, generally they agree with the direction of the correlations in Figure 25. These composites reveal some large positive anomalies under a negative SAO which do not necessarily translate to large negative ones under positive SAO over the same seasons (Figure 26). Relations to the negative SAO events have a coastal impact between winter and spring with only the

southwest responding significantly in autumn. On the other hand, positive SAO is most impactful between spring and summer, with the region of significant negative anomalies moving offshore to the west over autumn. Although the largest positive anomalies occur in autumn – greater than 12 kW/m above the mean along the southern coastline – they are insignificant except in the southwest due to the SAO rarely being negative over autumn (five out of 120 autumn months). Negative SAO winters show the strongest coastal impact, with positive anomalies greater than 5 kW/m above the mean from the South African Namibian border around to the KwaZulu Natal coast as well as impacting the Madagascan coastline. Conversely under a positive SAO, the strongest negative anomalies occur along the coast in spring which amounts to less than – 3 kW/m below the seasonal mean and stretches from the Angolan coast southwards to the south coast of South Africa. Positive SAO also significantly affects the flux in summer but more so in the west and southwest. The positive phase does not occur over the winter months in the record. The above analysis shows the SAO as most influential over spring, in line with previous relations found with cut-off low frequency (Singleton and Reason, 2007). Depending on the phase, these anomalies will show up one season earlier (winter, negative SAO) or last one season longer (summer, positive SAO) (Figure 26).

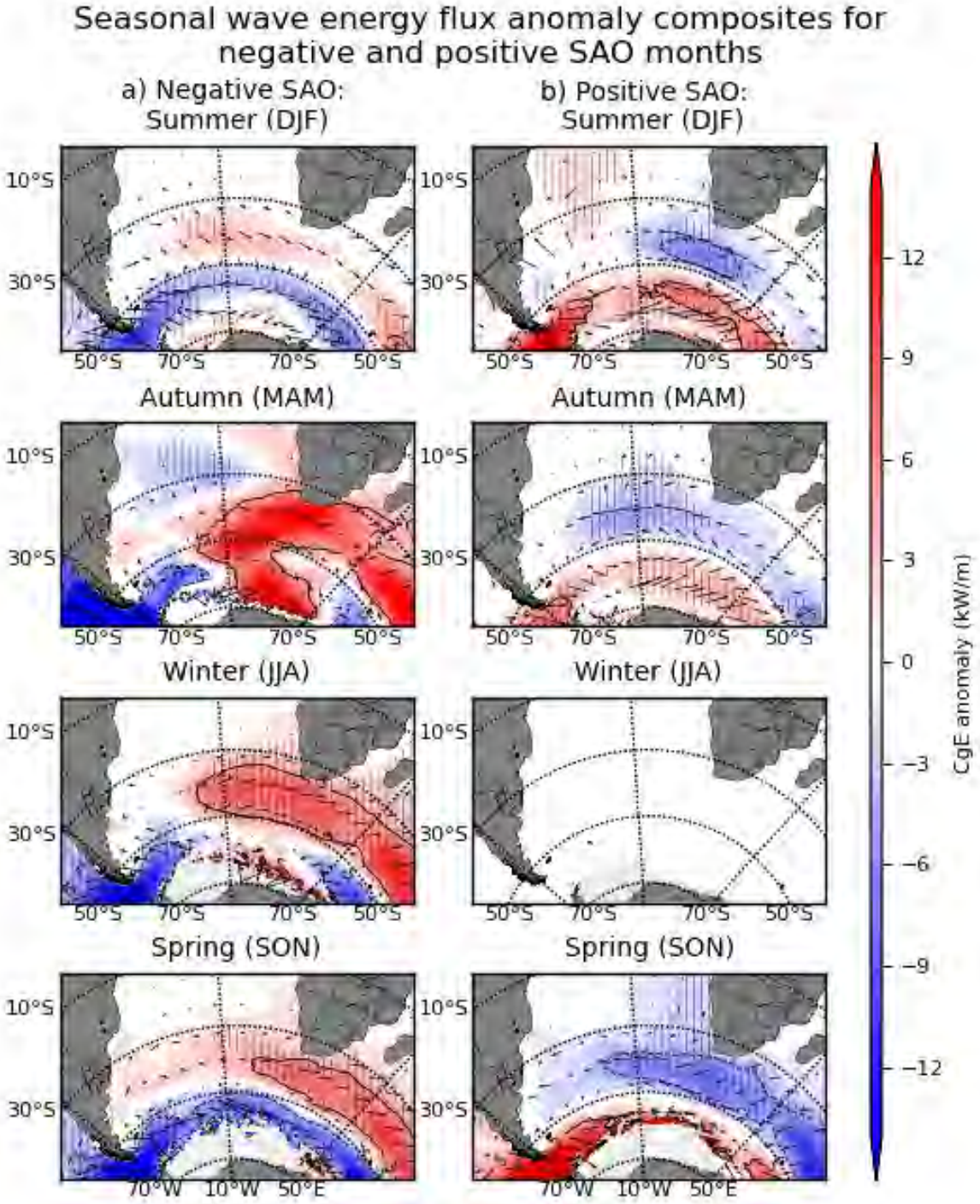

Figure 26: The same as Figure 19 but for seasonal composites under negative and positive SAO events. The shading indicates significance at the 95% level. The solid (dashed) contour line indicates anomalies 5 kW/m above (below) the seasonal mean. The no. of months used for each composite are given in Table A1

Similar to the previous sections, the relationships with in-situ significant wave height data are investigated to test whether these relations translate to the coastal zone (Table 8). Saldanha Bay is the only location where correlations are significant for all seasons, with the strongest correlation

occurring in winter (r = -0.37). This agrees with the year-round negative correlations (Figure 25) with a stronger flux impacting the coastal zone when the SAO is negative. The in-situ Cape Point data reveal that after the 1990s move of the instrument from Slangkop to Cape Point, the wave record showed more significant seasonal correlations. At Slangkop, only spring responded significantly ($r = -0.41$, $p < 0.05$) whereas at Cape Point the correlations were significant between autumn and spring ($r = -0.35$, $p < 0.05$). The strongest seasonal relation occurs over summer at the Durban wave rider ($r = 0.53$, $p < 0.05$), which is likely due to the north-easterly wave direction anomalies under a positive SAO. A strong direction relation is also present at the Port of Ngqura during summer ($r = 0.44$, $p < 0.05$), which are also due to these north-easterly wave direction anomalies under positive SAO. The only remaining significant relationships occur at East London in spring and Richards Bay in winter, both are negative and in agreement with the spring and winter composites (Figure 25).

Buoy	Summer R	Autumn R	Winter R	Spring R
Saldanha Bay	**-0.27**	**-0.32**	**-0.37**	**-0.30**
Slangkop	-0.21	-0.26	-0.28	**-0.41**
Cape Point	-0.19	**-0.25**	**-0.29**	**-0.35**
Mossel Bay	0.14	-0.00	0.10	-0.10
Port of Ngqura	**0.44**	0.33	0.04	-0.12
East London	-0.02	-0.13	0.03	**-0.27**
Cooper Light	-0.02	-0.18	0.20	0.18
Durban	**0.53**	0.01	-0.15	0.14
Richards Bay	0.16	0.03	**-0.21**	-0.03

Table 8: Correlations between in-situ significant wave height and the ERA5 derived SAO index at the monthly frequency. Bold indicates significance greater than 95%.

4.3.4 Climate Mode Combinations

The previous section has shown that some seasons and locations show robust relationships of the wave climate with the various climate modes, SAM, ENSO, and the SAO. Using monthly anomalies various combinations between phases of these climate modes were considered. However, due to the relatively low number of co-occurrences and the monthly frequency, this analysis cannot be done seasonally. First, the impact of only one mode active (dependent on the other two in a neutral phase) is assessed against the impact of one mode active independent of the phase of the other two (Table 9, Figure 27). Some interesting differences emerge.

Negative SAM only impacts the southwest and west coast marginally when it is the only active mode, whereas when the other modes are active, the positive anomalies shift eastward and cause changes around South Africa's coast (Figure 27c – d). The direction also becomes more zonal across the

oceans south of South Africa when SAM is negative with other modes active. The same is true for the direction under positive SAM with other active modes compared to just positive SAM (Figure 27a – b). The direction anomalies are ENE under just positive SAM and swing more easterly with multiple active modes. Unlike negative SAM, the positive phase impacts the coast more when it is the only active mode (Figure 27a – b).

El Niño hardly impacts the coast over the whole period which is not surprising given the strong seasonality in the impact of this mode (Section 4.3.2). The anomalies are in line with the strengthening and southward shift in the storm tracks characteristic of the South Atlantic El Niño response (Figure 23, (Pezza *et al.*, 2008). The strongest response is located south of South Africa where this enhanced storm track drives an above-average flux (Figure 27 a – b). The direction again becomes more zonal with greater impact on the coast when multiple modes are active under El Niño conditions, which could be due to the ability of certain El Niño events to excite a negative SAM (Yu *et al.*, 2015). La Niña shows shifts in the direction of the anomalies with slightly positive anomalies for the independent events, which become slightly negative when the phases of the other modes are disregarded (Figure 27c – d). This result again points to the ability of certain La Niña events to excite a positive SAM.

The SAO also shows changes when just it is active compared to when the phase of other modes is ignored. Positive SAO events are associated with northeasterly negative flux anomalies south of South Africa, which move northward and become more zonal when disregarding the phase of the other modes. Similarly, when just a negative SAO is present there are west-southwesterly positive flux anomalies that shift northward and strengthen affecting a large section of the southern African coastline when the phase of the other modes is disregarded (Figure 27 c – d). Given the relatively strong association between SAM and the SAO, r = 0.6 (Table 5), with no months existing when one is positive and the other is negative, these changes again seem linked to the presence of an active SAM.

Mode	**Sample size**			
	Independent		**Dependent**	
	Positive months	**Negative months**	**Positive months**	**Negative months**
SAM	80	77	35	24
ENSO	63	65	31	29
SAO	69	90	32	38

Table 9: The sample sizes used to plot Figure 27 of the different phases of each mode independent of the phase of the other two and dependent on the other two in a neutral phase.

Comparing the dependent vs. independent states of the active modes in Figure 27 shows how necessary it is to look at the entire picture when assessing the impact of individual climate modes on the wavefield. Combined with the seasonal composites and correlations found in the previous

sections, it was suspected that certain combinations could lead to significantly above (below) average flux in the oceans surrounding southern Africa. There is an inverse relationship between wave energy flux and both the SAM and SAO, while a direct relationship exists between ENSO and the wave record (Figure 27). Constructive modal interference could cause both. For example, positive flux and westerly direction anomalies surrounding South Africa may occur when a negative SAM, negative SAO, and El Niño combine whereas negative flux and easterly direction anomalies can happen under a combination of positive SAM, positive SAO, and La Niña. In theory, the strongest anomalies should occur when all three of these modes combine constructively however combinations of at least two will still change how the wave energy flux fields respond.

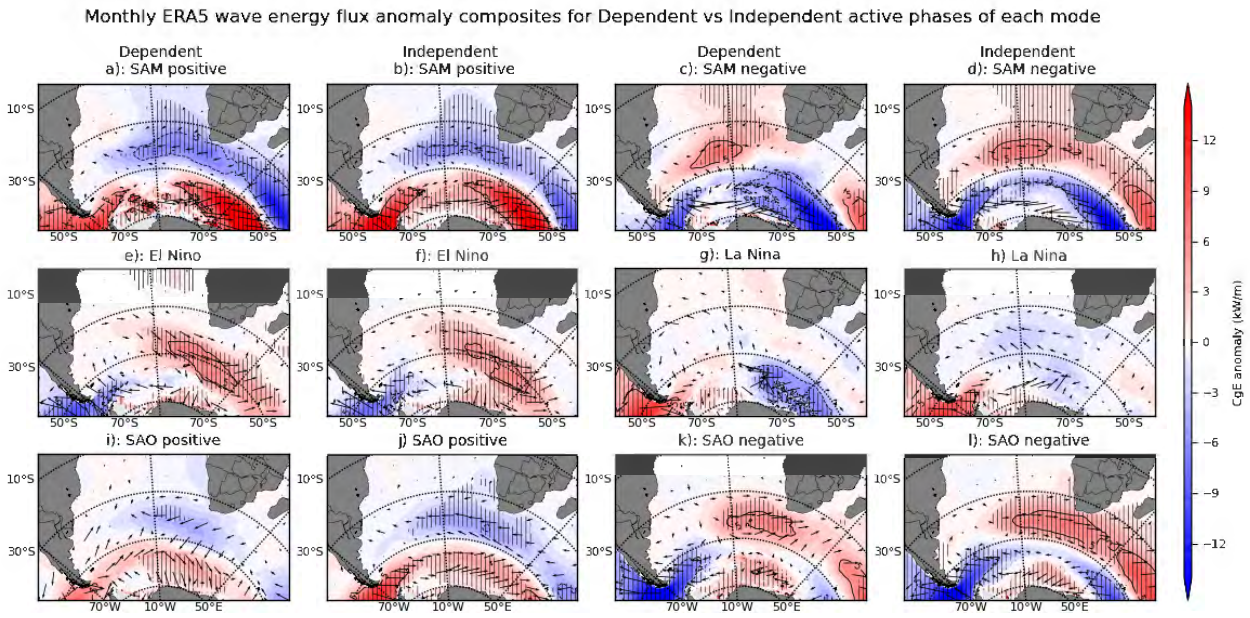

Figure 27: Composites of the positive and negative phases of SAM, ENSO, and the SAO for months when the mode in question is active dependent on the other two modes being in a neutral phase (Dependent columns) compared to composites when only the mode in question is active independent of the other two (Independent columns). The phase is defined by an exceedance of one standard deviation away from the mean in the positive or negative direction and the sample sizes of each composite given in Table 9. The solid (dashed) contour line indicates anomalies 5 kW/m above (below) the mean.

These hypothesized relationships are investigated in Figure 28, using composites under the above-mentioned phase combinations. The relative sample size used for each composite is shown in Table 10. The most coastally significant positive anomalies occur when a negative SAM and negative SAO combine with a neutral ENSO (Figure 28 b). This combination leads to positive and westerly anomalies from the Angolan Namibian border round to Mozambique, with the strongest anomalies along the southern African coast. Although these anomalies strengthen when including an active El Niño they tend to move offshore, becoming coastally insignificant (Figure 28 f). The shift south-

westward agrees with the above-mentioned impact of El Niño on the southern hemisphere jet streams and storm tracks (Pezza *et al.,* 2008). From Figure 27, negative SAM brings the western coastline significance whereas negative SAO brings the eastern coastline significance. Negative and easterly coastal anomalies are generally associated with the positive phase of both SAM and the SAO (Figures 20, 26 and 27). When positive SAM and SAO months are combined with a La Niña event, the strongest negative coastal anomalies occur, again reaching from the Angolan coastline round to the east coast of South Africa (Figure 28 e). The south coast again responds the strongest and northeasterly wave direction anomalies are present. These relationships show how both constructive and destructive modal interference significantly influences the interannual variability in the southern African wave climate in the coastal zone.

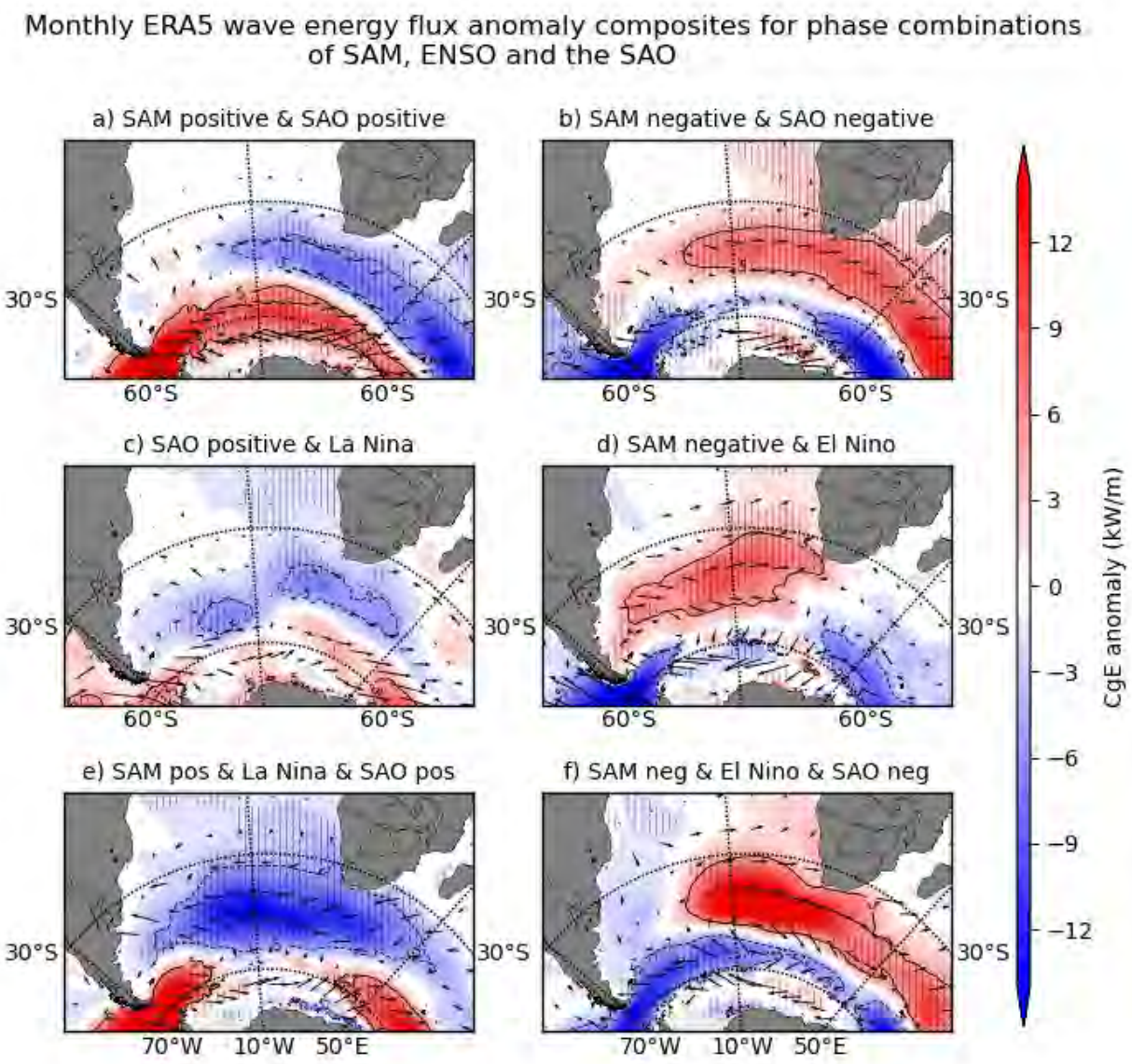

Figure 28: Composites created from monthly wave energy flux and mean wave direction anomalies for various combinations of different phases of the atmospheric modes. Shading indicates the 95%

significance level. The solid (dashed) contour line indicates anomalies 5 kW/m above (below) the mean.

Combination:	Sample size (months)
+ SAM, neutral ENSO, + SAO	17
Neutral SAM, La Niña, + SAO	13
+ SAM, La Niña, + SAO	5
- SAM, neutral ENSO, - SAO	34
- SAM, El Niño, neutral SAO	7
- SAM, El Niño, - SAO	5

Table 10: The sample sizes of the combinations used in Figure 28

Finally, seasonal partial correlations are presented between in-situ significant wave height and one mode controlling for the variability associated with the other two modes. Comparisons between the partial correlations (Tables 11, 12, and 13) and the standard correlations (Tables 6, 7, and 8) allows us to determine whether the relationship is to the climate mode or if it is due to the climate mode's relationship to another climate mode. This is particularly useful when 2 modes are significantly correlated as are SAM and the SAO (Table 5). Tables 11, 12, and 13 show the partial correlations between the in-situ data and the mode in question. SAM stands out as the dominant signal in the monthly near-coast significant wave height anomalies. Generally, the partial correlations with SAM are weaker than the standard correlations implying the relationship to the in-situ significant wave height is weaker when removing the variability associated with ENSO and the SAO. This decrease is most prominent along the west and southwest in the transition and summer seasons, where some seasons correlation coefficients drop by up to 0.2 (Table 11 vs Table 6). Saldanha Bay loses significance in autumn, Slangkop in summer, and Cape Point in spring. These are the active seasons for both the ENSO and the SAO, during which they show their strongest influence as shown in Sections 4.3.2 and 4.3.3. Other changes include those at the Port of Ngqura where the strong summer positive correlation drops to near zero in the partial correlation, and East London which is the only location to show a stronger partial correlation compared to the standard correlation. The increase occurs in winter, suggesting that the SAO and ENSO generally reduce the influence of SAM in this region. Similarly, to the west and southwest, the East London result weakens to become statistically insignificant in spring.

For the ENSO partial correlations, nearly all the significant relationships found in Table 7 are present in Table 12. Only the summer negative correlation disappears from the Richards Bay station, with the others showing small decreases in strength, more so in the west and southwest. Given research showing how certain ENSO events can excite the SAM (Lim *et al.*, 2013; Yu *et al.*, 2015), this minimal change comes as a surprise particularly compared to the changes in the relationships to SAM

and the SAO. The SAO partial correlations show the most difference from the standard correlations (Table 13 vs Table 8). In fact, all but one significant correlation remains, the winter negative correlation at East London. Table 5 shows a strong SAM SAO correlation (r = 0.6), with no simultaneous occurrences of positive SAM and negative SAO, they are either both active in the same direction or one is neutral while the other is active. This large decrease in influence also stands out in Figure 27 i – l, where active SAO vs active SAO and other modes neutral shows the largest change.

Overall, these results point to SAM and ENSO as the leading modes in the wave record around the South African coastline with the SAO acting to enhance these anomalies when concurrently active (Figure 27). Based on these results, the large anomalies in the time series (Figure 15) at various times can now be assessed further. The 1992/1993 positive anomalies coincided with negative SAM, SAO, and an El Niño Modoki event which drove changes in the storm tracks and 10m winds leading to significant changes in the wavefield around the South African coast in line with those in Figure 28 b), d), f). Nearly all positive (negative) anomalies in flux or direction are associated with negative (positive) SAM and SAO phases (Figure 17). The 1999/2000 and 2011 La Niña, positive SAM and SAO similarly led to the negative direction and flux anomalies like those in panel e) of Figure 28. The dip in both flux and direction around 2005 also co-occurred with positive SAM and SAO, however no active ENSO was present. These modes can also interfere destructively, for example, the strong 2015/2016 El Niño did not lead to above-average flux as during this period SAM was generally positive, counteracting the normal response. Around 2012/2013, the 5-year cycle ends, which could be due to this dissociation between the SAM and ENSO which manifested in the synchronised 2015/2016 phases of all 3 modes.

Southern Annular Mode (SAM)	**Partial correlation coefficient**				
	Period				
Buoy location:	**1980 – 2019**	**Summer**	**Autumn**	**Winter**	**Spring**
Saldanha Bay	**0.27**	**-0.32**	-0.19	**-0.20**	**-0.24**
Slangkop	-0.16	-0.31	0.07	-0.12	**-0.39**
Cape Point	**-0.29**	**-0.30**	**-0.29**	**-0.26**	0.22
Mossel Bay	-0.06	-0.21	0.22	-0.22	0.05
Port of Ngqura	0.01	-0.01	0.29	-0.16	0.12
East London	**-0.23**	-0.19	**-0.25**	**-0.35**	-0.14
Durban	0.04	0.12	0.11	-0.10	0.19
Richards Bay	-0.09	-0.01	-0.14	**-0.20**	-0.06

Table 11: Seasonal partial correlations between SAM and the in-situ significant wave height data at a monthly frequency controlling for the SAO and ENSO. Bold indicates 95% significance.

El Nino Southern Oscillation (ENSO)	**Partial correlation coefficient Period**				
Buoy location:	**1980 – 2019**	**Summer**	**Autumn**	**Winter**	**Spring**
Saldanha Bay	0.03	**0.20**	0.01	0.11	-0.15
Slangkop	0.06	**0.35**	-0.03	0.04	0.01
Cape Point	0.04	0.05	0.20	0.14	-0.06
Mossel Bay	0.01	-0.11	-0.11	-0.06	0.21
Port of Ngqura	-0.05	-0.09	-0.01	-0.15	-0.04
East London	**0.16**	0.06	**0.31**	**0.31**	0.09
Durban	-0.11	-0.12	-0.07	**-0.37**	0.06
Richards Bay	-0.04	-0.19	-0.08	0.01	0.14

Table 12: Seasonal partial correlations between ENSO and the in-situ significant wave height data at a monthly frequency controlling for the SAO and SAM. Bold indicates 95% significance.

Semi-annual Oscillation (SAO)	**Partial correlation coefficient Period**				
Buoy location:	**1980 – 2019**	**Summer**	**Autumn**	**Winter**	**Spring**
Saldanha Bay	-0.04	0.09	-0.14	-0.13	-0.05
Slangkop	-0.07	0.19	-0.23	-0.15	0.02
Cape Point	-0.01	0.05	-0.05	-0.01	-0.08
Mossel Bay	0.07	0.22	-0.11	0.24	-0.12
Port of Ngqura	0.09	0.31	0.14	0.20	-0.16
East London	0.09	0.12	0.06	**0.25**	-0.08
Durban	0.07	0.31	-0.05	-0.01	-0.04
Richards Bay	0.03	0.07	0.04	-0.02	0.02

Table 13: Seasonal partial correlations between the SAO and the in-situ significant wave height data at a monthly frequency controlling for SAM and ENSO. Bold indicates 95% significance.

5. Summary and Conclusions

Through the investigation into the long-term wave energy flux variations around the southern African coastline, some important conclusions can be drawn. Firstly, the accuracy of two global deep water ocean wave hindcast products were evaluated. ERA5 showed marginal outperformance against both in-situ and altimeter data when compared to the CAWCR around the South African coastline. This marginally better representation of the past wave climate agrees with research comparing hindcasted winds, in which ERA5 was 30% more accurate than an ensemble mean (Ramon *et al.*, 2019). In ERA5 there is a direct coupling between atmosphere and ocean which should better represent the dynamics between the two. The CAWCR has been shown to be inhomogeneous due to an upgrade in both wind forcing and wave model physics which could have imparted inconsistencies particularly when performing trend analysis (Smith *et al.*, 2021). Although ERA5 still has deficiencies, it is more consistent and has been used in the determination of long-term trends (Amrutha and Sanil Kumar, 2019; Takbash and Young, 2020). One such inconsistency in the product is the apparent increase in variability due to the increase in global altimeter coverage in 1992, however Timmermans *et al.* (2020) compared both the hindcast with assimilation and without, finding no significant changes due to the 1992 increase in coverage. ERA5 was chosen to assess long-term variations in the wave energy flux around the southern African coastline.

Emerging from the evaluation of these two hindcasts is the strong seasonal signal characteristic of the Southern African coastline. Generally, wave energy flux peaks over the winter months when the storm and wind belt expand northwards and reaches a minimum over summer where the storm and wind belt are most contracted (Figure 13). The in-situ data revealed how the timing of this peak shifts later moving further eastwards around the coastline, pointing to the increasing significance of cut-off lows in generating these intense waves. Another interesting factor emerged from the comparison of the Slangkop (old Cape Point buoy location, further offshore, Table 1) and the Cape Point climatologies. The latter showed a clear bimodal peak in June and August whereas the former had a single peak in July. The change is in line with the post 1990s increase in wave variability found in Section 4.2. The long-term changes in the wave climate were first assessed using Mann-Kendal trend analysis on the seasonal means. The results showed significant increasing meridional flux year-round, but more prominently over spring and summer. Spring was the only season with significant increases in both meridional and zonal wave energy flux. These increases are in line with the later peak in the east coast seasonal cycle as well as the tendency toward more frequent cut-off lows in the spring months (Singleton and Reason, 2007).

A more detailed analysis agreed with these seasonal trends, the waves are becoming more powerful and slightly more southerly over the period 1979 and 2020 (Figure 15). Within this general increase, wavelet analysis revealed a significant 5-year cycle that starts later and lasts longer further eastwards around the coast. During the period 1997 – 2012, the direction and flux anomalies are more strongly correlated than over the whole period (Table 4). It may be suggested that this higher variability is due to the out of phase relationship between SAM and ENSO over this period. After the 1990s the El Niño (La Niña) Modoki/central Pacific type began to more frequently modulate the SAM phase, particularly to excite a negative (positive) SAM over late autumn to early winter (Lim, Hendon and Rashid, 2013; Yu *et al.*, 2015). This has led to ENSO having a stronger influence on the southern hemisphere climate since the 1990s through this teleconnection to SAM. During the more variable 1997 – 2012 period, inter-mode correlations revealed a significant inverse relation between both SAM and ENSO as well as the SAO and ENSO. The role of this synchronization in the wave record could only be truly understood by assessing how each mode affects the wave energy flux and direction anomalies within the ERA5 reanalysis.

First, an understanding of each modes impact regardless of what other modes were active was achieved through correlations between and composites of wave energy flux and direction. Next, multi-mode composites and partial correlations were used to see if these relations held when controlling for concurrently active modes. Each mode showed significant seasonal correlations to 10m winds, which translated to significant correlations in the wave energy flux fields for at least two seasons.

The strongest correlations to the wave energy flux field were found to be with SAM, particularly over the spring and winter seasons (Figure 19). These were also the only seasons showing coastally significant anomalies in the SAM composites (Figure 20). Wave energy flux and direction had a significant negative correlation year-round, in line with the in-situ significant wave height correlations at Saldanha Bay, Cape Point, and East London (Table 6). The anomaly composites indicate that the most robust coastal response occurred under negative SAM in spring and positive SAM in winter, however, the modifications to the offshore climate could translate into the coastal record through changing the waves in the generation zones where there is a significant response year-round. Summer shows the strongest negative correlation with wave direction, during which a positive SAM will rotate the mean wave direction anticlockwise turning it more southerly to south-easterly. The in-situ data showed the strongest responses between spring and summer in line with the strong flux and direction correlations (Figure 19, Table 6). When compared to the in-situ partial correlations controlling for ENSO and the SAO, the coefficients generally decreased in strength with no stations showing significance for all seasons. Saldanha Bay and Cape Point both showed significance for three seasons, these being summer, winter, and spring at Saldanha Bay and summer, autumn, and winter at Cape

Point (Table 6 vs. Table 11). Generally, the strongest decreases coincided with the active seasons for both ENSO (summer) and the SAO (autumn and spring) in line with the dropping of the significant anomalies under only SAM negative (Figure 28).

ENSO showed a strong impact on the summer wave climate in the form of direct wave energy flux and direction correlations and significant near-coast negative anomalies under La Niña (Figures 22 and 23). El Niño did lead to significant positive anomalies although only slightly offshore of South Africa, in line with the associated spring and summer strengthening of the jet stream. The in-situ correlations showed some significance, with the strongest direction relation occurring over summer at Slangkop, $r = 0.46$ ($p < 0.05$), and indirect relation occurring over winter at the Durban station, $r = -0.40$ ($p < 0.05$). When comparing to the partial correlations controlling for SAM and the SAO all associations weaken, with only the summer Richards Bay relation dropping below the significance level. These small decreases in strength show how ENSO events can significantly impact the flux and direction, particularly over the summer months.

Finally, the impact of the semi-annual oscillation (SAO) on the flux and direction fields was assessed. When looking at just the SAO, strong seasonal correlations and large significant anomalies emerged (Figure 25 and 26). The composites revealed a significant near-coast response to both phases in spring, only negative SAO in winter and positive SAO in summer. The in-situ correlations agree with these composites, with a significant negative correlation year-round at Saldanha Bay and in the autumn, winter, and spring seasons at Cape Point (Table 8). The strongest relations occurred over winter at Saldanha Bay, spring at Cape Point, and summer at Port of Ngqura and Durban. Durban showed the strongest direct relation, implying above-average flux over summer under positive SAO. When compared to the partial correlations controlling for SAM and ENSO, nearly all these relations drop below the significance level. This comes as no surprise given the strong association between SAM and the SAO ($r = 0.6$, $p < 0.05$, Table 5) and the fact that no months exist when both are in opposing phases (Table 13). Figure 27 i – l backs this up, with large decreases in significant areas when holding the other two modes in a neutral phase compared to the plots with the phase of the other two modes is disregarded.

In conclusion, SAM shows the strongest control on the wave record, with more of a seasonal response present for ENSO and the SAO. Generally, a negative SAM will lead to above-average flux and westerly direction anomalies across all seasons with the strongest mean wave direction response occurring over spring and summer (Figures 19, 20 and 27). The ENSO influences mainly the summer wavefields, more so under La Niña events where there are negative flux and southerly wave direction anomalies (Figure 23). Summer is the mature phase of ENSO and shows the strongest impacts on atmospheric circulation over southern Africa and the nearby oceanic regions (Reason *et al.*, 2000). The SAO seems to act more to amplify the anomalies rather than directly drive them since its

presence under certain phases of the main drivers (SAM and ENSO) can lead to more intense departures from the mean state.

Given the existing operational accuracy in the forecasting of ENSO and the knowledge that certain El Niño (La Niña) events can significantly excite the negative (positive) SAM – central pacific events predict the SAM phase in the late autumn to early winter months, whereas classic (or canonical) events give insight into the late spring to summer SAM phase (Lim, Hendon and Rashid, 2013) – and the more recent research showing significant skill in the 6-month forecasting of these central Pacific events using neural networks (Pal *et al.*, 2020). These forecasts used in combination with the relationships found in this thesis between the magnitude and direction of the wave energy flux arriving at the southern African coastline and the modes investigated, there may be some seasonal predictability in wave climate. If this predictability proves to be robust, it could provide vital information to those at risk of coastal inundation, structural erosion, coastal engineering, offshore engineering, and the tuning of wave energy converters. Ultimately the ability to predict a coming season's severity will depend on the ability to forecast the ENSO, the SAM, and the SAO phases.

The use of daily outputs from a high-resolution coupled wave-current model can be recommended in trying to understand how these relationships affect the near-coast energy flux at higher temporal and spatial scales. Given the global increasing wave energy trend (Reguero, Losada and Méndez, 2019; Meucci *et al.*, 2020), research into the projected changes under various degrees of future global warming is recommended to understand how the combined changes to both the waves, sea-level rise and storm intensities will impact the southern African coastline. Finally, given the large influence of these climate modes on not only waves but also wind and precipitation across southern Africa that a unified climate mode outlook site should be introduced, similar to those created by the Australian Bureau of Meteorology and the U.S. NOAA outlook sites with a focus on southern African impacts.

APPENDIX

A Buoy evaluation

In this section, scatter plots and Taylor diagrams of Tp and Dp anomalies are shown. The statistics used to plot these figures are given in tables A1 and A2 respectively.

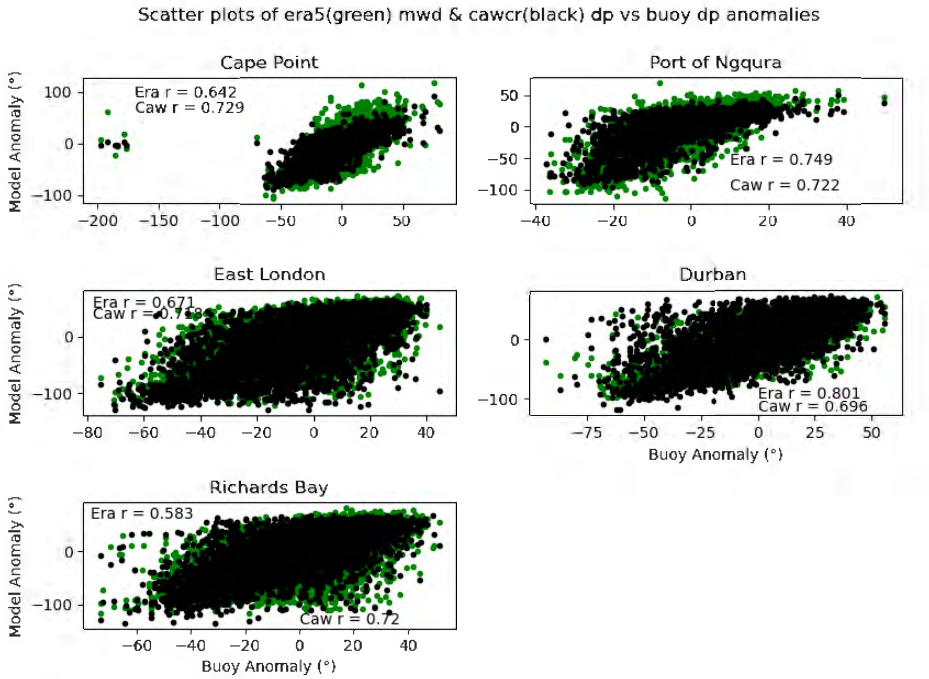

Figure A1: As for figure 9 but for ERA5 mean wave direction and CAWCR peak direction against buoy peak direction anomalies.

From figure A4 and table A2, it is clear that ERA5 outperforms the CAWCR for the peak wave period variable.

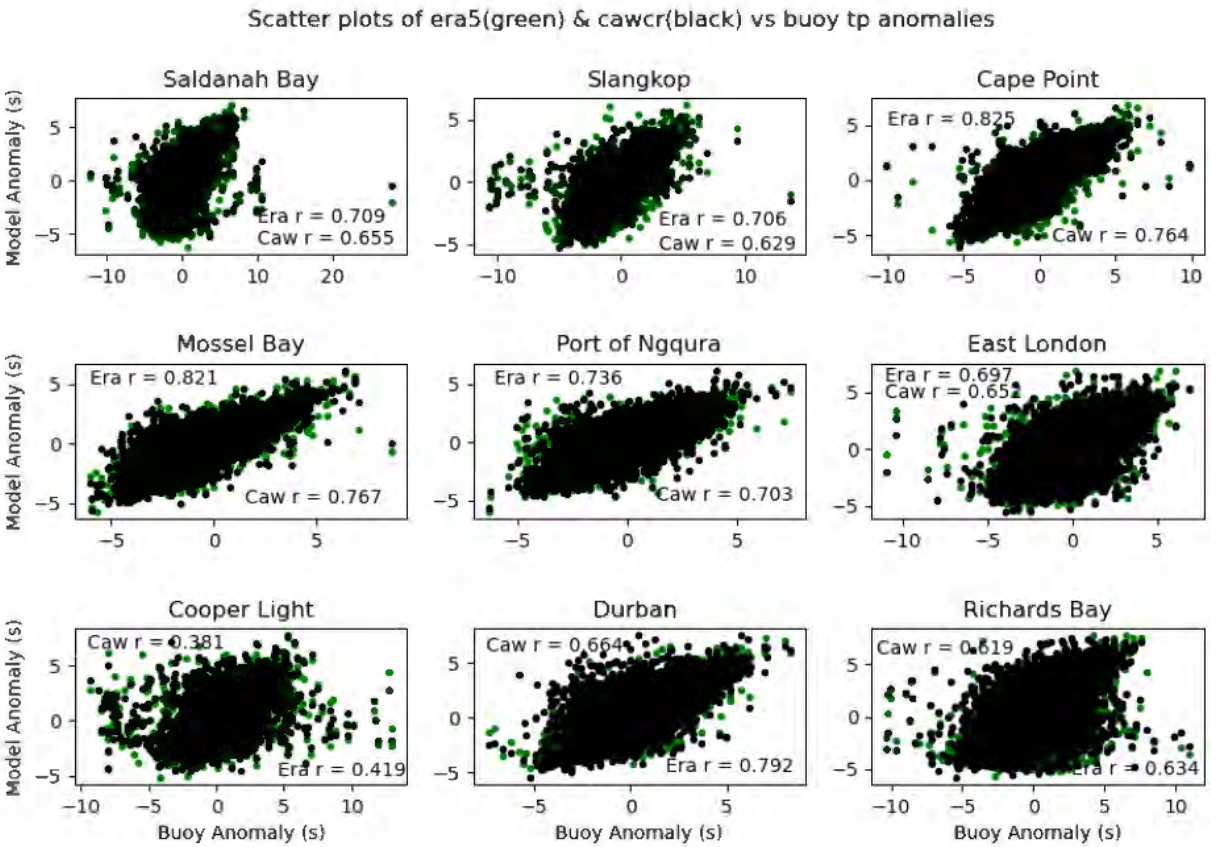

Figure A2: Scatter plots of hindcast vs buoy peak period anomalies. R for each hindcast is shown on the plot

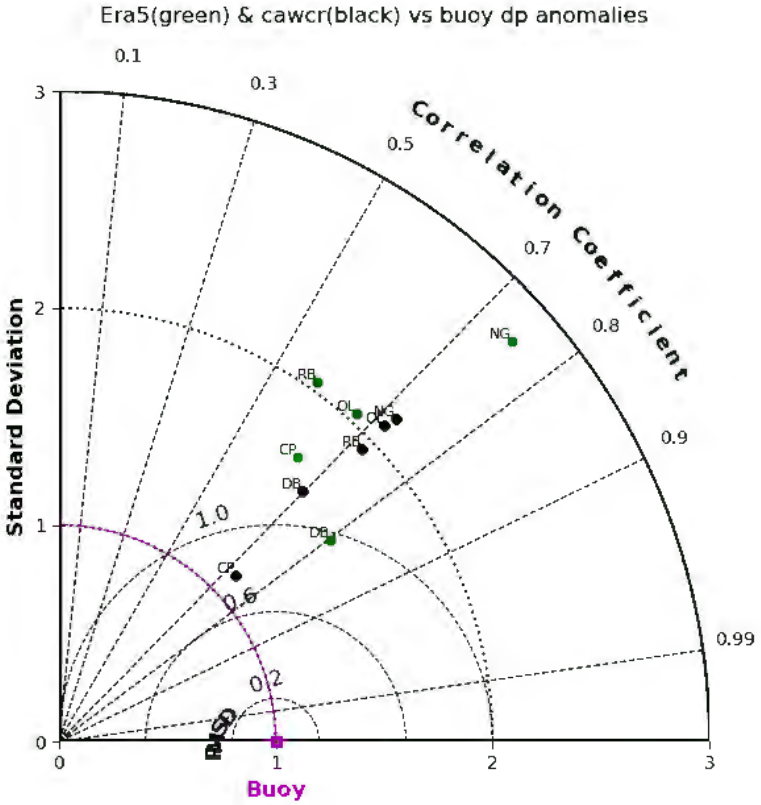

Figure A3: As for figure 10 but comparing ERA5 mean wave direction and CAWCR peak wave direction anomalies to the buoy peak direction anomalies.

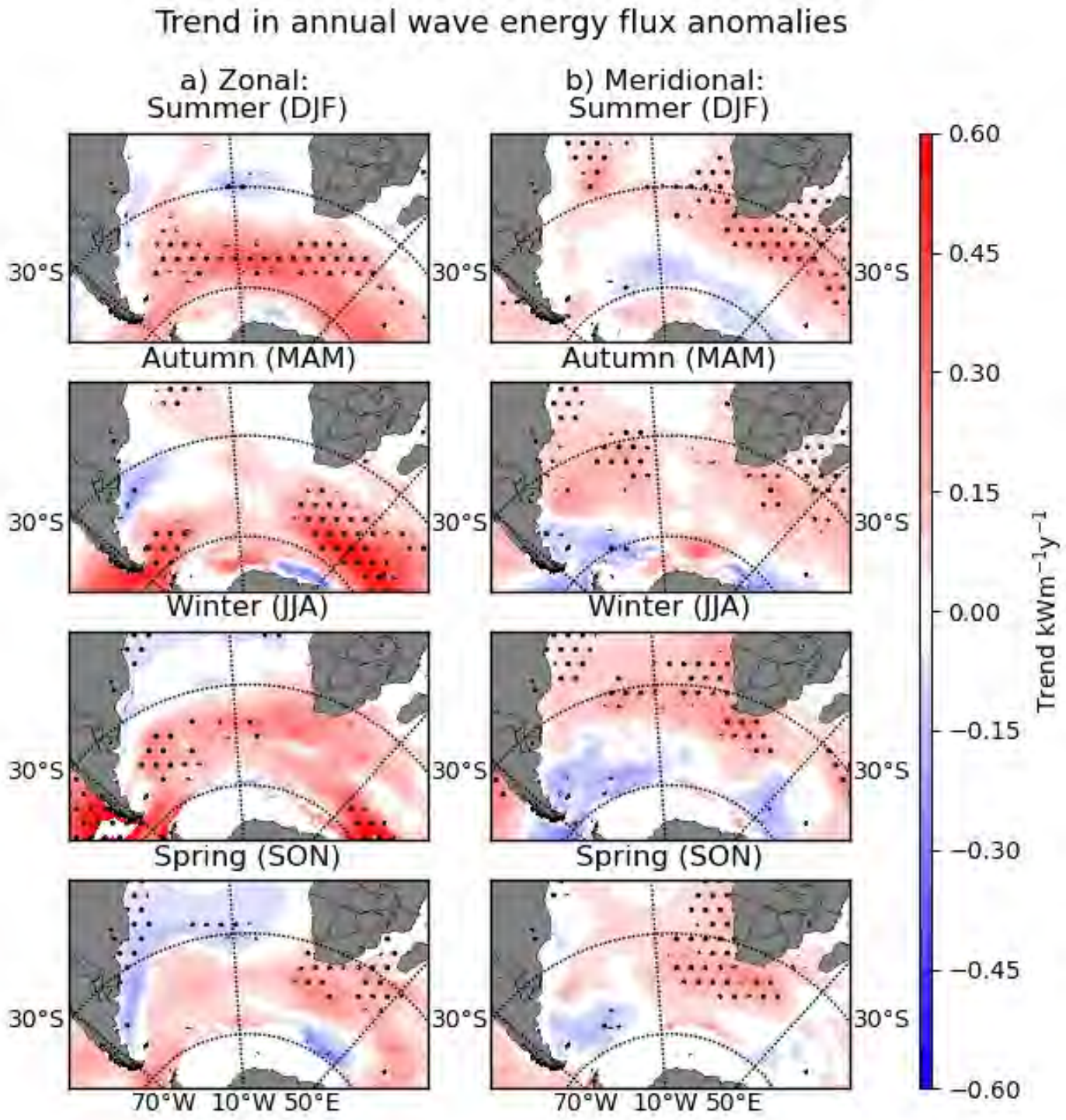

Figure A4: The annual trend in the mean seasonal zonal and meridional wave energy flux fields. The dots indicate 95% significance as determined through the pre-whitened Mann-Kendal test over the period 1980 – 2019

Season:	SAM		ENSO		SAO	
	Positive	**Negative**	**Positive (El Niño)**	**Negative (La Niña)**	**Positive**	**Negative**
Summer (DJF)	19	20	23	25	30	18
Autumn (MAM)	16	15	12	13	5	42
Winter (JJA)	25	24	13	10	40	0
Spring (SON)	24	21	24	23	18	14

Table A1: Sample sizes for the composite analysis for each phase of each mode investigated (SAM, the SAO, and ENSO)

References

Amrutha, M. M. and Sanil Kumar, V. (2019) 'Changes in wave energy in the shelf seas of India during the last 40 years based on ERA5 reanalysis data', *Energies*, 13(1), pp. 1–23. doi: 10.3390/en13010115.

Ashok, K., Nakamura, H. and Yamagata, T. (2007) 'Impacts of ENSO and Indian Ocean dipole events on the Southern Hemisphere storm-track activity during austral winter', in *Journal of Climate*, pp. 3147–3163. doi: 10.1175/JCLI4155.1.

Ashok, K. and Yamagata, T. (2009) 'Climate change: The El Nĩno with a difference', *Nature*, pp. 481–484. doi: 10.1038/461481a.

Barnes, M. A. and Rautenbach, C. (2020) 'Toward Operational Wave-Current Interactions Over the Agulhas Current System', *Journal of Geophysical Research: Oceans*, 125(7), pp. 1–21. doi: 10.1029/2020JC016321.

Barnett, T. P. and Sutherland, A. J. (1968) 'A note on an overshoot effect in wind-generated waves', *Journal of Geophysical Research*, 73(22), pp. 6879–6885. doi: 10.1029/jb073i022p06879.

Birkett, A. (2010) *Relationship Between Atmospheric Variability and Variability in the Wave Record at Cape Point*. University of Cape Town.

Blamey, R. C. *et al.* (2018) 'The role of regional circulation features in regulating El Niño climate impacts over southern Africa: A comparison of the 2015/2016 drought with previous events', *International Journal of Climatology*, 38(11), pp. 4276–4295. doi: 10.1002/joc.5668.

van der Borch van Verwolde, E. (2004) *Characteristics of extreme wave events and the correlation between atmospheric conditions along the South African coast*. University of Cape Town.

Bretherton, C. S. *et al.* (1999) 'The effective number of spatial degrees of freedom of a time-varying field', *Journal of Climate*, 12(7), pp. 1990–2009. doi: 10.1175/1520-0442(1999)012<1990:TENOSD>2.0.CO;2.

Burls, N. J., Blamey, R. C., Cash, B.A., *et al.* (2019) 'The Cape Town "Day Zero" drought and Hadley cell expansion', *Climate and Atmospheric Science*, pp. 285–287. doi: 10.1016/B978-0-323-60984-5.00062-7.

Burls, N. J., Blamey, R. C., Cash, Benjamin A., *et al.* (2019) 'The Cape Town "Day Zero" drought and Hadley cell expansion', *npj Climate and Atmospheric Science*. Nature Research, 2(1). doi: 10.1038/s41612-019-0084-6.

Burnett, A. W. and McNicoll, A. R. (2000) 'Intel-annual variations in the southern hemisphere winter circumpolar vortex: Relationships with the semiannual oscillation', *Journal of Climate*, 13(5), pp. 991–999. doi: 10.1175/1520-0442(2000)013<0991:IVITSH>2.0.CO;2.

Caires, S. and Sterl, A. (2005) '100-year return value estimates for ocean wind speed and significant wave height from the ERA-40 data', *Journal of Climate*, 18(7), pp. 1032–1048. doi: 10.1175/JCLI-3312.1.

Chawla, A. *et al.* (2009) *Validation of a multi-grid WAVEWATCH III TM modeling system*.

Colberg, F., Reason, C. J. C. and Rodgers, K. (2004) 'South Atlantic response to El Niño-Southern Oscillation induced climate variability in an ocean general circulation model', *Journal of Geophysical Research C: Oceans*, 109(12), pp. 1–14. doi: 10.1029/2004JC002301.

Corbella, S. and Strech, D. D. (2012) 'The wave climate on the KwaZulu-Natal coast of South Africa', *Journal of the South African Institution of Civil Engineering*, 54(2), pp. 45–54.

Corbella, S. and Stretch, D. D. (2012) 'Decadal trends in beach morphology on the east coast of South Africa and likely causative factors', *Natural Hazards and Earth System Science*, 12(8), pp. 2515–2527. doi: 10.5194/nhess-12-2515-2012.

Corson, W. D. and Resio, D. T. (1981) 'Comparisons of Hindcast and Measured Deepwater, Significant Wave Heights', *Wave Information Studies of U.S. Coastlines*.

Cox, A. T. and Swail, V. R. (2001) 'A global wave hindcast over the period 1958-1997: Validation

and climate assessment', *Journal of Geophysical Research: Oceans*, 106(C2), pp. 2313–2329. doi: 10.1029/2001jc000301.

Darbyshire, J. and Darbyshire, M. (1964) 'Wave observations in South African waters', *South African Journal of Science*, 60(6), pp. 183–189.

Darbyshire, M. and Pritchard, E. (1966) 'Sea waves near the coasts of South Africa', *Deutsche Hydrografische Zeitschrift*, 19(5), pp. 218–225.

Durrant, T. *et al.* (2014) *A Global Hindcast focussed on the Central and South Pacific, CAWCR Technical Report*. Available at: http://www.cawcr.gov.au/technical-reports/CTR_070.pdf.

Fahad, A. al, Burls, N. J. and Strasberg, Z. (2020) 'How will southern hemisphere subtropical anticyclones respond to global warming? Mechanisms and seasonality in CMIP5 and CMIP6 model projections', *Climate Dynamics*. Springer Berlin Heidelberg, 55(3), pp. 703–718. doi: 10.1007/s00382-020-05290-7.

Fitchett, J. (2018) 'Recent emergence of CAT5 tropical cyclones in the South Indian Ocean', *South African Journal of Science*, 114(11–12). doi: 10.17159/sajs.2018/4426.

Fitchett, J. M. and Grab, S. W. (2014) 'A 66-year tropical cyclone record for south-east Africa: Temporal trends in a global context', *International Journal of Climatology*, 34(13), pp. 3604–3615. doi: 10.1002/joc.3932.

Gelci, R. (1957) 'Prévision de la houle. La méthode des densités spectroangulaires', *Bull Inform Comite Central Oceanogr D'Etude*. Available at: https://ci.nii.ac.jp/naid/10007645104/ (Accessed: 12 August 2019).

Gillett, N. P., Kell, T. D. and Jones, P. D. (2006) 'Regional climate impacts of the Southern Annular Mode', *Geophysical Research Letters*, 33(23), pp. 1–4. doi: 10.1029/2006GL027721.

Godoi, V. A. *et al.* (2019) 'Regional-scale ocean wave variability associated with El Niño–Southern Oscillation-Madden-Julian Oscillation combined activity', *International Journal of Climatology*, 39(1), pp. 483–494. doi: 10.1002/joc.5823.

Godoi, V. A. *et al.* (2020) 'What happens to the ocean surface gravity waves when ENSO and MJO phases combine during the extended boreal winter?', *Climate Dynamics*. Springer Berlin Heidelberg, 54(3–4), pp. 1407–1424. doi: 10.1007/s00382-019-05065-9.

Godoi, V. A. and Torres Júnior, A. R. (2020) 'A global analysis of austral summer ocean wave variability during SAM–ENSO phase combinations', *Climate Dynamics*. Springer Berlin Heidelberg, 54(0123456789). doi: 10.1007/s00382-020-05217-2.

Gong, D. and Wang, S. (1999) 'Definition of Antarctic oscillation index', *Geophysical Research*

Letters, 26(4), pp. 459–462. doi: 10.1029/1999GL900003.

Gramcianinov, C. B. *et al.* (2020) 'Analysis of Atlantic extratropical storm tracks characteristics in 41 years of ERA5 and CFSR/CFSv2 databases', *Ocean Engineering*. Elsevier Ltd, 216(August), p. 108111. doi: 10.1016/j.oceaneng.2020.108111.

Grundlingh, M. and Rossouw, M. (1995) 'Wave attenuation in the Agulhas Current', *South African Journal of Science*, 91(7), pp. 357–359.

Günther, H. *et al.* (1998) 'The wave climate of the Northeast Atlantic over the period 1955-1994: The WASA wave hindcast', *Global Atmosphere and Ocean System*, 6(2), pp. 121–163.

Gweba, B. and Krug, M. (2019) *Evaluation of global wave forecast models against the buoy data along the South African coast*.

Hanson, J., Tracy, B. and Tolman, H. (2006) 'Pacific hindcast performance evaluation of three numerical wave models', *In 9th International Workshop on Wave Hindcasting and Forecasting*, pp. 1–29. Available at: http://www.gebco.net.

Hasselmann, K. (1963) 'On the non-linear energy transfer in a gravity-wave spectrum: Part 3. Evaluation of the energy flux and swell-sea interaction for a Neumann spectrum', *Journal of Fluid Mechanics*, 15(3), pp. 385–398. doi: 10.1017/S002211206300032X.

Hasselmann, K. *et al.* (1973) 'Measurements of Wind-Wave Growth and Swell Decay during the Joint North Sea Wave Project (JONSWAP)', *Ergnzungsheft zur Deutschen Hydrographischen Zeitschrift Reihe*, A(8), pp. 8–12. doi: citeulike-article-id:2710264.

Hasselmann, K. *et al.* (1988) 'The WAM model - a third generation ocean wave prediction model.', *J. PHYS. OCEANOGR.*, 18(12, Dec. 1988), pp. 1775–1810. doi: 10.1175/1520-0485(1988)018<1775:twmtgo>2.0.co;2.

Hemer, M. A., Church, J. A. and Hunter, J. R. (2010) 'Variability and trends in the directional wave climate of the Southern Hemisphere', *International Journal of Climatology*, 30(4), pp. 475–491. doi: 10.1002/joc.1900.

Hersbach, H. *et al.* (2020) 'The ERA5 global reanalysis', *Quarterly Journal of the Royal Meteorological Society*, 146(730), pp. 1999–2049. doi: 10.1002/qj.3803.

Holthuijsen, L. H. (2010) *Waves in Oceanic and Coastal Waters*. New York: Cambridge University Press.

Hurrell, J. W. and van Loon, H. (1994) 'A modulation of the atmospheric annual cycle in the Southern Hemisphere', *Tellus A*, 46(3), pp. 325–338. doi: 10.1034/j.1600-0870.1994.t01-1-00007.x.

Janssen, P. A. E. M., Hansen, B. and Bidlot, J. R. (1997) 'Verification of the ECMWF wave forecasting system against buoy and altimeter data', *Weather and Forecasting*, 12(4), pp. 763–784. doi: 10.1175/1520-0434(1997)012<0763:VOTEWF>2.0.CO;2.

Joubert, J. R. (2008) 'An investigation of the wave energy resource on the south african coast, focusing on the spatıal distribution of the south west coast', (March), p. 183.

Joubert, J. R. and van Niekerk, J. L. (2013) 'South African wave energy resource data: A case study', *Centre for Renewable and Sustainable Energy Studies*, 27(May), pp. 1–36.

Jury, M. R. (2019) 'Meteorological controls on big waves south of Africa', *Regional Studies in Marine Science*. Elsevier B.V., 27, p. 100538. doi: 10.1016/j.rsma.2019.100538.

Kendall, M. G. (1948) 'Rank correlation methods.'

Komen, G. J. *et al.* (1996) 'Dynamics and Modelling of Ocean Waves', in *Dynamics and Modelling of Ocean Waves*. New York: Cambridge University Press, pp. 1–69. doi: 10.1017/CBO9780511628955.

Kumar, P. *et al.* (2019) 'Influence of Natural Climate Variability on the Extreme Ocean Surface Wave Heights Over the Indian Ocean', *Journal of Geophysical Research: Oceans*, 124(8), pp. 6176–6199. doi: 10.1029/2019JC015391.

Kushnir, Y. *et al.* (1997) 'The recent increase in North Atlantic wave heights', *Journal of Climate*, 10(8), pp. 2107–2113. doi: 10.1175/1520-0442(1997)010<2107:TRIINA>2.0.CO;2.

Laing, A. *et al.* (1998) *Guide to wave analysis. Second Ed., World Meterological Organization (WMO-No. 702)*.

Lavidas, G. and Venugopal, V. (2018) 'Prospects and applicability of wave energy for South Africa', *International Journal of Sustainable Energy*. Taylor & Francis, 37(3), pp. 230–248. doi: 10.1080/14786451.2016.1254216.

Lavrenov, I. V. (1998) 'The wave energy concentration at the Agulhas Current off South Africa', *Natural Hazards*, 17(2), pp. 117–127. doi: 10.1023/A:1007978326982.

Lim, E. P., Hendon, H. H. and Rashid, H. (2013) 'Seasonal predictability of the southern annular mode due to its association with ENSO', *Journal of Climate*, 26(20), pp. 8037–8054. doi: 10.1175/JCLI-D-13-00006.1.

van Loon, H. (1967) 'The Half-Yearly Oscillations in Middle and High Southern Latitudes and the Coreless Winter', *Journal of The Atmospheric Sciences*, 24, pp. 472–487.

Lorenz, D. J. and Hartmann, D. L. (2001) 'Eddy-zonal flow feedback in the Southern Hemisphere',

Journal of the Atmospheric Sciences, 58(21), pp. 3312–3327. doi: 10.1175/1520-0469(2001)058<3312:EZFFIT>2.0.CO;2.

Lyttle, C. T. *et al.* (2018) *Analysing Modelled Nearshore Wave Climate Variability and Change as Relevant to the Traditional Handline Fishery of the South African Coast*. University of Cape Town.

Lyu, K. *et al.* (2020) 'Processes responsible for the southern hemisphere ocean heat uptake and redistribution under anthropogenic warming', *Journal of Climate*, 33(9), pp. 3787–3807. doi: 10.1175/JCLI-D-19-0478.1.

Mandal, S. and Prabaharan, N. (2010) 'Ocean Wave Prediction Using Numerical and Neural Network Models', *The Open Ocean Engineering Journal*, 3(1), pp. 12–17. doi: 10.2174/1874835x01003010012.

Mann, H. B. (1945) 'Nonparametric Tests Against Trend', *Econometrica*, 13(3), pp. 245–259. Available at: http://www.jstor.com/stable/1907187.

Marshall, A. G. *et al.* (2018) 'Southern annular mode impacts on global ocean surface waves', *Ocean Modelling*. Elsevier, 129(February), pp. 58–74. doi: 10.1016/j.ocemod.2018.07.007.

Marshall, G. J. (2003) 'Trends in the Southern Annular Mode from observations and reanalyses', *Journal of Climate*, 16(24), pp. 4134–4143. doi: 10.1175/1520-0442(2003)016<4134:TITSAM>2.0.CO;2.

Mawren, D. and Reason, C. (2017) 'Variability of upper-ocean characteristics and tropical cyclones in the South West Indian Ocean', *Journal of Geophysical Research : Oceans*, 122, pp. 2012–2028. doi: 10.1002/2016JC012028.Received.

Meehl, G. A., Hurrell, J. W. and Loon, H. Van (1998) 'A modulation of the mechanism of the semiannual oscillation in the Southern Hemisphere', *Tellus A: Dynamic Meteorology and Oceanography*, 50(4), pp. 442–450. doi: 10.3402/tellusa.v50i4.14537.

Meucci, A. *et al.* (2020) 'Projected 21st century changes in extreme wind-wave events', *Science Advances*, 6(24), pp. 1–10. doi: 10.1126/sciadv.aaz7295.

Miles, J. W. (1957) 'On the generation of surface waves by shear flows', *Journal of Fluid Mechanics*, 3(2), pp. 185–204. doi: 10.1017/s0022112059000842.

Mitsuyasu, H. (1971) 'On the Form of Fetch-Limited Wave Spectrum', *Coastal Engineering in Japan*, 14(1), pp. 7–14. doi: 10.1080/05785634.1971.11924122.

Morim, J. *et al.* (2019) 'Robustness and uncertainties in global multivariate wind-wave climate projections', *Nature Climate Change*. Springer US, 9(9), pp. 711–718. doi: 10.1038/s41558-019-0542-5.

Morris, T., Rautenbach, C. and Stander, J. (2019) ‘A new era for marine forecasting in South Africa’, *South African Journal of Science*, 115(5–6), pp. 5–6. doi: 10.17159/sajs.2019/6170.

Ndarana, T. and Waugh, D. W. (2010) ‘The link between cut-off lows and Rossby wave breaking in the Southern Hemisphere’, *Quarterly Journal of the Royal Meteorological Society*, 136(649), pp. 869–885. doi: 10.1002/qj.627.

Nguyen, H. *et al.* (2018) ‘Variability of the extent of the Hadley circulation in the southern hemisphere: a regional perspective’, *Climate Dynamics*, 50(1–2), pp. 129–142. doi: 10.1007/s00382-017-3592-2.

NOAA (2009) *National Weather Service : Environmental Modelling Center - NOAA WaveWatch III*. Available at: https://polar.ncep.noaa.gov/waves/wavewatch/.

Pal, M. *et al.* (2020) ‘Long-lead Prediction of ENSO Modoki Index using Machine Learning algorithms’, *Scientific Reports*, 10(1), pp. 1–13. doi: 10.1038/s41598-019-57183-3.

Pezza, A. B. *et al.* (2008) ‘Southern hemisphere synoptic behavior in extreme phases of SAM, ENSO, sea ice extent, and Southern Australia rainfall’, *Journal of Climate*, 21(21), pp. 5566–5584. doi: 10.1175/2008JCLI2128.1.

Phillips, O. (1957) ‘On the generation of waves by turbulent wind’, *Journal of Fluid Mechanics*, 2(5), pp. 417–445. doi: 10.1017/S0022112057000233.

Phillips, O. (1958) ‘The equilibrium range in the spectrum of wind-generated waves’, *Journal of Fluid Mechanics*, 4(4), pp. 426–434. doi: 10.1017/S0022112058000550.

Phinn, S. R. and Hastings, P. A. (1992) ‘Southern Oscillation Influences on the Wave Climate of South-Eastern Australia’, *Journal of Coastal Research*, 8(3), pp. 579–592.

Pierson, W. J. (1955) *Wind generated gravity waves*, *Advances in Geophysics*. doi: 10.1016/S0065-2687(08)60312-X.

Previdi, M. and Liepert, B. G. (2007) ‘Annular modes and Hadley cell expansion under global warming’, *Geophysical Research Letters*, 34(22), pp. 5–9. doi: 10.1029/2007GL031243.

Quilfen, Y. and Chapron, B. (2019) ‘Ocean Surface Wave-Current Signatures From Satellite Altimeter Measurements’, *Geophysical Research Letters*. Blackwell Publishing Ltd, 46(1), pp. 253–261. doi: 10.1029/2018GL081029.

Ramon, J. *et al.* (2019) ‘What global reanalysis best represents near-surface winds?’, *Quarterly Journal of the Royal Meteorological Society*, 145(724), pp. 3236–3251. doi: 10.1002/qj.3616.

Rapizo, H., Durrant, T. H. and Babanin, A. V. (2018) ‘An assessment of the impact of surface

currents on wave modeling in the Southern Ocean', *Ocean Dynamics*. Springer Verlag, 68(8), pp. 939–955. doi: 10.1007/s10236-018-1171-7.

Reason, C. J. C. *et al.* (2000) 'Enso and climatic signals across the Indian Ocean basin in the global context: Part I, Interannual composite patterns', *International Journal of Climatology*, 20(11), pp. 1285–1327. doi: 10.1002/1097-0088(200009)20:11<1285::AID-JOC536>3.0.CO;2-R.

Reason, C. J. C. (2017) 'Climate of Southern Africa', *Oxford Research Encyclopedia of Climate Science*, pp. 1–39. doi: 10.1093/acrefore/9780190228620.013.513.

Reason, C. J. C. and Jagadheesha, D. (2005) 'A model investigation of recent ENSO impacts over southern Africa', *Meteorology and Atmospheric Physics*, 89(1–4), pp. 181–205. doi: 10.1007/s00703-005-0128-9.

Reason, C. J. C. and Keibel, A. (2004) 'Tropical Cyclone Eline and its unusual penetration and impacts over the Southern Africa mainland', *Weather and Forecasting*, 19(5), pp. 789–805. doi: 10.1175/1520-0434(2004)019<0789:TCEAIU>2.0.CO;2.

Reason, C. J. C. and Rouault, M. (2005) 'Links between the Antarctic Oscillation and winter rainfall over western South Africa', *Geophysical Research Letters*, 32(7), pp. 1–4. doi: 10.1029/2005GL022419.

Reguero, B. G., Losada, I. J. and Méndez, F. J. (2019) 'A recent increase in global wave power as a consequence of oceanic warming', *Nature Communications*. Springer US, 10(1), pp. 1–14. doi: 10.1038/s41467-018-08066-0.

Rind, D. *et al.* (2001) 'Climate response to basin-specific changes in latitudinal temperature gradients and implications for sea ice variability', *Journal of Geophysical Research Atmospheres*, 106(D17), pp. 20161–20173. doi: 10.1029/2000JD900643.

Rossouw, C. (1999) *The Probability of Occurrence and the Intensity of Tropical Cyclones Along the Southern African East Coast*. University of Stellenbosch.

Rossouw, J., Coetzee, L. W. and Visser, C. J. (1982) 'A South African Wave Climate Study', *Coastal Engineering*, pp. 1405–1418.

Rossouw, M. and Phelp, D. (1996) 'An Evaluation of Two Wave Forecast Models for the South African Region', in *Coastal Engineering*, pp. 340–353. doi: 10.1061/9780784402429.027.

Rouault, M., Pohl, B. and Penven, P. (2010) 'Coastal oceanic climate change and variability from 1982 to 2009 around South Africa', *African Journal of Marine Science*, 32(2), pp. 237–246. doi: 10.2989/1814232x.2010.501563.

Schoeberl, M. R. and Newman, P. A. (2015) 'Middle Atmosphere: Polar Vortex', *Encyclopedia of*

Atmospheric Sciences: Second Edition. Elsevier Inc., pp. 12–17. doi: 10.1016/B978-0-12-382225-3.00228-0.

Seymour, R. (1996) 'Wave Climate Variability in Southern California', *Journal of Waterway, Port, Coastal, and Ocean Engineering*, 122(4), pp. 182–186. doi: 10.1061/(asce)0733-950x(1996)122:4(182).

Seymour, R. J. *et al.* (1985) 'Influence of El Ninos on California's wave climate.', *IN: PROC. NINETEENTH INT. CONF. ON COASTAL ENGINEERING (HOUSTON, U.S.A.: SEP. 3-7, 1984), B.L. EDGE (ED.)*, 1, New Yo, pp. 577–592.

Shillington, F. A. (1974) *Characteristics of Ocean Gravity Waves off the Cape South West Coast*.

Shillington, F. A. and Britten-Jones, A. (1979) 'Features of Surface Waves off the Southern Cape Coast and Their Associated Meteorological Conditions during a Severe Storm between 30 August and 3 September 1978', *South African Journal of Science*, 75(November).

Silvestri, G. E. and Vera, C. S. (2003) 'Antarctic Oscillation signal on precipitation anomalies over southeastern South America', 30(21), p. 2115. doi: 10.1029/2003GL018277.

Singleton, A. T. and Reason, C. (2007) 'Variability in the characteristics of cut-off low pressure systems over subtropical souther Africa', *International Journal of Climatology*, 27, pp. 295–310. doi: 10.1002/joc.

Smith, G. A. *et al.* (2021) 'Global wave hindcast with Australian and Pacific Island Focus: From past to present', *Geoscience Data Journal*, 8(1), pp. 24–33. doi: 10.1002/gdj3.104.

Sreelakshmi, S. and Bhaskaran, P. K. (2020) 'Wind-generated wave climate variability in the Indian Ocean using ERA-5 dataset', *Ocean Engineering*. Elsevier Ltd, 209(January), p. 107486. doi: 10.1016/j.oceaneng.2020.107486.

Sterl, A, Komen, G. J. and Cotton, P. D. (1998) 'Fifteen years of global wave hindcasts using winds from the European Centre for Medium-Range Weather Forecasts reanalysis: Validating the reanalyzed winds and assessing the wave climate', *Journal of Ge*, 100, pp. 5477–5492.

Sterl, A., Komen, G. J. and Cotton, P. D. (1998) 'Fifteen years of global wave hindcasts using winds from the European Centre for Medium-Range Weather Forecasts reanalysis: Validating the reanalyzed winds and assessing the wave climate', *Journal of Geophysical Research: Oceans*. American Geophysical Union (AGU), 103(C3), pp. 5477–5492. doi: 10.1029/97jc03431.

Stopa, J. E. *et al.* (2013) 'Patterns and cycles in the Climate Forecast System Reanalysis wind and wave data', *Ocean Modelling*. Elsevier Ltd, 70, pp. 207–220. doi: 10.1016/j.ocemod.2012.10.005.

Sverdrup, H. and Munk, W. H. (1947) 'Wind, Sea, and Swell. Theory of Relations For Forecasting',

Hydrology Office Washington, (601), p. 44.

SWAMP Group (1985) 'Ocean Wave Modeling', in *Ocean Wave Modeling*. New York: Plenum Press, pp. 1–19.

Takbash, A. and Young, I. R. (2020) 'Long-term and seasonal trends in global wave height extremes derived from era-5 reanalysis data', *Journal of Marine Science and Engineering*, 8(12), pp. 1–16. doi: 10.3390/jmse8121015.

Taylor, K. E. (2001) 'Summarizing multiple aspects of model performance in a Single Diagram', *Journal of Geophysical Research*, 106(D7), pp. 7183–7192. doi: 10.1029/2000JD900719.

Theron, A. *et al.* (2014) 'MetOcean conditions & vulnerability - Medium resolution wave climate & run-up', *South African coastal vulnerability assessment DEA - CSIR : Phase 2*.

Theron, A. K. (2016) *Methods for Determination of Coastal Development Setback Lines in South Africa*.

Thompson, D. W. J. and Solomon, S. (2002) 'Interpretation of recent Southern Hemisphere climate change', *Science*, 296(5569), pp. 895–899. doi: 10.1126/science.1069270.

Thompson, D. W. J. and Wallace, J. M. (2000) 'Annular modes in the extratropical circulation. Part I: Month-to-month variability', *Journal of Climate*, 13(5), pp. 1000–1016.

Timmermans, B. W. *et al.* (2020) 'Global Wave Height Trends and Variability from New Multimission Satellite Altimeter Products, Reanalyses, and Wave Buoys', *Geophysical Research Letters*, 47(9). doi: 10.1029/2019GL086880.

Toffoli, A. *et al.* (2010) 'Maximum steepness of oceanic waves: Field and laboratory', *Geophysical Research Letters*, 37(5), pp. 1–4. doi: 10.1029/2009GL041771.

Tolman, H. L. (1989) 'The numerical model WAVEWATCH: a third generation model for hindcasting of wind waves on tides in shelf seas', *Communications on Hydraulic and Geotechnical Engineering*, 89–02(2, Apr., 1989), pp. 1–72.

Tolman, H. L. (1991) 'A third-generation model for wind waves on slowly varying, unsteady, and inhomogeneous depths and currents', *Journal of Physical Oceanography*, 21(6), pp. 782–797.

Tolman, H. L. (1992) 'Effects of numerics on the physics in a third-generation wind-wave model', *Journal of Physical Oceanography*, 22(10), pp. 1095–1111.

Torrence, C. and Compo, G. P. (1998) 'A Practical Guide to Wavelet Analysis', *Bulletin of the American Meteorological Society*, 79(1), pp. 61–78. doi: 10.1175/1520-0477(1998)079<0061:APGTWA>2.0.CO;2.

Trenberth, K. E. and Stepaniak, D. P. (2001) ‘Indices of El Niño evolution’, *Journal of Climate*. American Meteorological Society, 14(8), pp. 1697–1701. doi: 10.1175/1520-0442(2001)014<1697:LIOENO>2.0.CO;2.

Veitch, J. *et al.* (2019) ‘The Cape Point wave record, extreme events and the role of large-scale modes of climate variability’, *Journal of Marine Systems*, 198. doi: 10.1016/j.jmarsys.2019.103185.

Wang, X. L. and Swail, V. R. (2002) ‘Trends of Atlantic wave extremes as simulated in a 40-yr wave hindcast using kinematically reanalyzed wind fields’, *Journal of Climate*, 15(9), pp. 1020–1035. doi: 10.1175/1520-0442(2002)015<1020:TOAWEA>2.0.CO;2.

Wingeart, K. M. (2001) *Validation of Operational Global Wave Prediction Models with Spectral Buoy Data, Ocean Wave Measurement and Analysis*. Naval Postgraduate School.

Young, I. R. (1999a) ‘Seasonal variability of the global ocean wind and wave climate’, *International Journal of Climatology*, 19(9), pp. 931–950. doi: 10.1002/(SICI)1097-0088(199907)19:9<931::AID-JOC412>3.0.CO;2-O.

Young, I. R. (1999b) ‘Seasonal variability of the global ocean wind and wave climate’, *International Journal of Climatology*. John Wiley & Sons, Ltd, 19(9), pp. 931–950. doi: 10.1002/(SICI)1097-0088(199907)19:9<931::AID-JOC412>3.0.CO;2-O.

Young, I. R. *et al.* (2020) ‘The wave climate of the southern ocean’, *Journal of Physical Oceanography*, 50(5), pp. 1417–1433. doi: 10.1175/JPO-D-20-0031.1.

Young, I. R. and Ribal, A. (2019) ‘Multiplatform evaluation of global trends in wind speed and wave height’, *Science*, 364(6440), pp. 548–552. doi: 10.1126/science.aav9527.

Young, I. R., Sanina, E. and Babanin, A. V. (2017) ‘Calibration and cross validation of a global wind and wave database of altimeter, radiometer, and scatterometer measurements’, *Journal of Atmospheric and Oceanic Technology*, 34(6), pp. 1285–1306. doi: 10.1175/JTECH-D-16-0145.1.

Young, I. R., Zieger, S. and Babanin, A. V. (2011) ‘Global Trends in Wind Speed’, *Science*, 159(April), pp. 451–455.

Yu, J. Y. *et al.* (2015) ‘The early 1990s change in ENSO-PSA-SAM relationships and its impact on Southern Hemisphere climate’, *Journal of Climate*, 28(23), pp. 9393–9408. doi: 10.1175/JCLI-D-15-0335.1.